

Dissertation

**Unfolding the Spectrum of the
Blazar Markarian 421 using Data from
the First Large-Sized Telescope of the
Cherenkov Telescope Array**

Noah Biederbeck

2023

A document submitted in partial fulfillment of the requirements for the degree of
Doctor rerum naturalium at Fakultät Physik, Technische Universität Dortmund

Supervised by
Prof. Dr. Dr. Wolfgang Rhode and Prof. Dr. Johannes Albrecht

Der Inhalt der Physik geht die
Physiker an, die Auswirkung alle
Menschen.

Friedrich Dürrenmatt
Die Physiker

Abstract

The nature of acceleration processes of very-high-energy radiation in the universe is largely unsolved. To study these, Imaging Atmospheric Cherenkov Telescopes measure Cherenkov radiation produced by secondary particles in Extensive Air Showers. The **Cherenkov Telescope Array (CTA)** is the next generation of ground-based Cherenkov astronomy to be built in the coming years parts on La Palma, Spain and parts at Paranal Observatory, Chile. The first prototype telescope of **CTA**, the **LST-1**, was inaugurated in 2018 on La Palma, and has been in the commissioning phase since. In this thesis, I develop a new automated analysis pipeline for analyses of point-like gamma-ray sources for **LST-1** observations, using the workflow manager **snakemake**. I implement regularized unfolding in the open-source high-level gamma-ray analysis software **Gammapy**. I use the analysis pipeline and the unfolding implementation to analyze data of the blazar Markarian 421, creating an unfolded energy spectrum. The unfolded energy spectrum calculated in this thesis is compared to earlier analyses. It extends the measured range of the multi-wavelength energy spectrum of Markarian 421 to the highest energies.

Zusammenfassung

Die Natur der Beschleunigungsmechanismen für sehr hochenergetische Strahlung im Universum ist weitestgehend ungeklärt. Um diese zu untersuchen, werden bildgebende, atmosphärische Tscherenkow Teleskope eingesetzt, die Tscherenkowstrahlung messen, die von Sekundärteilchen in ausgedehnten Luftschauern erzeugt wird. Das **Cherenkov Telescope Array (CTA)** ist die nächste Generation der bodengebundenen Tscherenkow-Astronomie und wird in den kommenden Jahren teils auf La Palma, Spanien, teils im Paranal Observatory, Chile, gebaut. Das erste Prototyp-Teleskop des **CTA**, das **LST-1**, wurde 2018 auf La Palma eingeweiht und befindet sich seitdem in der Phase der Inbetriebnahme. In dieser Arbeit entwickle ich eine neue automatisierte Analysepipeline für Analysen von punktförmigen kosmischen Gammastrahlungsquellen für **LST-1**-Beobachtungen unter Verwendung des Workflow-Managers **snakemake**. Ich implementiere regularisiertes Entfalten in der quelloffenen Gammastrahlenanalysesoftware **Gammapy**. Ich verwende die Analysepipeline und die Entfaltungsimplementierung, um Daten des Blazars Markarian 421 zu analysieren und ein entfaltetes Energiespektrum zu erstellen. Das in dieser Arbeit entfaltetes Energiespektrum wird mit früheren Analysen verglichen und erweitert den gemessenen Bereich des multiwellenlängen Energiespektrums von Markarian 421 bis zu den höchsten Energien.

Contents

1	Introduction	1
2	Active Galactic Nuclei	5
2.1	Sources of Very-High-Energy Radiation	5
2.2	Interstellar Medium and Messenger Particles	11
2.3	Extensive Air Showers	12
2.4	Cherenkov Radiation	14
3	Detection	17
3.1	Imaging Atmospheric Cherenkov Telescopes	17
3.2	The Cherenkov Telescope Array	19
3.3	The Large-Sized Telescope	20
3.4	Data Analysis	22
4	Simulation and Analysis	25
4.1	Simulation	25
4.2	Low-Level Analysis	29
4.3	Machine Learning	34
4.4	Instrument Response Functions	43
4.5	Background Estimation	46
4.6	High-Level Analysis	47
5	LST Analysis	51
5.1	Data Selection	51
5.2	All-Sky Monte Carlo Simulation	55
5.3	Calculating Instrument Response Functions	58
5.4	Application of Models	63
5.5	List of Gamma-like Events	65
5.6	High-Level Analysis	68
6	Unfolding	71
6.1	Likelihood Unfolding	74
6.2	Unfolding of LST-1 Data	80
7	Conclusions and Outlook	85

Bibliography	89
Appendix	99
Glossary	109
Acknowledgements	113

1 Introduction

We have powerful tools: Openness,
optimism and the spirit of curiosity.

Jean-Luc Picard
Star Trek

In astronomy and astrophysics, we look at our galaxy and beyond. Humans have been observing the night sky since the dawn of time, and people are naturally fascinated by the vastness of the universe. Celestial observations with the naked eye allow us to recognize constellations and have helped us navigate at sea for centuries. We can see even further into space with optical telescopes, discover new planets, and describe new laws of physics. All this is possible because the Earth's atmosphere is transparent in the electromagnetic range of 400 nm to 800 nm, called the optical window. The atmosphere is also transparent in the radio regime, which enables radio astronomy observations. In all other regions of the electromagnetic spectrum, it is predominantly opaque.

More than one hundred years ago, researchers measured radiation with Geiger counters that they could not explain. In 1912, during hot air balloon flights, Victor Hess was able to explain for the first time that this radiation increases with altitude [59]. He called it *Höhenstrahlung*. Today we know that this radiation is made up of cosmic rays, to which the atmosphere is opaque. The cosmic rays interact with the upper layers of the atmosphere, creating secondary particles and forming **Extensive Air Showers (EASs)** by scattering processes. Gamma rays, extremely high energetic photons, induce **EASs** when entering the atmosphere, as charged cosmic rays do. This thesis is about gamma rays from extragalactic sources. The observation of **very-high-energy (VHE)** gamma rays led to increased interest in the scientific community in the 1960s. With the construction of the Whipple Observatory, astroparticle gamma-ray physics was born. Astroparticle physics combines particle physics and astrophysics to gain new insights into the physical mechanisms in the universe. It describes the processes in the galaxy and beyond, the propagation through the interstellar medium, and the interactions in the Earth's atmosphere. Astronomers have been observing, analyzing, and categorizing galactic and extragalactic sources for several years. The best-known galactic source among astroparticle physicists is the Crab Nebula. This supernova

remnant, a star that exploded in 1054 [83], was first detected in the VHE range by the Whipple Observatory in 1989 [101] and has since been used as a *standard candle* for experiments because of its strong and almost constant flux of VHE gamma rays. The Crab Nebula is used to study the performance of new generations of experiments and is often used as the first published detection.

In Cherenkov astronomy, the radiation emitted by secondary particles created in EASs by VHE particles is used to study galactic and extragalactic sources. Many Cherenkov telescopes have been built since the first detection of the Crab Nebula. Each has surpassed its predecessors by orders of magnitude in sensitivity by using more and larger telescopes with more sensitive cameras. The Cherenkov Telescope Array (CTA) will be the next ground-based gamma-ray observatory, consisting of tens of telescopes at two sites: The Observatorio del Roque de los Muchachos (ORM) on La Palma, Spain, in the northern hemisphere and the Paranal Observatory in Chile in the southern hemisphere. Both sites will contain multiple telescope types, each specializing in specific energy ranges. The configuration of CTA will allow observations of the entire night sky at higher sensitivities over more extensive energy ranges.

In this thesis, I describe in chapter 2 the essential physics of Active Galactic Nuclei (AGN), their acceleration of particles, including gamma rays, the interaction of VHE particles with the Earth's atmosphere, and the primary mechanism that can be used for detection with ground-based detectors: the emittance of Cherenkov radiation.

In chapter 3, I explain a class of ground-based detectors: Imaging Atmospheric Cherenkov Telescopes (IACTs). I describe the general structure and electronics, review different generations of experiments, describe the plan for the next-generation ground-based gamma-ray observatory CTA, and in particular the LST-1, the first Large-Sized Telescope (LST) for CTA.

In this thesis, I analyze data from the LST-1. I explain the general procedure for analyzing Cherenkov telescope data in chapter 4, where I also discuss Monte Carlo (MC) simulations needed to describe and evaluate the telescope performance. Furthermore, this chapter goes into detail on machine learning analysis methods and Instrument Response Functions (IRFs), the description of detector responses. The methods in this chapter serve for the general analysis of data from a mono-operating Cherenkov telescope.

In chapter 5, I describe the LST-1 specific data analysis for observations of the blazar Mrk 421. Here I discuss how to select data for analyses, the selection, training, and application of Machine Learning (ML) models, quality criteria for IRFs, and

show high-level results of Mrk 421, such as a Spectral Energy Distribution (SED) and Light Curve (LC).

Chapter 6 introduces unfolding, a way to solve inverse problems. I develop a prototype for unfolding in the open-source analysis software `Gammapy`. I use this prototype software to unfold LST-1 data.

Finally, I conclude this thesis with chapter 7, summarizing and discussing the work and giving an outlook on the future.

2 Active Galactic Nuclei

I don't believe in astrology; I'm a Sagittarian and we're skeptical.

Sir Arthur C. Clarke

When Victor Hess did his famous balloon flight in 1912 [59] he found curious radiation, increasing in intensity the higher he got. He called this radiation *Höhenstrahlung*, and the discovery was awarded a Nobel Prize in 1936¹. The fact that the radiation increases with altitude indicates the existence of extraterrestrial radiation: radiation of cosmic origin. The following sections describe the sources of this radiation, its production mechanisms, and the principles that lead to their detection on Earth.

2.1 Sources of Very-High-Energy Radiation

In the last decades, different experiments have investigated this radiation, called *charged cosmic rays*, and its spectrum almost perfectly follows a power law with index $\gamma = -2.7$, as shown in figure 2.1. Charged cosmic rays consist mainly of protons but also of heavier nuclei, such as helium or even iron. Galactic and intergalactic magnetic fields deflect these particles. Their arrival directions on Earth are isotropically distributed over the observable sky at all but the highest energies [1]. They do not allow conclusions about a point of origin, or *source*. To identify sources of high-energy radiation, *gamma rays* are helpful messengers. Gamma rays are photons accelerated to the highest energies. Because photons are not charged, magnetic fields do not deflect them, allowing conclusions about a source location. Cosmic rays are postulated to be accelerated in the most extreme environments, and gamma rays are byproducts in the processes occurring there. These environments include supernova remnants like the Crab Nebula shown in figure 2.2, collapsing binary systems, or *Supermassive Black Holes (SMBHs)* accreting matter. In extreme environments, gravitational energy is converted into kinetic energy of matter. In further processes, particles are accelerated to even higher energies. One process is

¹<https://www.nobelprize.org/prizes/physics/1936/hess/facts>

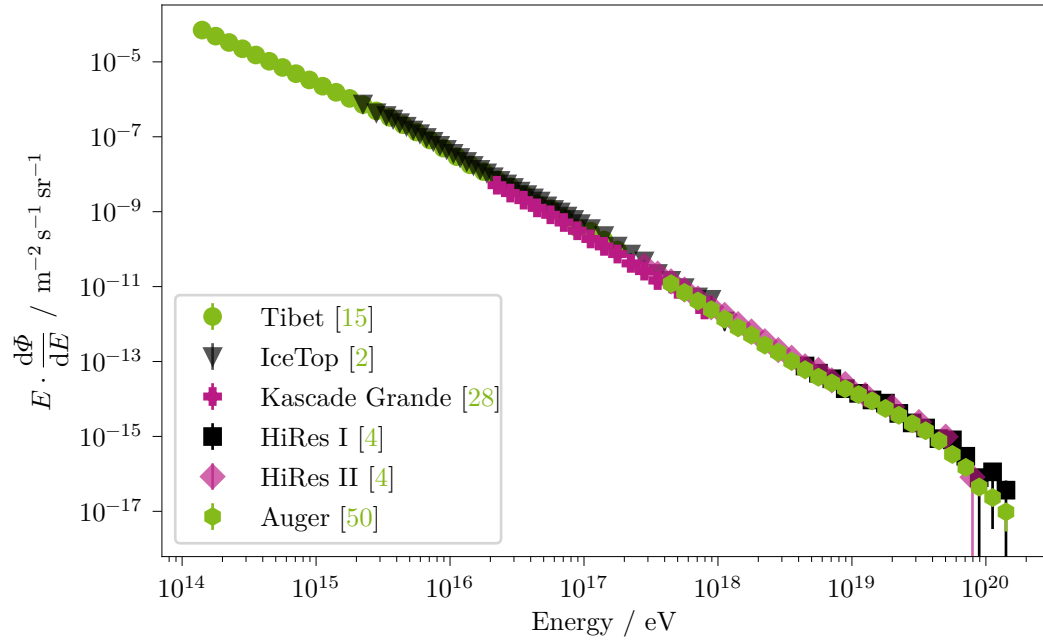


Figure 2.1: All-particle spectrum over many orders of magnitude of energy. Data provided by Kai Brügge [32].

described in the Fermi principle [24]: matter is accelerated in shock fronts in the vicinity of supernovae. Other acceleration principles, for example in **Active Galactic Nuclei (AGN)**, are not yet fully understood.

The scenarios which drive the production of **VHE** gamma rays in **AGN** are the leptonic and the lepto-hadronic scenario. In the leptonic scenario, electrons produce synchrotron radiation as high-energy gamma rays when they are deflected in the magnetic fields in the vicinity of the source

$$e^{-'} \rightarrow e^{-} + \gamma. \quad (2.1)$$

The inverse Compton effect, where a high-energy electron transfers its energy during scattering accelerates the gamma rays to even higher energies. When the synchrotron electrons feed the inverse Compton process, it is called **Synchrotron Self-Compton (SSC)**. In the hadronic scenario, high-energy hadrons collide with other particles and produce pions

$$p + N \rightarrow \pi^{+} + \pi^{-} + K + \mu + \pi^{0} + \dots \quad (2.2)$$



Figure 2.2: Composite image of the Crab Nebula [78]. Data used from the Very Large Array, the Spitzer Space Telescope, the Hubble Space Telescope, the XMM-Newton Observatory, and the Chandra X-ray Observatory. The outer expanding shell of the supernova and the rotating neutron star at the center are clearly visible. The Crab Nebula emits **VHE** gamma rays, and is used as *standard candle* for Cherenkov observatories due to its stability in the **VHE** regime.

Via the decay of charged pions, neutrinos are produced

$$\pi^+ \rightarrow \mu^+ \nu_\mu, \quad (2.3)$$

$$\pi^- \rightarrow \mu^- \bar{\nu}_\mu, \quad (2.4)$$

and the decay of neutral pions produces predominantly gamma rays

$$\pi^0 \rightarrow \gamma\gamma. \quad (2.5)$$

The minimum energy of those gamma rays is

$$E_{\gamma,\min} = \frac{m_{\pi^0} c^2}{2} = 70 \text{ MeV}, \quad (2.6)$$

making high- to very-high-energy gamma-ray detectors the perfect instruments to study the processes in **AGN**.

The acceleration processes of protons produce gamma rays and neutrinos. Neutrinos are neutral as photons and therefore carry the information about their origin's direction when measured on Earth. A neutrino detection and a gamma-ray flare, temporal and spatial coincident, supports the hypothesis of a hadronic acceleration scenario in AGN. For this reason, there is increasing emphasis in the scientific community on different experiments sharing data and results with each other. This sharing is the dawn of *multi-messenger astronomy*, which has become more prominent in recent years. There are considerations that there might be a time gap between the neutrino and the gamma-ray signal. Gamma rays interact with the matter in a very dense source region, whereas neutrinos escape directly. A subproject in the Collaborative Research Center SFB 1491² “Cosmic Interacting Matters” investigates these considerations. Time-resolved gamma-ray spectra are essential for understanding AGN and will be produced in this work.

Source regions emitting high-energy gamma rays have been cataloged by the Fermi Large Area Telescope (Fermi-LAT) satellite [21]. A skymap of the sources is shown in figure 2.3. The angular resolution of optical or radio telescopes is much higher than that of current VHE gamma-ray instruments, so assignments of individual sources are often difficult. For some gamma-ray sources, entire known galaxies are identified as counterparts. The drivers of the radiation are believed to be the central SMBH of these galaxies, having masses of millions of solar masses. During accretion of surrounding mass, the SMBHs can release enormous amounts of energy. If they do, these SMBHs are referred to as AGN. AGN are further classified by their emission in the radio range, their emission power, and the relative viewing angle to Earth, figure 2.4 gives a graphical overview. The *jets* are the parts in which the high-energy radiation is produced, they are oriented perpendicular to the accretion disk. During a description of 762 astrophotographies of nebulae and clusters, Curtis described the source Messier 87 as having a “curious straight ray [...] apparently connected with the nucleus by a thin line of matter” [42, p. 31], which is the first known observation of a jet. How exactly the transfer of energy works is under active research and largely unsolved. AGN with a jet pointing directly towards Earth are called *blazars*.

Most AGN gamma-ray spectra are well-described by a two-bump SSC model. Figure 2.5 shows the two-bump SSC model of Mrk 421, with data points from many experiments collected in [6]. AGN show a steep decrease in the spectrum at energies higher than about 100 GeV. The highest energies are attenuated by the absorption of the Extragalactic Background Light (EBL) [47], visible at around 10^4 GeV in figure 2.5. The interaction cross-section of VHE gammas with EBL

²<https://www.sfb1491.ruhr-uni-bochum.de>

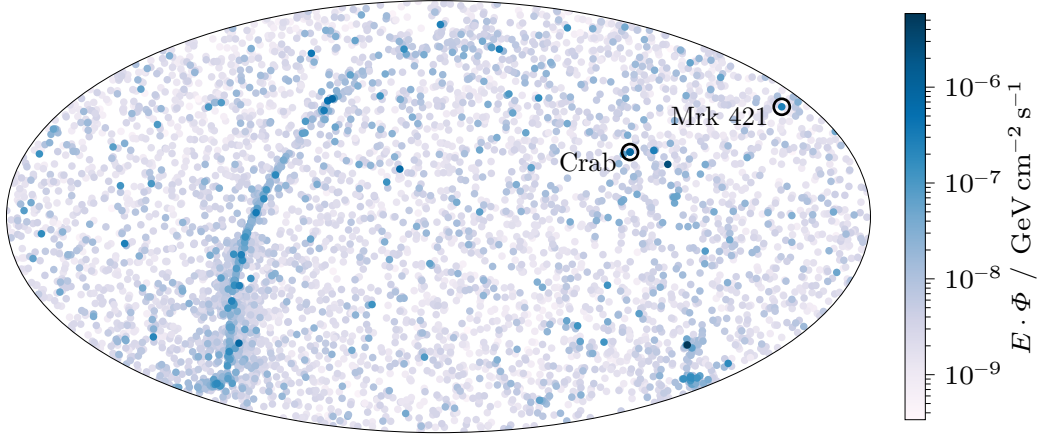


Figure 2.3: Fermi catalog of high-energy gamma-ray sources [7] in International Celestial Reference System (ICRS) coordinates. Mrk 421 and the Crab Nebula are marked with black circles. The accumulation of sources along the band in the left-hand side of the plot is the galactic plane.

photons,

$$\gamma_{\text{VHE}} \gamma_{\text{EBL}} \rightarrow e^+ e^-, \quad (2.7)$$

becomes larger with increasing energy. The EBL absorption effects are reduced in observations of nearby sources.

Blazars are interesting observational targets because

- they have excellent observation possibilities due to their strong and pointed jets emitting gamma rays,
- they can exhibit strong variability, which can give information about acceleration mechanisms and can be used to find counterparts, and
- since IceCube was able to assign neutrinos to AGN [62], they are considered to be possible neutrino emitters.

To best study AGN, one should choose nearby blazars. Mrk 421 is such a nearby AGN, a blazar in the constellation Ursa Major at ICRS coordinates $Ra = 166.114^\circ$,

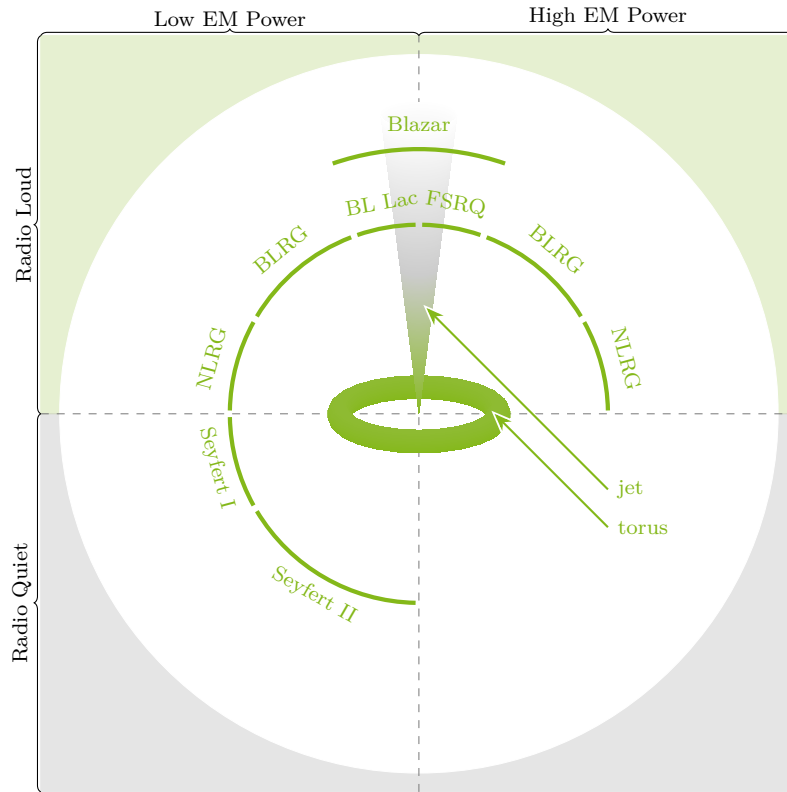


Figure 2.4: Overview of AGN types. Inspiration for this figure taken from [23, 48, 96, 97]. The classification is based on radio emission, electromagnetic power and the viewing angle of the jet. AGN with a jet pointing towards Earth are called *blazar*.

Dec = 38.209°, with a redshift of $z = 0.03$ [94, 102]. Mrk 421 was discovered first in the VHE gamma-ray energy range by the Whipple Observatory [88]. Since then different experiments regularly monitor it, e.g. the First G-APD Cherenkov Telescope (FACT) [17] and the Major Atmospheric Gamma Imaging Cherenkov (MAGIC) telescopes [74].

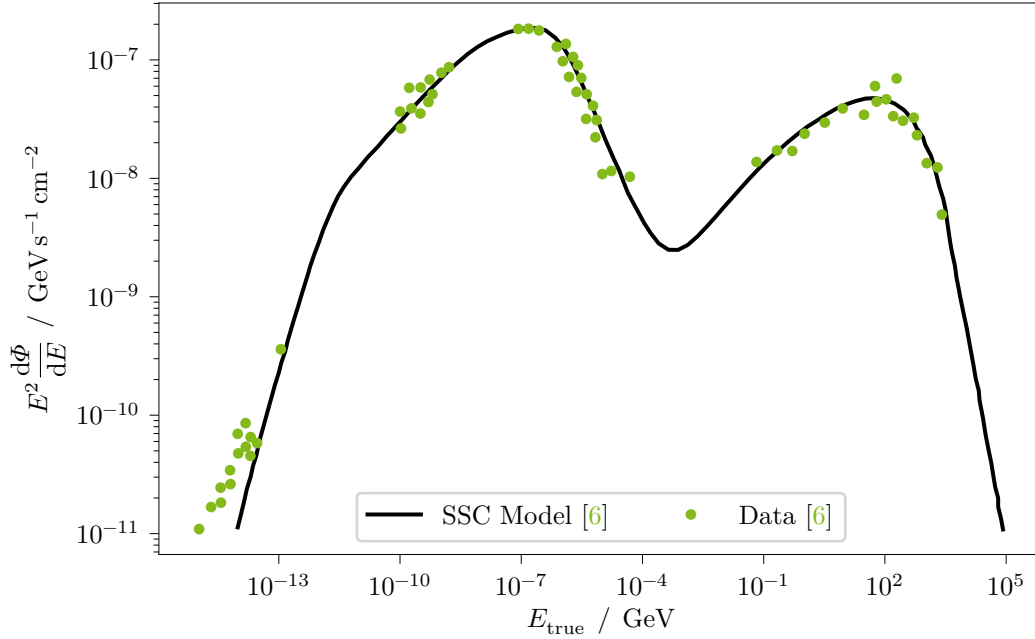


Figure 2.5: One-zone SSC model of Mrk 421. Data and model taken from [6, fig. 11]. Data extracted with [90].

2.2 Interstellar Medium and Messenger Particles

Particles accelerated in extreme environments like AGN pass through the interstellar medium on their way to Earth, in most parts an almost perfect vacuum. Nevertheless, there is the possibility of meeting some obstacles: galactic and intergalactic magnetic fields and dust clouds. Magnetic fields affect charged particles and deflect them, whereas neutral particles like photons and neutrinos are not affected. Protons and other charged cosmic rays are unsuitable for analyzing specific sources since these magnetic fields deflect them. Thus, the directional reconstruction of cosmic rays carries no information about the origin. Magnetic fields do not deflect gamma rays, but dust clouds attenuate them. Neutrinos are barely affected on their way to Earth due to their weak interaction and small effective cross-section, but these properties make it challenging to observe cosmic neutrinos. Neutrino detectors need huge collection volumes, e. g., a cubic kilometer of ice, as IceCube instruments at the South Pole [3].

Other possible messengers are gravitational waves, completing the field of multi-messenger astroparticle physics. The field is new and promises exciting insights into our universe for the coming decades, like the first multi-messenger campaign of a

binary neutron star merger [5], which was first observed through by the Advanced Virgo Interferometer (VIRGO) [8] and Advanced Laser Interferometer Gravitational-Wave Observatory (LIGO) [70] detectors.

2.3 Extensive Air Showers

Naturally, gamma rays are an excellent tool to study specific sources. Fortunately, Earth's atmosphere shields life from cosmic rays and gamma rays. In fact, gamma rays interact with the molecules of the atmosphere. When the gamma rays enter the upper layers of the atmosphere, they initiate processes in the electric fields of the atomic nuclei, distributing their energy. These scatter processes generate highly energetic electrons and positrons via pair production,

$$(Z+) \gamma \rightarrow (Z+) e^+ e^-. \quad (2.8)$$

Those particles are still of very high energy, that they generate photons via bremsstrahlung

$$(Z+) e^{-'} \rightarrow (Z+) \gamma + e^- \quad (2.9)$$

in the early state of shower development. Those photons are of such a high energy that the process repeats, in first order doubling the number of particles each cycle and halving their energy, until the energies are too low to further undergo pair production or bremsstrahlung. This simplification of the process is called the Heitler model [58]. It is displayed in figure 2.6. Other interaction processes are strongly suppressed [84]. Below the energy limit, the particles gradually slow down, and the process no longer takes place. However, the atmosphere is not opaque only to gamma rays. Also hadrons, mostly protons and helium nuclei, but also heavier particles like oxygen, carbon and iron, of similar primary energy induce air showers in the atmosphere. There are many more decay paths, such as pion production, muon production, or decay into other hadrons

$$p + N \rightarrow \pi^\pm + \pi^0 \dots \quad (2.10)$$

These interactions induce a cascade-like particle shower, like gamma rays do. Hadronic particle showers also produce electromagnetic sub-showers via

$$p + N \rightarrow \pi^0 + X, \quad (2.11)$$

$$\pi^0 \rightarrow \gamma\gamma, \quad (2.12)$$

as depicted in figure 2.7. These so-called Extensive Air Shower (EAS) can be measured by ground-based detectors. Two types of experiments are currently

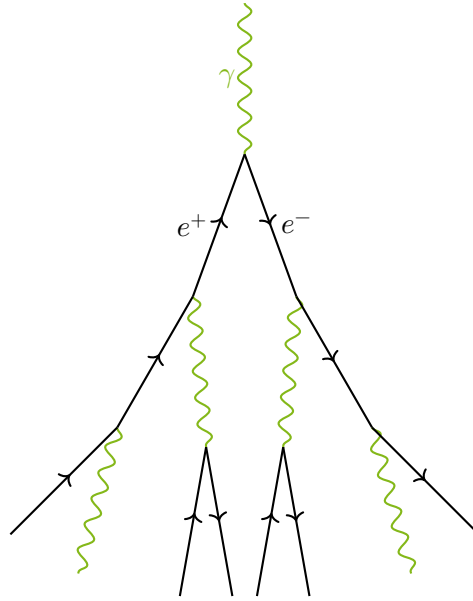


Figure 2.6: An air shower produced by a primary gamma, as described by the Heitler model [58]. In each generation, the number of particles double and the energy of the particles halve. Electrons and positrons are created by pair production and gammas by bremsstrahlung.

in operation: observatories such as the **High-Altitude Water Cherenkov Gamma-Ray Observatory (HAWC)** and the **Pierre Auger Observatory (PA)** use water-filled tanks to measure the particles of an **EAS**: the high-energy charged particles generate Cherenkov light in the tanks, which is collected with **Photomultiplier Tubes (PMTs)**. The other class of ground-based observatories are the **Imaging Atmospheric Cherenkov Telescopes (IACTs)**, which are discussed in detail in section 3.1. The particle showers produce Cherenkov radiation in the atmosphere. A major task of an analysis in Cherenkov astronomy is to separate showers initiated by hadrons from showers initiated by gamma rays, and reconstruct the primary particle's main properties: energy and direction. The number of hadron-induced particle showers is many orders of magnitude larger than that of gamma-induced ones, posing an additional challenge to the analysis. If a **VHE** particle would not create an **EAS**, it would travel in a straight path towards the Earth's surface. That path is called *shower axis*, and is one main characteristics to reconstruct the origin of the gamma ray.

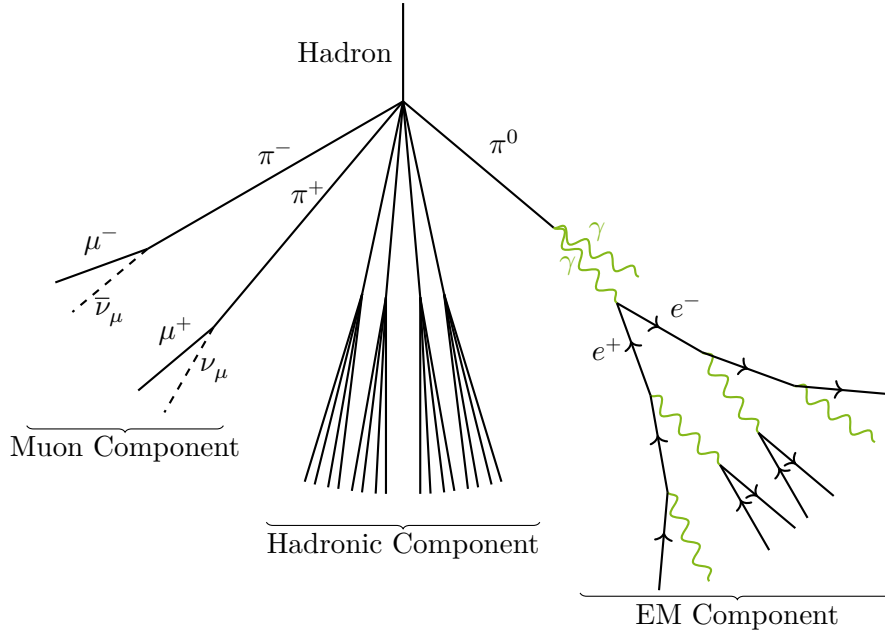


Figure 2.7: A hadronic air shower, producing a muonic component via charged pions and an electromagnetic component via neutral pions.

2.4 Cherenkov Radiation

Particles created in **EAS** can travel faster than the local speed of light in the atmosphere. The electromagnetic field of a fast charged particle moves at a constant velocity in a dielectric medium, polarizing the medium along its path so that the electrons attached to the atoms follow the waveform of the pulse as the particle passes [65]. If the speed of a particle is faster than the local speed of light, the electromagnetic waves are in phase and interfere constructively. A shock front is formed, as shown in figure 2.8, very similar to a mach cone known from audible systems. The opening angle of this shock front is derived as

$$\cos(\theta_c) = \frac{1}{n\beta}, \quad (2.13)$$

where n is the refractive index of the medium and

$$\beta = \frac{v}{c}. \quad (2.14)$$

Cherenkov light is produced by particles with $\beta > 1/n$. The maximum opening angle, for particles with $\beta \rightarrow 1$, is

$$\theta_{\max} = \arccos \frac{1}{n}. \quad (2.15)$$

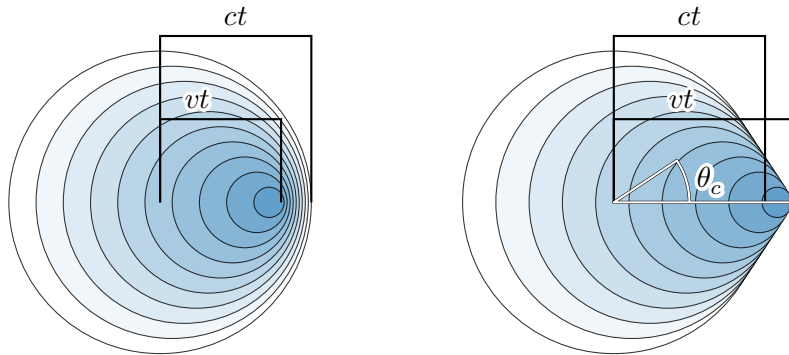


Figure 2.8: A sketch showing and explaining shock waves. On the left is a particle traveling with a velocity $v = \beta c$, where $\beta < 1$ and c the local speed of light $c < c_0$. On the right is a particle traveling with $\beta > 1$. One can see the shock-front developing conically. For a total duration time t , a wavefront is drawn as a circle at location vt_i with radius $r_i = c(t - t_i)$, where $0 \leq t_i < t$. The particle in the end is at position vt . The first wavefront (white) has a radius of ct .

This effect of emitting light is known as the *Cherenkov effect*. The Cherenkov light of **EASs** cannot be seen by eye, as the intensity is very low and especially the duration of an **EAS** is only tens of nanoseconds.

An **EAS** creates a *Cherenkov light pool* on the ground with its shock cone, in which the Cherenkov photon density is nearly constant. An **IAC** standing in the light pool detects the Cherenkov photons and thus the **EAS** generated by the primary particle.

3 Detection

Looking up into the night sky is looking into infinity—distance is incomprehensible and therefore meaningless.

Douglas Adams
The Hitchhiker's Guide to the Galaxy

In Cherenkov astronomy, earth-bound **Imaging Atmospheric Cherenkov Telescopes (IACTs)** are used to detect the faint flashes of light produced by **Extensive Air Shower (EAS)** via the Cherenkov effect. The following sections guide through the general structure and manner of operation of these telescopes, the currently observing experiments, an overview of the data analysis, and the future of ground-based Cherenkov astronomy: the **Cherenkov Telescope Array (CTA)** with its first **Large-Sized Telescope (LST)**.

3.1 Imaging Atmospheric Cherenkov Telescopes

IACTs can detect the faint and short flashes of Cherenkov radiation produced by superluminal particles in **EASs** created by incident **VHE** particles in the Earth's atmosphere. That causes the whole visible atmosphere to constitute the detector volume. The large detector volume makes **IACTs** much more suited for the lower count of higher energetic gamma rays, compared to satellite experiments like the **Fermi-LAT** [21], which are limited in volume.

The first Cherenkov detectors were built in 1959 at the Volcano Ranch in New Mexico, and they detected the first **EASs**, including a shower induced by a primary particle with a claimed energy greater than 10^{20} eV in 1962 [77]. The first **IACT** was the Whipple telescope with a collecting mirror of 10 m diameter, located in Arizona [101]. The second generation consists of the **High-Energy-Gamma-Ray Astronomy (HEGRA)** system, an array of five telescopes, each packing a camera made of **PMTs** [57], and ground detectors. In addition to the telescopes, further Cherenkov counters were installed. The current and future generation of Cherenkov

telescopes, as well as the telescopes of **HEGRA**, are all built on the same working principle, with significant differences in mirror area, computing power, number of pixels, and the overall quality of all components.

Current Cherenkov telescopes typically feature a segmented mirror made of hexagonal or square parabolic mirrors, forming a huge parabolic mirror, with the cameras located on an arc in the focal point. Alternatively, they can be built with two large mirrors facing each other, like the proposed **Schwarzschild-Couder Telescope (SCT)** [10] of **CTA**, where the camera is located in-between the primary and secondary mirror, the focal point of the secondary mirror.

The cameras consist of **PMTs** or **Silicon Photomultipliers (SiPMs)**, with hexagonal or quadratic light cones, detecting light reflected by the mirrors. Auxiliary devices are located in the center of the main dish to accommodate calibration measurements.

The current generation of **IACT** observatories are

- **the First G-APD Cherenkov Telescope (FACT)**, which is a single Cherenkov telescope located at the **ORM** on La Palma. **FACT** was the pathfinder Cherenkov telescope for **SiPMs**, which have the advantages of being very sensitive to low photon counts but are robust at the same time [16, 29]. The **SiPMs** of **FACT** can observe single Cherenkov photons while being operable at high currents as present in bright moon conditions.
- **The Major Atmospheric Gamma Imaging Cherenkov (MAGIC) telescopes**, a system of two Cherenkov telescopes with 17 m mirror diameter each. **MAGIC** is located at the **ORM** on La Palma [13], next to **FACT** and **LST-1**.
- **The High Energy Stereoscopic System (H.E.S.S.)**, an array of four 12 m mirror diameter telescopes placed on the edges of a 120 m square, with one large 28 m mirror diameter telescope at its center [53]. **H.E.S.S.** is located in the **Khomas highlands** of **Namibia** near the **Gamsberg** mountain.
- **The Very Energetic Radiation Imaging Telescope Array System (VERITAS)**, an array of four 12 m telescopes located at the **Fred Lawrence Whipple Observatory** in **Arizona**, with a slightly irregular footprint [86].
- **The Cherenkov Telescope Array (CTA)**, as described in detail below.

3.2 The Cherenkov Telescope Array

The next-generation ground-based gamma-ray observatory is the **Cherenkov Telescope Array (CTA)**. Once finished, it will consist of tens of telescopes located at two sites: the Paranal Observatory in the Atacama Desert in Chile and at the **ORM** at the canary island of La Palma, next to **MAGIC** and **FACT**. The sites are selected due to their remoteness and altitude, resulting in optical environments that are ideal for Cherenkov telescopes. Both observatories feature optical instruments for many decades, for example, the **Very Large Telescope (VLT)** at Paranal Observatory and the **Gran Telescopio Canarias (GTC)** at La Palma.

The **CTA** telescopes will have different types of architectures: the **Large-Sized Telescope (LST)**, the **Medium-Sized Telescope (MST)** and the **Small-Sized Telescope (SST)**.

The **LSTs** will have a segmented mirror, made from hexagonal tiles, with a total diameter of 23 m and a camera with 1855 **PMTs**. The **LSTs** are located at the heart of both arrays, on La Palma and at Paranal Observatory, with four **LSTs** planned each. They will provide the best array sensitivity in the lower energy regime from 20 GeV to 150 GeV [38, 40].

The **MSTs** will consist of 12 m mirror diameter and also a camera with 1855 **PMTs**. In the alpha configuration of **CTA** [37] La Palma will get nine **MSTs** and the Paranal Observatory 14. The **MSTs** will provide the best array sensitivity in the core range of **CTA**, from 150 GeV to 5 TeV.

The **SSTs** will comprise a Schwarzschild-Couder dual-mirror optical design. The primary mirror has a diameter of 4.3 m and the secondary of 1.8 m. The cameras of the **SSTs** will feature 2048 **SiPMs**. There will be 37 **SSTs** at the Paranal Observatory, and none on La Palma. The southern hemisphere has the better observing conditions for the galaxy, where **PeVatron** searches are done [35], while the northern hemisphere mainly has extragalactic sources, where high energy is limited by **EBL** absorption. **SSTs** will provide best array sensitivity from 5 TeV to 300 TeV.

The array layouts are designed to accommodate the expected count of gamma rays in the different energy ranges. Low-energy gamma rays are numerous and create showers with faint Cherenkov flashes, in conclusion needing few but large telescopes. High-energy gamma rays, on the other hand, create showers with a lot of Cherenkov light that can be observed by small telescopes but are relatively rare, meaning a larger detector volume is needed to observe them in high enough quantities. Compare figure 3.1 for the array layout with the different telescope types.

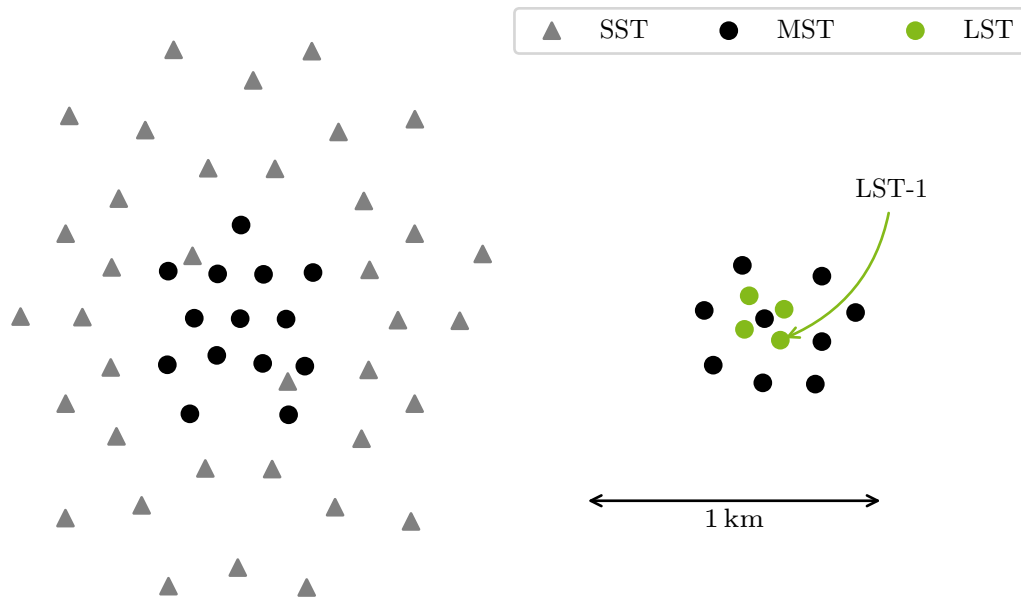


Figure 3.1: CTA South (left) and CTA North (left) array layout. North points upwards and East points rightwards. Data from the CTA alpha configuration [37]. Figure adapted from Brüggel [32].

All three telescope types have working prototypes at various locations, usually close to the institute where the architecture is developed and tested. The LST prototype is already at its final location at the ORM on La Palma. CTA is being operated as an open, proposal-driven observatory for the first time in VHE gamma-ray astronomy³.

3.3 The Large-Sized Telescope

The LST-1, shown during an observation in figure 3.2, being the prototype for the LSTs, is built on La Palma and was inaugurated in October 2018 [40]. It is currently in the commissioning phase to ensure the requirements by CTA are fulfilled and to further increase the telescope’s performance. The LST-1 has a mirror diameter of 23 m, and a focal length of 28 m, with a Field of View (FoV) diameter of 4.3°. For La Palma, three more LSTs are planned to improve the observation of the northern low-energy gamma-ray sky.

³<https://www.cta-observatory.org/about/how-ctao-works>

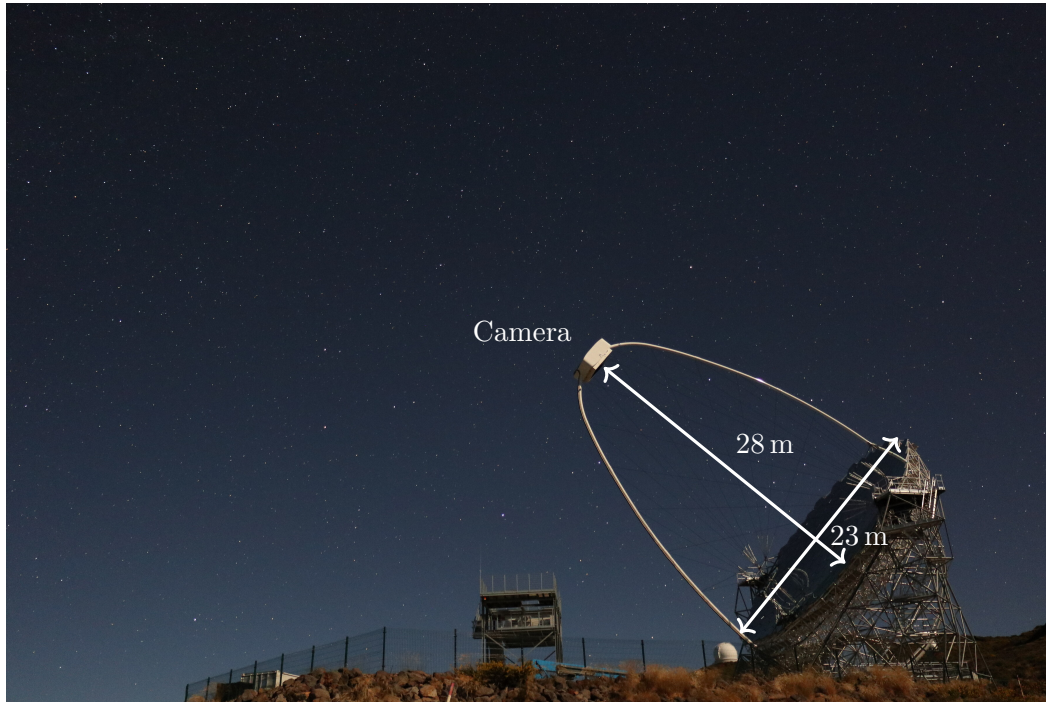


Figure 3.2: The LST-1 during an observation on La Palma. The main dish on the lower right-hand side is made up of 198 hexagonal mirrors, totaling at 396 m^2 mirror area. The camera at the center is held by carbon-fiber reinforced plastic arcs at a focal length of 28 m [40]. The tower at the lower center holds the camera during the day.

The LST-1 is capable of repositioning in 20 s to observe transient events and react to alerts by the multi-messenger and multi-wavelength communities. The low energy sensitivity of LST-1 [41] makes it possible to observe, among others, AGN at high redshifts and dark matter sources, both of high interest in the scientific community [35].

Observation Mode of the LST-1

During a typical night of LST-1 observations, preparations must be made before the observation starts. First, with a closed lid, the camera is operated with a periodic trigger. The events are used for the estimation of electronic noise in the pixels. Second, with an opened lid, the camera triggers periodically. These events are called *pedestals*. They do not contain Cherenkov flashes, but noise created by the Night

Sky Background (NSB). The pedestals can be used to describe the darkness of the night. For final calibration purposes, the camera is fully illuminated by bright light sources for the so-called *flat-fielding* events [95].

Events are triggered when a module containing seven pixels exceeds a certain threshold. When this happens, the **Data Acquisition (DAQ)** reads out all camera pixels that were sampled with 1 GHz, digitized into 40 values, resulting in a waveform of 40 ns duration [95].

LST-1 observes in the so-called *wobble-mode*. The telescope points so that the region of interest is not in the camera center, but off by 0.4° . Areas in the camera without the region of interest but with the same distance to the camera center can be used for background estimations. This way, background measurements can be taken simultaneously during an observation instead of needing a separate background measurement.

3.4 Data Analysis

The pixels of **IAC**Ts are made up of **PMT**s or **SiPM**s. They measure time series of voltages created by the Cherenkov photons. The readout window of these time series is generally sampled in a GHz regime, with a duration of tens of nanoseconds. Current and future **IAC**Ts have around two thousand camera pixels.

In the first step, the telescope triggers and the time series of each pixel are read out and saved into one *event*. The data provided by the camera must be calibrated. This step extracts the number of incoming photons and the mean arrival time from the waveforms. Next to the Cherenkov light, background noise like electrical noise is measured by the **PMT**. During calibration, the noise is estimated and extracted from the signal. Only a fraction of all camera pixels contain the actual Cherenkov signal of an event. The others consist mainly of background noise. That makes it possible to reduce the amount of data significantly by discarding those pixels that most likely contain only background noise. This data reduction step must be done carefully to not discard faint events or other sought-for features in some events.

The calibrated and reduced data must now be cleaned by a thorough algorithm that removes pixels that contain no Cherenkov light. The cleaning threshold level depends on the weather, **NSB**, and source environment. Extragalactic sources have reduced background noise compared to galactic sources due to their dark surroundings, making it easier to clean such events.

The remaining pixels form the shower image, representing the shower in the camera. These images with hexagonal pixels are not yet usable for classical machine learning algorithms. Therefore, the showers are parameterized into a set of features describing the shape of the signal, its location in the camera, containment, and brightness. These parameterized event lists are fed into machine learning algorithms to reconstruct the particle types, their energies, and directions. The aim is to identify the gamma events and reject the hadronic ones. The gamma-like events, the events that are likely gamma-induced and reconstructed as such, are kept and further analyzed to highly-reduced products such as *SEDs*.

4 Simulation and Analysis

It is important to draw wisdom from many different places.

Uncle Iroh

Avatar: The Last Airbender S02E09 *Bitter Work*

Before observing at all with **Imaging Atmospheric Cherenkov Telescopes (IACTs)**, the specificities of the instrument must be known, as well as the detector's response to **Extensive Air Showers (EASs)** produced by gammas or hadrons. To do this, intensive **Monte Carlo (MC)**-simulations are used. First, all properties of the individual components are described. Second, these properties are used to simulate **EASs** with the Cherenkov light, and the detector response, including telescope structure and mirror reflectivity, as well as the **PMT** responses, the readout electronics and the trigger. The simulated data must go through the same analysis chain used for observed data to include all known effects correctly. The analyses make heavy use of **Machine Learning (ML)** algorithms, where, i. e., **Random Forests (RFs)** are trained on known **MC** truth to predict properties of the observed events: the particle's type, its energy, and direction. A list of gamma-candidates is created from all reconstructed events to be further used in the *high-level* gamma-ray analysis.

Each part of the simulation, the **MC** analyses, and the high-level analyses, are described in detail in the following sections. The results of the different steps in an analysis of observed data from LST-1 are shown in **chapter 5**.

4.1 Simulation

The initial primary particles are simulated, their interactions in the atmosphere, and the detector response to the Cherenkov light produced in the air shower.

Two programs are used for the **MC**-simulation of the events: first, **Cosmic Ray Simulations for Kascade (CORSIKA)** simulates the particle interactions in the atmosphere [56]. The most important interaction processes in electromagnetic showers are pair production and bremsstrahlung (see **figure 2.6**), and an exemplary result

of a vertical shower induced by a 100 GeV proton is shown in figure 4.2. The `CORSIKA` extension `IACT/ATMO` [27] by Konrad Bernlöhner simulates the production of Cherenkov light in an air shower. `CORSIKA` propagates those Cherenkov photons to the ground.

`sim_telarray`, also developed by Konrad Bernlöhner, takes care of the detector simulation [26]. The photons produced by `CORSIKA` get ray-traced through the optical system of the detector, where mirror degradation and impureness are taken care of by randomly sampling them. In addition, `sim_telarray` takes into account and simulates the `PMT` response of the camera, producing waveforms for each pixel. Such a waveform is shown in figure 4.1.

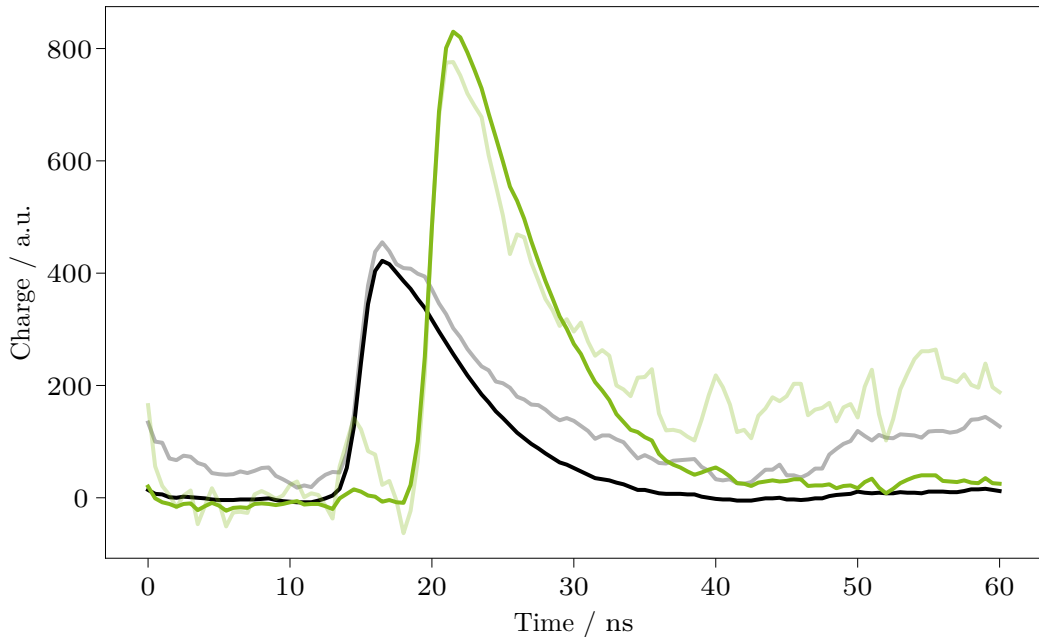


Figure 4.1: Waveform of two pixels hit by Cherenkov photons, as `sim_telarray` simulates them. Shown are the measured (transparent) and calibrated (opaque) waveforms.

Air Showers

`CORSIKA`, the software that simulates the interactions of the particles in the atmosphere, was developed for the `KARlsruhe Shower Core and Array DETector` (`KASCADE`) in the 1990s [56]. `KASCADE` is a particle shower experiment that is

now no longer operated. Nevertheless, the simulation software is still widely used, see e. g. [39]. **CORSIKA** is further developed continuously at Karlsruhe Institute of Technology (KIT). **CORSIKA** consists of several configurable modules to calculate particle interactions and cross-sections. Among these modules are for low-energy interactions **Fluka** [51] and **URQMD** [22], see [81] for a comparison. Current **CTA** simulations use **CORSIKA** 7 with a modified **EGS4** code for electromagnetic interactions [25, 79]. For the new **CORSIKA** 8 [49, 89], a module for electromagnetic interactions is the **Propagator with optimal precision and optimized speed for all leptons (PROPOSAL)**, which is developed at the chair in Dortmund [66, 92]. **PROPOSAL** was originally created to calculate muon cross-sections. Different modules simulate interactions in different energy ranges and take, depending on the complexity of the interaction and thus its simulation, more or less time. Especially high-energy interactions lead to large computational efforts. **CORSIKA** takes the incident particles, computes interactions of these and all created secondary particles, and propagates all particles to their termination. Particles either reach the ground, decay into secondary particles, or lose energy to below a minimum energy, beyond which the particles are no longer considered relevant because their contribution to the air shower is estimated to be small. A 100 GeV proton, simulated by **CORSIKA**, is shown in figure 4.2. The secondary **EAS** particles are not directly measurable by **IAC**Ts, since they measure the Cherenkov radiation emitted only by the superluminal particles. For each particle, the **CORSIKA** extension **IAC**T/ATMO simulates the emitted Cherenkov radiation and propagates the Cherenkov photons to the telescopes. The output data from the **EAS** simulation are the Cherenkov photons, each with a certain wavelength and direction, at locations on the ground⁴.

Detector

The software **sim_telarray** is used to simulate the detector response to Cherenkov photons, which come from the atmospheric simulation **CORSIKA** with the extension **IAC**T/ATMO. The Cherenkov photons are ray-traced through the optical detector system. Ray-tracing is a technique that is also used in modern computer games [87]. The photons, starting at their locations on the telescope sphere with a specific direction, are propagated in a straight path until they hit a surface. If this surface is the telescope structure, the photon is absorbed and not propagated further. If the photons hit a mirror, they are reflected and propagated further. The wavelength-dependent absorption and reflection of each mirror are considered. The law of reflection states that the angle of incidence equals the angle of reflection. However, no real mirror is perfect. Therefore, a slight random deviation is included to simulate

⁴To be precise: At this stage, the telescopes are modeled as spheres.

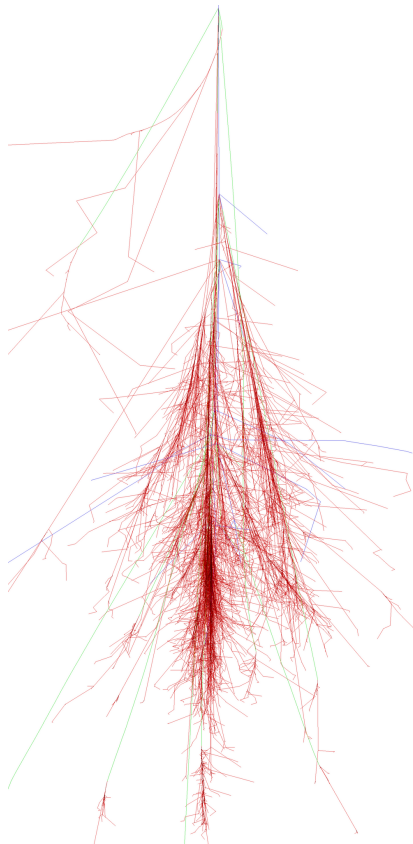


Figure 4.2: A 100 GeV proton air shower simulated with `CORSIKA` [93]. In red the hadronic particles are shown, and electrons and photons in green. The muonic component is shown in blue.

the mirror imperfections systematically. This way, the telescope's performance is not overestimated by knowingly ignoring inaccuracies. Photons can also propagate past the mirrors, in which case they are discarded. All others are reflected by the mirrors. Again, some hit the telescope structure or miss the camera. Of course, these are also no longer considered. Of much more interest are those photons which hit the camera.

`sim_telarray` also takes care of the propagation of the photons through the camera optics. First comes the protective camera glass, where photons can be reflected or transmitted, with a certain probability depending on their energy. Furthermore, `sim_telarray` simulates the light guides of the `PMTs`. The individual response curves of the `PMTs` are considered. Technical details about the `PMTs` used in LST-1 are in [40]. The output data of the detector simulation are the response curves

of each PMT, which correspond to the camera’s pixels. Two typical curves are displayed in figure 4.1.

`CORSIKA` with the simulations of the air showers is much more computationally intensive than `sim_telarray` with the simulations of the detector response for a single telescope. For that reason, `sim_telarray` has clever mechanics to simulate the same telescope multiple times for a single `EAS` to see them from multiple angles and thus get more simulated telescope responses. For that, the telescopes can be moved around in the Cherenkov light pool. With `sim_telarray`, the instrument response of single telescopes can be simulated, but also, as the name suggests, whole telescope arrays. With the simulation of telescope arrays, the performance of the `CTA` can be studied, and the final configuration of the telescope locations can be optimized [9, 25].

4.2 Low-Level Analysis

This section introduces the low-level analysis of simulated and observed data. The analysis does not distinguish between the two. The low-level analysis is used to bring the raw simulated or measured waveforms to reconstructed gamma-like event lists, including the training and application of `ML` models, detailed in section 4.3.

`ctapipe` is the low-level prototype pipeline for `CTA` [68, 72]. `ctapipe` takes the simulated and observed data from raw waveforms (Raw Data 0, R0) to reconstructed event lists (Data Level 3, DL3). While doing so, it calibrates the waveforms, integrates them in a central interval to *extract* the signal, and calculates a peak time. This creates two images per event, which get cleaned from noise: the charge image and the peak time image, see figure 4.4. These images are parameterized, and `ML`-methods are applied to those parameters to reconstruct event properties: particle type, energy, and arrival direction.

Calibration

The waveforms of the `PMTs`, `Raw Data 0 (R0)`, might be noisy due to thermionic emission in the `PMTs`. The noise can be reduced by constantly cooling the `PMTs`, but only partially avoided. Also, the `PMTs` differ from each other, e.g., due to production differences. In the calibration step, `PMTs` are adapted to each other. The results are reasonably smooth curves, as shown in figure 4.1. Pixels that have not been hit by Cherenkov photons show roughly a constant line. Those pixels that were hit by Cherenkov photons contain a more or less visible peak,

depending on the contained charge. The calibrated data is referred to as **Raw Data 1 (R1)**.

In this step, the data can already be reduced conservatively for the first time. Pixels that clearly contain no Cherenkov photons can be discarded. However, this must be done with great care, since anything contained in the removed data is irretrievably lost. Nevertheless, the data size can already be reduced by more than 90 %, as can be seen in [figure 4.4](#), where only ~ 100 of 1855 pixels contain signal.

Signal Extraction

The signal is extracted from the **R1**, the calibrated and possibly reduced response curves of the **PMTs**. In LST-1, the **DAQ** reads out with 1 GHz, and the response curves are about 40 ns long, which correspond to a data size of 40 data points [95]. These are now further reduced by determining two values for each pixel: the so-called *peak time* and *charge*, i. e., Cherenkov photon count of the pixel.

There are several ways to determine these two values, in the simplest case the location of the peak of the waveform is searched, resulting in the peak time. Then the curve can be integrated in a window around the peak to calculate the charge. This step is called signal extraction.

Since these two values are determined for each pixel, from now on, the data consists of two camera *images* per event. One consists of the photon charge, the other of the corresponding peak time. In [figure 4.3](#) is shown which pixels contain Cherenkov photons from the **EAS**: the charge is much higher compared to the rest of the camera. It also shows that the peak times of the shower signal are similar to each other. The background pixels are easily distinguished from the signal pixels in both images. First, by the low number of contained Cherenkov photons, second by the randomly distributed peak times.

After the signal extraction, the data has **Data Level 1a (DL1a)**, which is also referred to as *image level*.

Image Cleaning

The next step is image cleaning, separating the signal pixels from the background pixels. Different algorithms are developed, the simplest being *tailcuts cleaning*, which considers only the charge image. Two thresholds are defined: the core threshold q_c and the boundary threshold q_b . In the first step, all pixels below q_c are discarded. The remaining pixels are combined into the so-called core pixels. In the second step, all pixels adjacent to the core pixels are added to the core pixels, as long as they are above the boundary threshold q_b and have at least two neighboring core pixels.

As shown in figure 4.3 and figure 4.4 and discussed before, the relative peak times are also an excellent way to separate signal pixels from background pixels. Other cleaning algorithms also use this information, one being used by MAGIC [12]. For example, in a step before applying the boundary threshold q_b , it is required that the relative deviation of two neighboring pixels does not exceed a time threshold Δt . The cleaned images are still called DL1a.

As described below, the cleaned images are typically parameterized to reduce data size further and to clear the path for ML-based analyses. In recent years, deep learning-based analyses have gained traction [63, 80], which typically use Convolutional Neural Networks (CNNs) and are applied directly on the image level or even on the calibrated waveforms.

Image Parameterization

Cleaned images can have different shapes and sizes. Cherenkov photons can hit a few or many pixels and illuminate them strongly or weakly. The signal may be entirely inside the camera or be incomplete at the edge. To summarize this information, including describing the quality of the event, the images are parameterized. The parameterization of images was popularized and first used by Hillas in 1985 [60]. On the cleaned charge image of an event, a Principal Component Analysis (PCA) is performed, yielding a first set of parameters. The first and second moments of this PCA can be identified as long and short semi-axis of an ellipse. An example of such an ellipse is overlaid on a toy-simulated image in figure 4.9. The location of the signal in the camera is determined by a weighted average, resulting in the *center of gravity* or *cog*. Further parameters describe the extension of the signal in values of the light distribution. For example, one parameter determines which part of the signal distribution is contained in the three brightest pixels. Other parameters specify the pixel or intensity proportion of the shower pixels in the outer one- or two-pixel rows. The parameters can be used to gain information about the primary

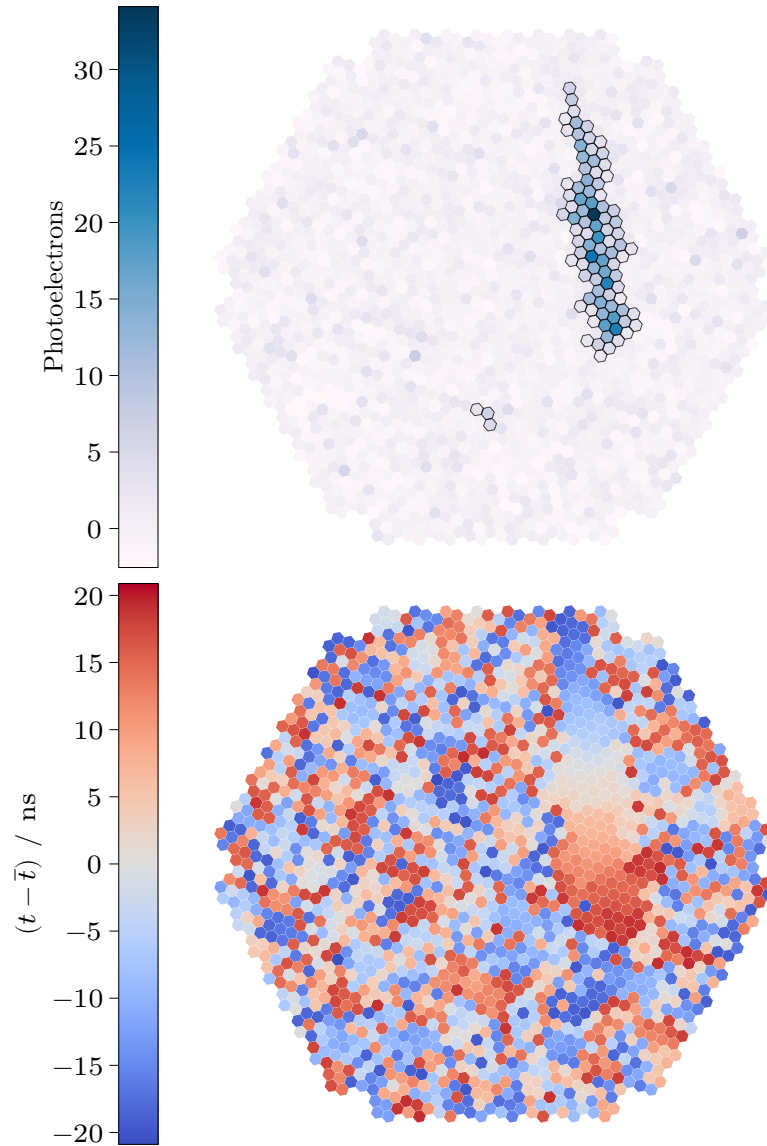


Figure 4.3: A gamma event at DL1a, before image cleaning, as simulated via `CORSIKA` and `sim_telarray`. On the top is the charge image, where the signal is clearly visible. On the bottom is the peak time image, subtracted by the mean peak time of shower pixels. In peak time image the noise is even more pronounced than in the charge image.

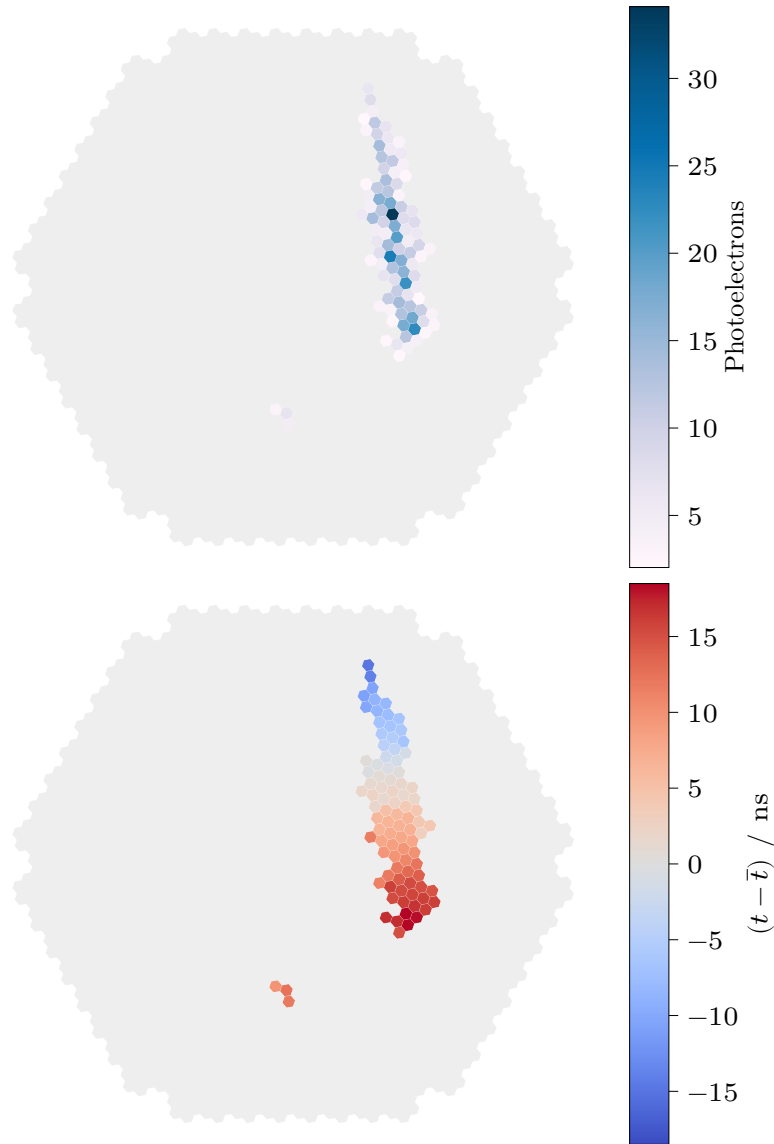


Figure 4.4: A gamma event at DL1a, after tailcuts cleaning, as simulated via `CORSIKA` and `sim_telarray` and analyzed by `ctapipe`. On the top the charge image and on the bottom the peak time image. The cleaned pixels comprise less than half of all camera pixels.

particle: the sum of the collected shower photons, the *intensity*, is correlated with the primary particle's energy, and the projected shower axis is close to the major shower axis, the first moment of the PCA. Figure 4.5 shows the correlation between the intensity and the primary energy. With multiple telescopes triggering the same

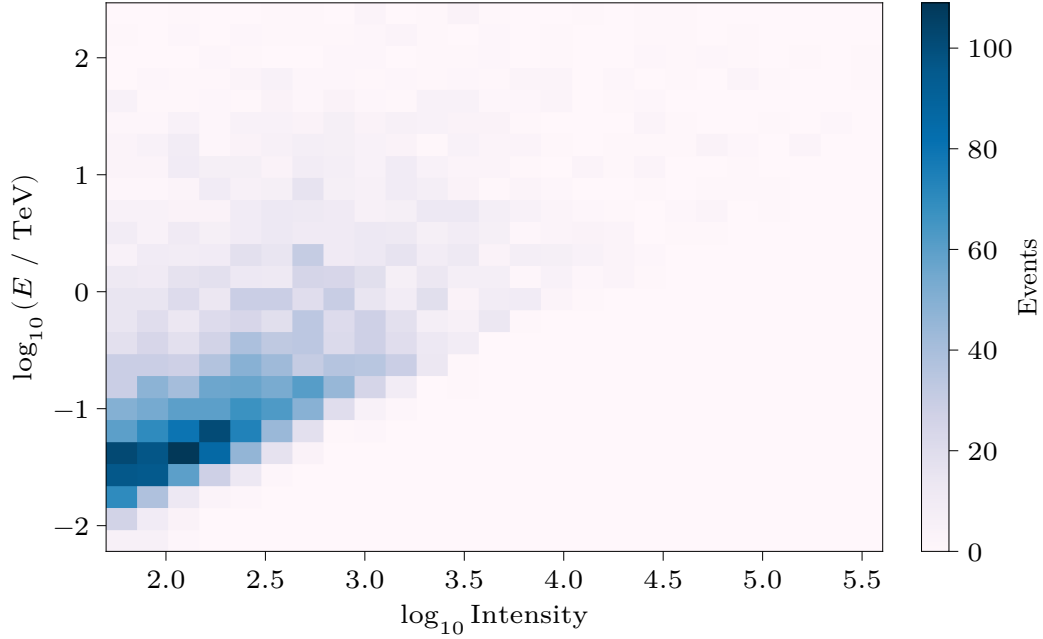


Figure 4.5: Correlation of intensity, the sum of shower photon charges, and energy of the primary gamma ray. A clear correlation is visible. To reconstruct the energy other dependent variables are needed.

event, further geometric calculations can be made to estimate the arrival direction of the incident particle. The parameterized events are called **Data Level 1b (DL1b)** and referred to as *parameter level*.

The reconstruction of the direction, the energy, and the type of the primary particle are performed with machine learning algorithms. The methods of the machine learning approach are described in the following.

4.3 Machine Learning

Machine learning refers to computer programs that can generate knowledge from experience. Machine learning models are trained on the relationships between a set of measured parameters X and one or more target variables y and can interpolate

and extrapolate. In machine learning, one distinguishes supervised and unsupervised learning. In supervised learning, there must necessarily be true target variables y ; in unsupervised learning, there are not. Unsupervised learning is often used to group similar data, called clustering, or to find out unknown relationships. Unlike unsupervised learning, supervised learning requires a dataset where the truth about variable y is known, this dataset is called labeled. The true relationships can be learned on labeled data, here simulations, and can be used to produce a predicted target \hat{y} . In Cherenkov astronomy, supervised machine learning is used. The known targets are the properties of the initial particles of the simulation. As mentioned earlier, there is a relationship between the image parameters and the properties of the primary particles: energy, direction, and particle type. The machine learning methods learn the relationships between the parameters X and the particle's properties, the target y , as well as multidimensional dependencies. For example, a bright image is associated with a high primary energy, compare figure 4.5. Multivariate methods can help tremendously.

Machine learning methods need to be validated and tested. For this purpose, the simulated datasets for the machine learning-based analyses are divided into a training dataset, a validation dataset, and a test dataset. The training dataset is used to infer the relationships between the features X and the target variables y . The validation of the models prevents *overtraining*: if the model predictions perfectly mirror the training dataset, it suffers in predictive power on other data. To deal with this problem, the validation dataset is available. During training, the learning procedures are adjusted to yield similar performance on both the training and validation datasets. This ensures that the machine learning agent is not overtrained, meaning it cannot generalize. During validation on known truths, it is verified that the model can be applied to data other than the training data and still give meaningful results. Thus, the training and validation dataset is effectively known to the learner. The final performance of this machine learning algorithm is evaluated on the test dataset at the end of training once an acceptable performance on the training and validation dataset is reached. The machine learning method's generalization performance is evaluated on the test dataset.

In the actual application, *cross-validation* is often used to check the performance of the machine learning method. First, the entire dataset is divided into a cross-validation and test datasets. The test dataset is, as before, not considered during the whole training process, only for the performance evaluation afterward. Cross-validation consists of several identical steps. In each step, the cross-validation dataset is divided into training and validation datasets. A new machine learning model is trained for each of these dataset combinations. Thus, cross-validation creates a set of trained models that should all perform equally well. If one or more perform significantly differently from the others, it is clear that the model's

architecture is insufficient to gather enough information about the target variables. The data in one step may be selected to partially overtrain, or not enough learning may have occurred. The selected machine learning method is unsuitable for learning the correlations, and a different architecture or set of variables must be selected.

Broadly, two types of supervised machine learning methods are regressors and classifiers, which are essentially based on the same training process. However, the differences lie in the evaluation of performance and the goodness criterion, sometimes called *loss*, used in learning. The goodness criterion describes the difference between the prediction and the known truth.

The quality criterion for a regressor in this analysis is the **Mean Squared Error (MSE)**,

$$\text{MSE} = \frac{1}{n} \sum_{i=1}^n (y - \hat{y})^2. \quad (4.1)$$

In this, upward and downward deviations are weighted equally, and larger deviations are weighted stronger. The evaluation of a regressor is given by three values: the r^2 value, a statistical quantity indicating the proportionality of two variables,

$$r^2(y, \hat{y}) = 1 - \frac{\sum_i (y_i - \hat{y}_i)^2}{\sum_i (y_i - \bar{y})^2} \quad (4.2)$$

with

$$\bar{y} = \frac{1}{n} \sum_i y_i. \quad (4.3)$$

The resolution and the bias of the prediction are further performance evaluation metrics, and are calculated in bins of the true target y using the ratio of the predicted and true value

$$\mu_i = \left(\frac{\hat{y}}{y} \right)_i, \quad (4.4)$$

where $i \in \{\text{Bins of } y\}$. The resolution is the binned inter-quantile distance

$$R_i = \frac{q_{84.1}(\mu_i) - q_{15.9}(\mu_i)}{2}, \quad (4.5)$$

and the bias is its mean

$$B_i = \text{mean}(\mu_i). \quad (4.6)$$

Constant and known biases can be corrected, whereas large resolutions cannot.

The quality criterion of a binary classifier is the cross entropy

$$H = -p \log(p), \quad (4.7)$$

where p is the assigned probability of belonging to one class, the *classification threshold*. From the confusion matrix

$$\begin{pmatrix} \text{tp} & \text{tn} \\ \text{fp} & \text{fn} \end{pmatrix}, \quad (4.8)$$

with the true positives tp , the true negatives tn , the false positives fp , and the false negatives fn , the quality criteria true positive rate and false positive rate are calculated as

$$\text{tpr} = \frac{\text{tp}}{P} = \frac{\text{tp}}{\text{tp} + \text{fn}}, \quad (4.9)$$

$$\text{fpr} = \frac{\text{fp}}{N} = \frac{\text{fp}}{\text{fp} + \text{tn}}. \quad (4.10)$$

Here, P and N are the total classified positives and negatives respectively. Both the true and false positive rate are functions of the classification threshold. Both rates are plotted against each other in figure 4.6. The resulting curve is called **Receiver Operator Characteristic (ROC)**. The **Area Under Curve (AUC)** determines the performance of a classifier. It ranges from 0.5 at the diagonal to 1, which is a perfect classification.

The machine learning functionality of `ctapipe` is capable of training and applying scikit-learn [85] based reconstructors. The application of reconstructors to events is the step to take the data to **Data Level 2 (DL2)**. **DL2** event lists contain events with reconstructed arrival direction, estimated energy, and particle identification.

Random Forests

A common ML-method are ensembles of binary decision trees, namely **Random Forests (RFs)**. Binary decision trees can be used for both regression and classification. In a binary decision tree, a cut is sought in each step that splits the dataset. The cut should minimize the Shannon entropy in both split datasets. The entropy of a dataset Q with size n is defined as

$$H(Q) = \sum_m \frac{n_m}{n} H(Q_m), \quad (4.11)$$

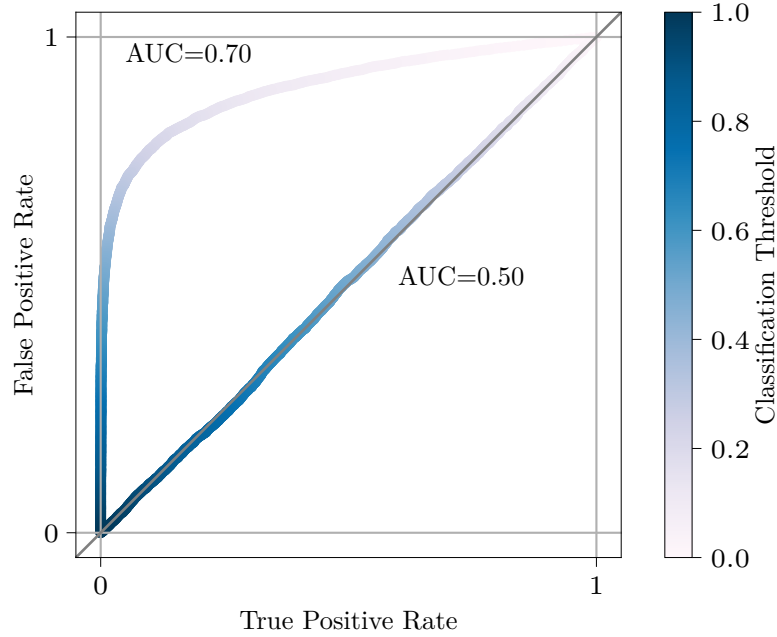


Figure 4.6: ROC and AUC for a classifier and random guesses. The diagonal gray line is identical to random guessing of the class. The color corresponds to the classification threshold.

where Q_m are the partial datasets with size n_m . The information gain

$$I = H(Q) - H_{\text{exp}}(Q | a) \quad (4.12)$$

is the difference between the entropy and the expected entropy H_{exp} after a cut on feature a , and must be maximized when deciding on a cut. Entropies vary, depending on whether a classification or regression is performed. In classification, the Gini coefficient

$$H_{\text{Gini}} = p(1 - p) \quad (4.13)$$

or the cross entropy

$$H_{\text{CE}} = -p \log(p) \quad (4.14)$$

is used. In both cases p is the probability of belonging to one class. In regression, the MSE

$$H_{\text{MSE}} = \frac{1}{n}(y - \bar{y})^2, \quad (4.15)$$

is often used. Thus, the cut is optimized according to (4.12), on the variable a that works best for it. In each of the splits, the procedure is now repeated until one of several conditions occur: either the maximum depth of the tree is limited, or the size of the partial dataset.

Binary decision trees are not continuous methods; instead, they approximate step functions. Therefore, decision trees are unsuitable for extrapolations of the target variable y . A decision tree has a strong tendency to overtrain and a high variance. These problems can be minimized by randomly generating statistical changes to the training that reduce the variance in exchange for a higher bias. Furthermore, multiple decision trees can be combined. Randomness and multiple trees make a **RF**.

A **RF** is a combination of several binary decision trees that are randomly varied. In normal **RFs**, there are two cases of randomness. First, each decision tree is trained on a random subset from the training dataset, this is called *bagging*. In this case, this decision tree cannot represent the entire dataset and, therefore, must be able to generalize better. Second, only some variables are used to optimize the cuts. Thus, each decision tree sees only a subset of all variables, reducing the chance of a single decision tree overtraining. The prediction of a **RF** regressor is typically an average of the predictions of all included decision trees, and **RF** classifiers take a majority vote or the average prediction.

Binary decision trees and random forests are a white box machine learning method. In contrast to the black box, a white box model can explain how a decision was made. Thus, with **RFs**, it can also be seen very well how important a variable is for the prediction. This is called *feature importance*. The importance of a feature can be determined by looking at how large the proportion of the training dataset is, which is divided by a cut on that feature.

Particle Identification

Particle classification is essential in gamma-ray analyses because, as mentioned earlier, the hadronic air showers look very similar to the gamma-induced air showers and come in much larger numbers. In gamma-ray astronomy, a separation of these two classes is needed. This classification is done with machine learning methods, using a two-class classification to separate signal from background: gammas from non-gammas. For this, both gammas and protons are simulated. Other classes could be simulated, for example, electrons or heavy nuclei, like iron. In the training of the particle classifier, the value one is assigned to the gammas and a zero to the protons. The model must predict a number between zero and one, the so-called *gammaness*. It indicates the fraction of trees in the **RF** that have classified the events as class one and thus as gamma-like. Protons get a number close to zero, and gammas get a number close to one. In the cross entropy (4.14), the quality criterion of a two-class classifier, the gammaness equals p . Since the gammaness is not a binary value that gets predicted but a continuous score from zero to one, the threshold that

distinguishes between the two classes must be chosen. This classification threshold is later called the gammaness cut, see section 5.3. It can be optimized on simulations, as is done and described in section 5.3.

Energy Regression

The energy is one of the central properties to be reconstructed about the gamma rays. The energy is a continuous variable, therefore a regressor is used. The regressor

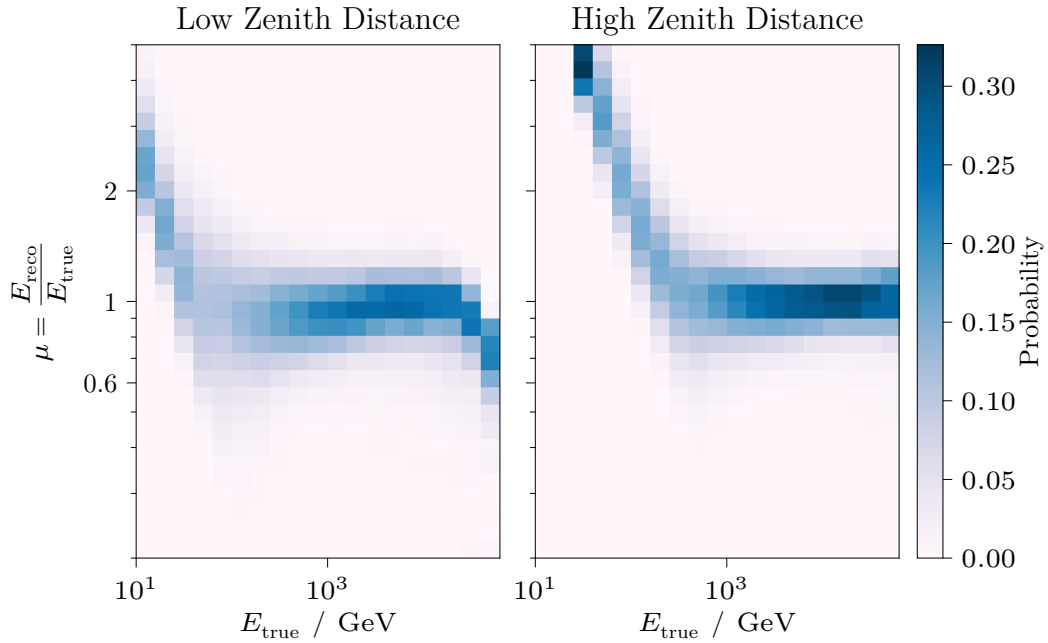


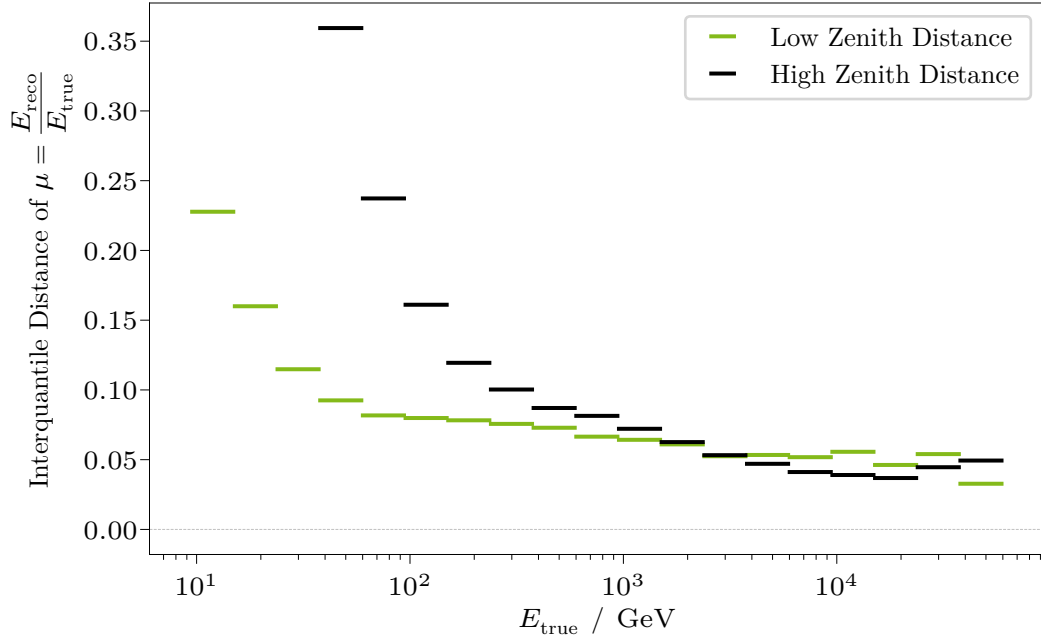
Figure 4.7: The energy migration matrix, also called energy dispersion, of a single model evaluated on two distinct datasets.

is optimized based on the **MSE**. The energy of the observed gamma rays spans several orders of magnitude. In a quality criterion like the **MSE**, larger deviations are weighted more heavily. This would mean that a machine learning algorithm weights high energies more heavily since the deviations are more strongly perceived here. Thus, the energy estimator would be poor at low energies. This is remedied by estimating the logarithm of the energy $\hat{y} = \log_{10}(E)$. The logarithm has a smaller range of values and no longer spans several orders of magnitude. Thus, it is possible to treat all energy ranges equally. Figure 4.7 shows the migration matrix of a single energy estimator evaluated on two distinct test datasets. The migration matrix shows the probability with which an event is reconstructed from a bin of true energy

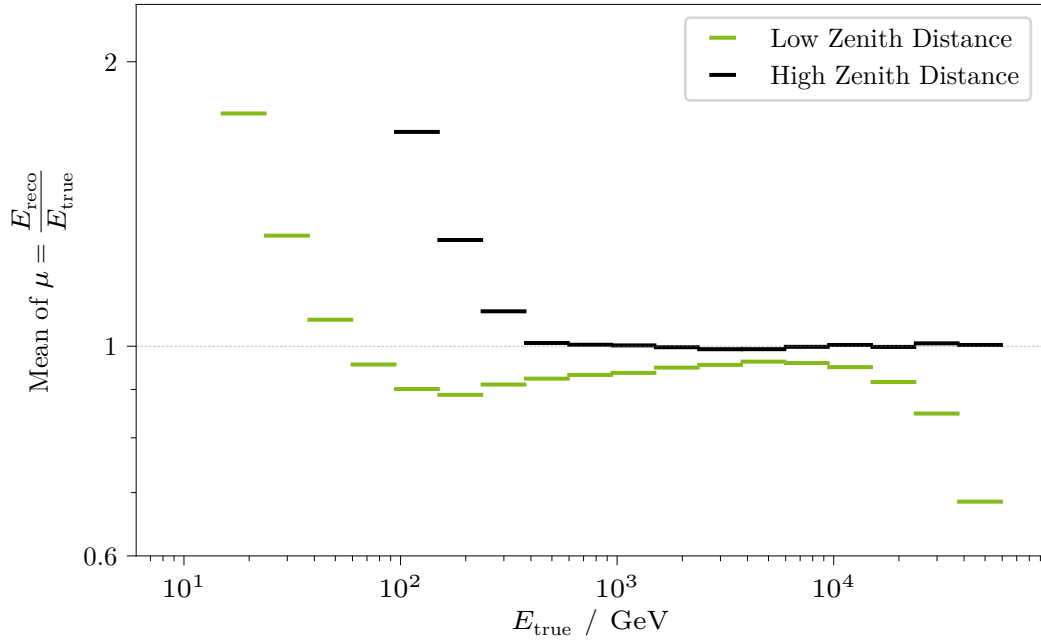
into a bin of estimated energy. Figure 4.8a shows the resolution (4.5) and figure 4.8b the bias (4.6). It clearly shows that the resolution is better at high than low energies. At low energies, the background rate plays a major role. Imperfect image cleaning throws away more signal than at high energies, and there is less signal to begin with. In the bias, it can be seen that low energies are overestimated, and high energies are underestimated. This is also a common effect: the simulated energy range is limited, and a machine learning method can meaningfully only learn and estimate energies in the simulated range. At the lowest energies, smearing into neighbor bins is only possible into higher energies, and vice versa: the opposite effect is to be considered in the high energy range. The effect is systematically reflected in the first and last few bins. In addition, close to the energy threshold, the surviving triggered events are rather untypical ones, brighter than the mean, resulting in a positive bias.

Direction Reconstruction

The *disp method* is a method of direction reconstruction for Cherenkov telescopes. It is necessary for mono observations, i. e., when only one telescope is observing, or for mono events, when only one telescope has triggered. Both is the case for the LST-1. In the image parameterization, the major axis of the PCA is expected to coincide with the shower axis. Due to the limited resolution of IACTs, the values may differ, nevertheless, the main axis of the camera image is a good approximation of the shower axis. However, the source can be anywhere along this axis, and its exact position still needs to be determined. This is where machine learning regression comes into play. The regressor determines how far away the source position is from the *center of gravity*. The perpendicular distance to the main shower axis, which arises by the insufficient resolution, is neglected. Since two points satisfy this condition, a classifier determines the direction of the source. Based on figure 4.4, one can easily imagine that the time slope along the main shower axis is a good variable for this. From the two predicted values, distance to the center of gravity, *norm*, and its direction, *sign*, the source position is determined in camera coordinates as shown in figure 4.9. Using the telescope position and orientation, the source position can then be determined in horizontal coordinates, and by including the timestamp transformed to equatorial coordinates.



(a) Resolution of the energy regressor. For both test datasets the energy resolution gets better at higher energies.



(b) Bias of the energy regressor. For both test datasets the bias is larger than 1 for the low energies.

Figure 4.8: Resolution (4.5) and bias (4.6) of the energy regressor. The two lines correspond to two different test datasets, explained in chapter 5.

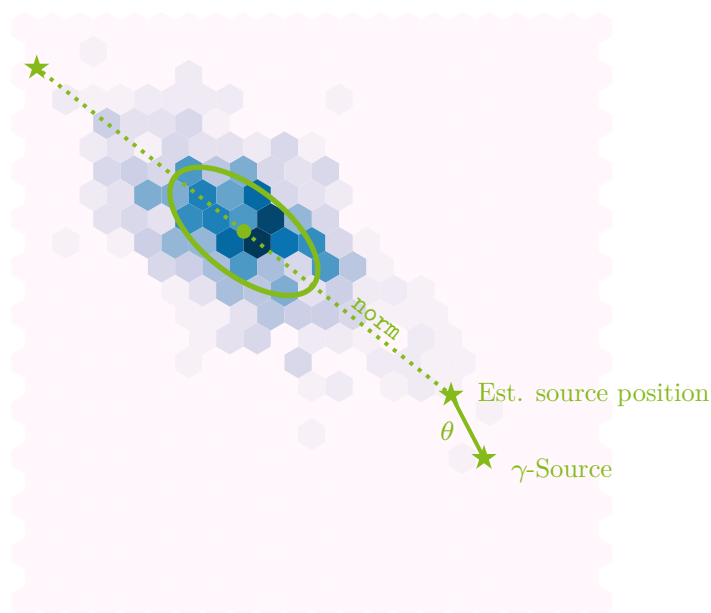


Figure 4.9: Explanation of the *disp method*: A shower is shown with its first and second moment of the PCA overlaid as an ellipse. The predicted distance to the source position is shown for both possible signs. The estimated source position lies on the main shower axis. It is still a little off from the known source, the distance is called θ , which can be used for background estimation as explained in the main text in section 4.4.

4.4 Instrument Response Functions

Data Level 3 (DL3) is the first public data level, consisting of reconstructed gamma-candidates, containing their estimated direction, estimated energy, and trigger time.

In addition to the event lists for each observation, which typically consists of a single run of around 20 min, the Instrument Response Functions (IRFs) are part of a DL3 file. The IRFs describe all known detector properties. IRFs are parameterized descriptions of a detector and are calculated from simulations. They describe the detector response to a particle with a certain primary energy E coming from a certain direction p . They additionally depend on the particle type, telescope orientation ψ , and time t , as well as atmospheric effects, such as density and transmission, and detector wear, such as mirror degradation. In the following, \hat{p} and \hat{E} are the

estimated direction and energy of the true values p and E . The detector response R is generally

$$R \rightarrow R(\hat{p}, \hat{E} | p, E, \psi, t). \quad (4.16)$$

However, such a high-dimensional description of the detector is computationally costly. Therefore, IRFs are factorized and decomposed into components given for time intervals in which they are assumed to be constant. The IRFs are thus reduced per observation to

$$R_{\Delta t} \rightarrow R(\hat{p}, \hat{E} | p, E), \quad \text{where } \Delta t = t_{\text{stop}} - t_{\text{start}}. \quad (4.17)$$

This still multi-dimensional function is factorized into three individual functions which further decrease the dimensionality

$$\begin{aligned} R(\hat{p}, \hat{E} | p, E) = & \\ & A_{\text{eff}}(p, E) \quad \text{Effective Area} \\ & \times \\ & E_{\text{disp}}(\hat{E} | p, E) \quad \text{Energy Dispersion} \\ & \times \\ & \text{PSF}(\hat{p} | p, E) \quad \text{Point Spread Function.} \end{aligned} \quad (4.18)$$

Effective Area

The first step is to see how many simulated particle showers are triggered by the telescope, classified as gamma events, and reconstructed well enough to be used in the high-level analysis. Because of the cuts in gammaness and the resulting loss of gamma events, the analysis chain is part of the detector response. Many particle showers with low energy are not measured by the telescope, because they produce too little Cherenkov light to trigger. High-energy particle showers, on the other hand, can illuminate the camera very strongly, so the reconstruction capability decreases. The detection probability is energy-dependent. The probability of detecting a particle is calculated on simulations as a function of the true energy E of the particle and its direction p . At this point, events have no reconstructed energy since undetected events do not pass through the analysis chain. In order to be able to specify the reconstruction probability in a system-independent way, it is described as effective area:

$$A_{\text{eff}}(p, E) \quad (4.19)$$

The effective area is the area an ideal detector with an efficiency of 1 must have to measure the same number of events as the real detector with an efficiency below 1.

The simulated area must, therefore, be included in the determination of the effective area,

$$A_{\text{eff}} = \frac{n_{\text{reconstructed}}}{n_{\text{simulated}}} A_{\text{simulated}}. \quad (4.20)$$

The effective area is a quality parameter that allows comparisons across experiments. The entire measurable area must be simulated in order to determine a reasonable effective area. The effective area is multiplied by the effective time of the observation to get the *exposure*

$$e = A_{\text{eff}} t_{\text{eff}}. \quad (4.21)$$

Energy Dispersion

The second factor of the IRFs is the energy dispersion. It gives the probability with which a particle of a true energy is assigned a reconstructed energy. The probability is always smeared around the truth due to the detector's finite resolution and the particle showers' stochastic nature. It is naturally energy-dependent and corresponds to the migration matrix of the energy regressor as presented in the previous section 4.3.

Point Spread Function

The third part of the IRF factorization is the Point Spread Function (PSF). Not to be confused with the optical resolution of the telescope, the PSF gives the probability density of reconstructing a particle's location. The PSF is energy-dependent, and depends on the reconstructed location in the camera. The PSF is usually considered to be radially symmetric in the camera, depending only on the distance to the camera center, and at each position is considered to be radially symmetric. This approximation is sufficient for mono-observations at low zenith distance.

For point-source analyses, as performed in observations of known extragalactic sources, the PSF can be reduced even further. Here, a region around the known source position is simply cut out, and the PSF in this region is assumed to be constant. The PSF is thus reduced to a delta function at the source location in camera coordinates

$$\text{PSF}(\hat{p} | p, E) \rightarrow \delta_{\hat{p}} \text{PSF}(E), \quad (4.22)$$

reducing the IRF to

$$R(\hat{p}, \hat{E} | p, E) \rightarrow R(\hat{E} | E). \quad (4.23)$$

However, since directional reconstruction is still energy dependent, the size or radius of the source region at \hat{p} can be given energy dependent.

4.5 Background Estimation

Furthermore, the expectation of background events in the field of view must be specified. In typical observations, the background events are measured during the observation, using the observation method *wobble-mode*. In wobble-mode, the telescope is pointed slightly off-center, in the case of LST-1 0.4° next to the assumed source position. The advantage of the wobble-mode is making the background measurement at the same time as the original observation, maximizing the available observation time of the target at a slightly reduced efficiency by measuring not at the camera's center.

The position where the source is assumed in camera coordinates is called *on-region*. Because the camera's efficiency is radially symmetric, all regions with the same distance to the camera center are IRF-equivalent to the on-region: the *off-regions*. These regions can have a fixed or energy-dependent radius, θ_{\max} . Figure 4.10 shows the on- and off-regions for the telescope's FoV.

The off-regions contain N_{off} events. Given a sufficient direction reconstruction, they contain no gamma-ray events from the observed source. The on-region contains N_{on} events, which stem from source and background events:

$$N_{\text{on}} = s + b, \quad (4.24)$$

where s is the number of source events, and b the number of expected background events

$$b = \alpha N_{\text{off}}, \quad (4.25)$$

where α is the ratio between on- and off-region observation time, or in the case of wobble-mode the inverse of the number of off-regions. The source counts s or *excess* are consequently

$$s = N_{\text{on}} - \alpha N_{\text{off}}. \quad (4.26)$$

These relationships can be used to calculate a significance of detection according to Li and Ma [69]

$$S_{\text{LiMa}} = \sqrt{2 \left\{ N_{\text{on}} \ln \left[\left(\frac{1 + \alpha}{\alpha} \right) \left(\frac{N_{\text{on}}}{N_{\text{on}} + N_{\text{off}}} \right) \right] + N_{\text{off}} \ln \left[(1 + \alpha) \left(\frac{N_{\text{off}}}{N_{\text{on}} + N_{\text{off}}} \right) \right] \right\}}. \quad (4.27)$$

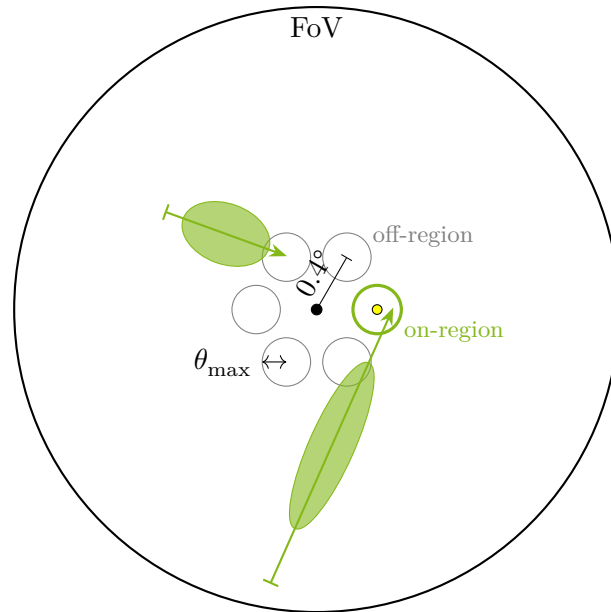


Figure 4.10: Selection of on- and off-regions for data from observations in wobble-mode. The center black dot is the telescope pointing. The green circle marks the on-region, with the yellow dot inside marking the source position. The on- and off-regions are displayed as circles with a wobble offset of 0.4° . The radius of the regions θ_{\max} can be fixed or energy-dependent.

The shower images of two events are overlaid, with the shower signal shown as a green ellipse and the reconstructed source position as an arrow tip. The longer shower is reconstructed as an *on-event*, possibly signal, and the shorter as *off-event*, background.

For each DL3 gamma-ray event, the angular distance to the observed source position is calculated. This is done for the on-events as well as the off-events. The squared distances are binned, and in the case of a strong source, the signal histogram peaks about zero, and the background histogram is flat. The most dominant background here are misclassified hadrons.

4.6 High-Level Analysis

In contrast to the low-level analysis from the previous sections, the high-level analysis is about the production of highly reduced data, which summarizes the characteristics of the source, removes the detector-specific response, and makes them comparable

among experiments.

The results of the high-level analysis can be used to build and verify source models, observe temporal and periodic changes in the source's behavior, and combine observations from different experiments. The last point is crucial because many experiments map only a part of the electromagnetic spectrum. However, for a full description of a source, it is essential to know about the whole electromagnetic spectrum, the *multi-wavelength* description, or go even further into the territory of *multi-messenger* analyses. High-level results have the detector response extracted from the observed data and thus are independent of the experiment.

Two high-level results are of central importance in the analysis of **Active Galactic Nuclei (AGN)**. The first is the **Spectral Energy Distribution (SED)**, the differential energy flux. For point sources it is the number of particles per energy and area and time,

$$\frac{d\Phi}{dE} = \frac{d^3 N}{dt_{\text{eff}} dA_{\text{eff}} dE}, \quad (4.28)$$

for extended sources additionally per solid angle $d\Omega$. The flux can be determined in two ways:

1. Forward folding of parameterized flux models,

$$\arg \min_{\vartheta} \{\text{Poisson}[\text{Counts}, \mathbf{R} \times \Phi(\vartheta)]\} \quad (4.29)$$

where \mathbf{R} is the discrete detector response and $\Phi(\vartheta)$ is the binned spectral model with parameters ϑ . The Poisson loss is minimized with regards to the parameters ϑ .

2. Unfolding, detailed discussion in [chapter 6](#).

For known models, forward folding is appropriate because it usually has fewer parameters to fit. Unfolding, on the other hand, is model independent, but must be regularized to suppress unphysical oscillations in the result.

The second important high-level result is the **Light Curve (LC)**. The LC shows the total or binned integrated energy flux for time intervals. The light curve is often divided into time intervals corresponding to observations, about 20 min, or whole nights. A LC can also be divided into finer bins for events with short durations, such as flares.

Gammapy

In the past, many experiments have developed and operated their own analysis chains. Currently, the scientific community's consensus is moving towards open science, and CTA will be operated as an open observatory. This suggests that the analysis software should also be open-source. CTA selected Gammapy as the official science tool for high-level analyses [36]. Gammapy is a publicly developed open-source Python package for gamma-ray astronomy [43], built on top of the scientific Python stack. In addition to its mission for CTA, it is also tested in analyses of H. E. S. S. [54], MAGIC, and VERITAS. The high-level analysis in Gammapy is capable of doing forward folding of spatial, temporal, and spectral models and the calculation of SEDs and LCs. Gammapy currently lacks an implementation of unfolding. Part of this work is to develop a prototype for unfolding algorithms in Gammapy and its proof of concept. More on unfolding and the results in chapter 6.

5 LST Analysis

Moonlight drowns out all but the
brightest stars.

J. R. R. Tolkien
The Lord of the Rings

This chapter explains the steps necessary to perform a point-like analysis of LST-1 observations. This analysis makes use of the scientific Python stack [55, 100, 61] as well as `astropy` [18, 20, 19], `iminuit` [45, 64], `Gammapy` [43] and the workflow manager `snakemake` [76]. Important command line tools and packages used within and their respective versions used throughout this chapter are

- `lstchain` version 0.9.13 [73],
- `pyirf` version 0.6.0 [82],
- `ctapipe` version 0.12.0 [67],
- `Gammapy` version 1 [43].

5.1 Data Selection

In this analysis, the same runs are used as in the LST-1 paper on analyses of different AGN (in preparation). The data selection is performed on auxiliary data taken during the observations. Statistical measures are proposed that are consistent with the selection cuts used in the paper.

The analyzed source is Mrk 421. The first step is to look at the run list⁵ and select those observations where Mrk 421 was observed. The corresponding time range is selected to use only those runs used in the paper, namely from 2020-12-12 to 2022-05-23. After removing runs with issues in the calculation of pedestals and those with slight mispointings, 228 runs are kept. The angular distance between the reported pointing of the telescope and the source of all kept runs is between 0.35°

⁵https://lst1.iac.es/datacheck/lstosa/LST_source_catalog.html (protected)

and 0.45° . The mean pedestal charges in all pixels and especially their standard deviation are a good measure for the consistency of the NSB. In figure 5.1, the pedestal charge standard deviation of all pedestals in a single run is shown in relation to the moon elevation and illumination at the observation time. It is shown clearly that having the moon below the horizon yields constant pedestal standard deviations. Since the illumination of the moon is the main factor for the NSB, it is a good proxy for the residual background light. A two-sigma band around the mean value of pedestal standard deviations where the moon is below the horizon is used for the selection cuts. This keeps some runs with a low-risen moon where it is only slightly illuminated.

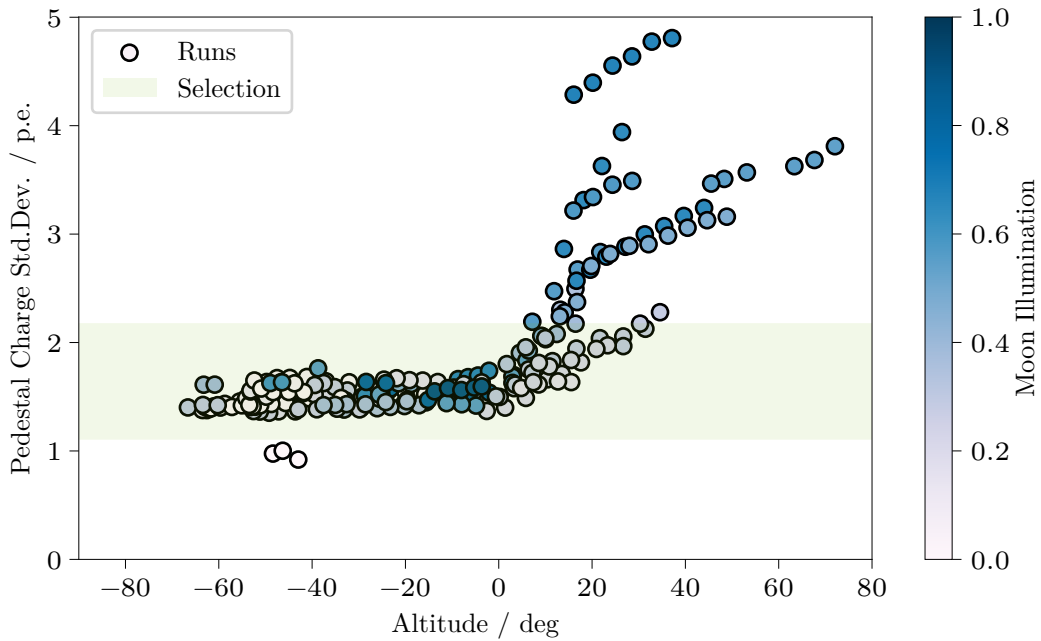
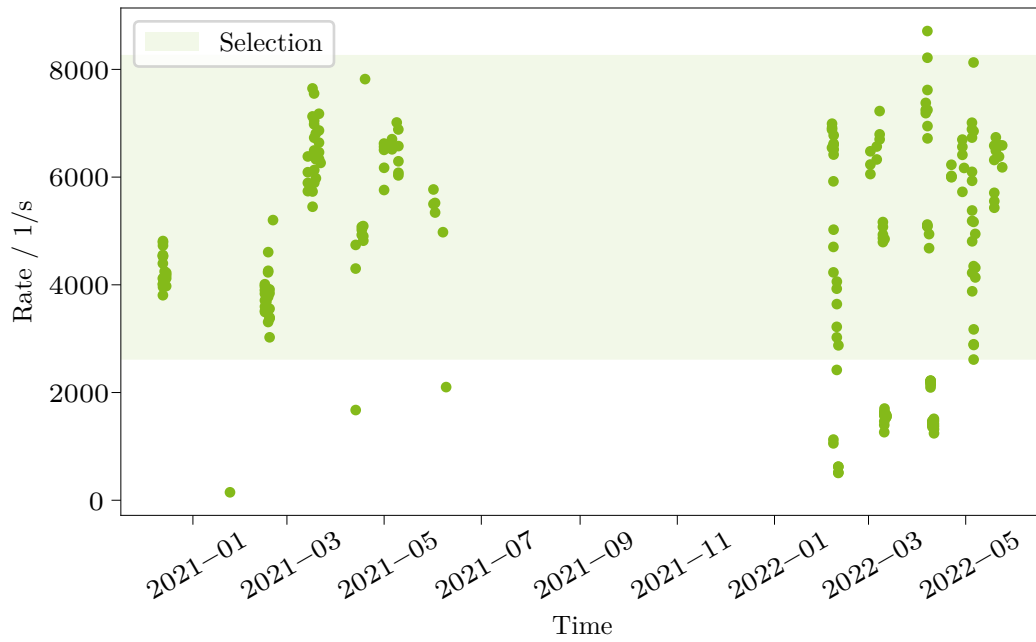
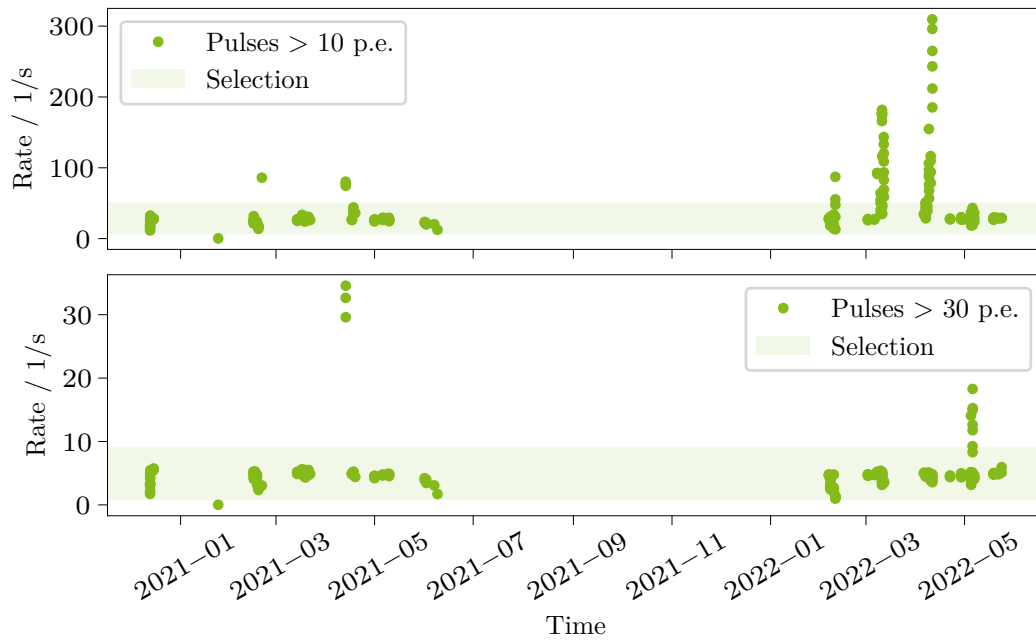


Figure 5.1: The pedestal charge standard deviation is shown against the moon elevation for each run. Color-coded is the moon illumination. The brighter and higher the moon, the more the pedestal standard deviations are spread out. A two-sigma band (green area) around the mean of the pedestal charges where the moon is below the horizon is used to keep some moon data.

Additional runs are discarded after looking at the rate of all triggered events, called *cosmics*, in figure 5.2a, and of those where the *intensity* of the cosmics is greater than 10 p.e. and 30 p.e., respectively, in figure 5.2b. Table 5.1 shows the cuts as described above. After all cuts there are 146 runs left, which add up to a total



(a) Rate of triggered events of all runs kept after the pedestal selection from figure 5.1. A two-sigma band (green area) around the mean discards further runs.



(b) The rate of triggered events with *intensities* above 10 p.e. and 30 p.e.. The rates are quite stable, but a two-sigma band (green area) around the mean still removes some outliers.

Figure 5.2

Table 5.1: Cuts as calculated by two-sigma bands as described in the main text.

Parameter	Lower Limit	Upper Limit
Pedestal Charge SD	1.1	2.2
Cosmics Rate (s^{-1})	2.6×10^3	8.3×10^3
Pulses above 10 p.e. (s^{-1})	6.3	51
Pulses above 30 p.e. (s^{-1})	0.8	9.1

observation time of 41.65 h. The total list of run IDs and their corresponding night can be found in [appendix 1](#).

5.2 All-Sky Monte Carlo Simulation

The LST-Collaboration provides so-called *All-Sky MC* simulations that are produced by the 1stMCpipe team [52]. Here, training data for declination lines of various possible sources and a grid of test data nodes are simulated, covering the whole sky. This way, models are trained per declination line, allowing the use of a model trained on similar pointing conditions as the observed data. First, the energy regressor is trained, then the direction reconstruction with the disp method (compare section 4.3 and figure 4.9), and afterward, the particle classifier, which includes the reconstructed energy and direction in the training features. To cover the whole declination with a good model, the telescope's pointing is included as a feature. Then IRFs are created for each test node, and the nearest to the observed data must be selected. Figure 5.3 shows an overview of the test nodes and the training declination lines.

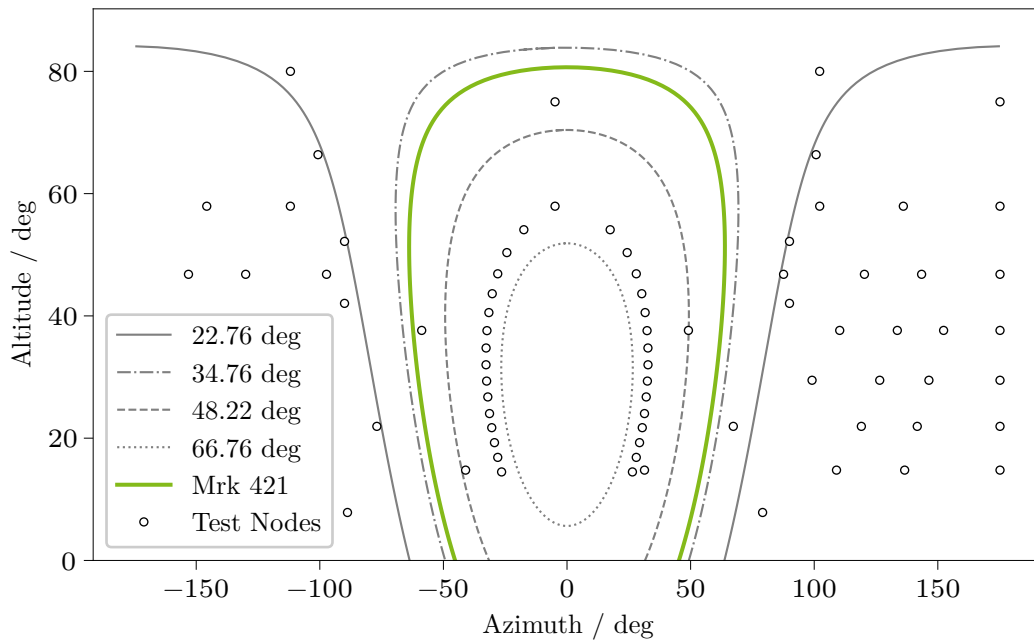


Figure 5.3: Overview of the All-Sky MC, with its test data nodes as white circles. The lines are the declination lines for which models are trained in this MC-production. The green line corresponds to the declination line of Mrk 421; the solid gray line at 22.76° is the one used for analyses of the Crab Nebula. Note that some test nodes are hidden behind the figure legend.

The nearest test node for to match IRFs to observations is calculated for as the minimal euclidean distance between the nodes and the telescope pointing

$$\text{node} = \min_{i \in \text{nodes}} \sqrt{(x_i - x_{\text{tel}})^2 - (y_i - y_{\text{tel}})^2}, \quad (5.1)$$

with

$$x_j = \sin \delta_j, \quad (5.2)$$

$$y_j = \cos \delta_j, \quad (5.3)$$

where δ is the angular separation between the telescope's pointing and the direction of the field lines of the Earth's magnetic field. The angular separation, or great-circle distance, is calculated using the Vincenty formula [99]

$$\delta = \arctan \frac{\sqrt{(\cos \theta_{\text{tel}} \sin \varphi)^2 + (\cos \theta_B \sin \theta_{\text{tel}} - \sin \theta_B \cos \theta_{\text{tel}} \cos \varphi)^2}}{\sin \theta_B \sin \theta_{\text{tel}} + \cos \theta_B \cos \theta_{\text{tel}} \cos \varphi}, \quad (5.4)$$

with

$$\varphi = \varphi_{\text{tel}} - \varphi_B, \quad (5.5)$$

where φ is the azimuth or longitude and θ the altitude or declination. The variables are also displayed in figure 5.4.

The Earth's magnetic field direction is calculated using an online calculator⁶ which uses the 13th generation of the International Geomagnetic Reference Field [14]. For the LST-1 coordinates

$$\text{lon} = -17.891\,39^\circ, \quad (5.6)$$

$$\text{lat} = 28.761\,39^\circ, \quad (5.7)$$

$$\text{height} = 2.184\text{ km}, \quad (5.8)$$

at the date 2021-12-01, the magnetic field lines directions are

$$\theta_B = B_{\text{inc}} = -37.36^\circ, \quad (5.9)$$

$$\varphi_B = B_{\text{dec}} = -4.84^\circ. \quad (5.10)$$

Although the magnetic field changes, it is assumed to be constant in the time range selected here, and it is also constant in the production of the test datasets, which were created around the same time. The associations in the aforementioned

⁶https://geomag.bgs.ac.uk/data_service/models_compass/igrf_calc.html

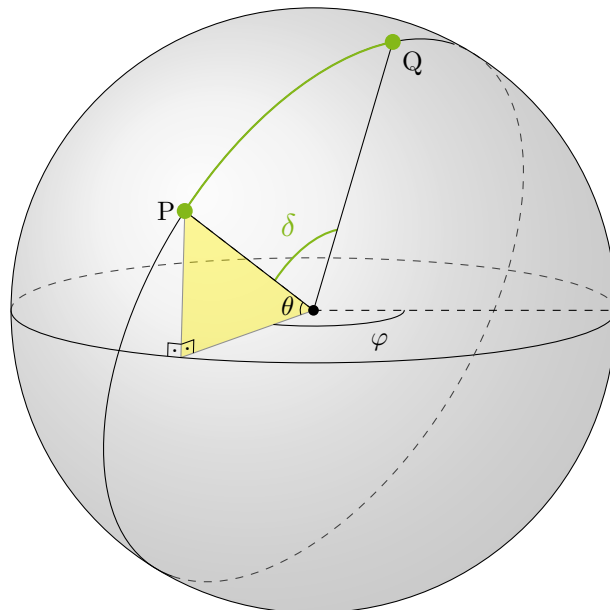


Figure 5.4: The great-circle distance, or angular separation (green). φ is the azimuth/longitude and θ is the altitude/declination. The points P and Q have an angular separation of δ (green), calculated with the Vincenty formula (5.4).

coordinates of observations to IRFs are shown in figure 5.5. From all possible IRFs only a few are selected for the observations.

In general, having test data on the declination lines would improve the analysis tremendously, as not only the training data and thus the models, but also the IRFs, and thus the description of the detector, would best fit to the observations. A future MC-production for LST-1 might incorporate this opportunity of improvement.

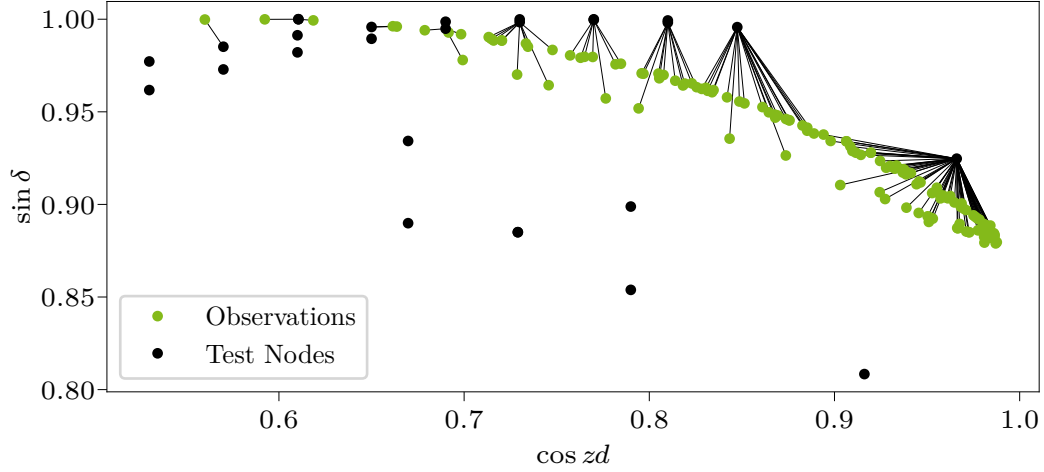


Figure 5.5: Associations of nearest test-data node for some observations. The green points are the pointings of the observations, black points are the test nodes of the All-Sky MC, and the lines represent the association. The nearest node is calculated as the minimal euclidean distance between test node and observation pointing, using the cosine of the zenith distance and the angular separation of the pointing to the field lines of the Earth's magnetic field.

Although there are many test nodes available, the observations lie in such a declination line that only a few nodes are selected. Observations with the same test node associated will be analyzed with identical IRFs.

5.3 Calculating Instrument Response Functions

The IRFs produced by LST On-Site Analysis (LST OSA) have singular default cuts for gamma-hadron separation, *gammaness*, and for the size of the source region θ_{\max} . Better results can be achieved by having those cuts energy-dependent, as typically the direction reconstruction is better for higher energies. Therefore, the IRFs are recreated with energy-dependent *gammaness* and θ_{\max} cuts for each test node. Figure 5.6, figure 5.8, and figure 5.9 show the IRFs created this way for the test nodes associated with the lowest and highest zenith distance of the selected observations. The effective area is calculated in true energy, whereas the

gammaness and θ_{\max} cuts are calculated in reconstructed energy. The command line tool `lstchain_create_irf_files`, with the configuration shown in [appendix 2.1](#), creates the **IRFs** on simulated gammas. `lstchain` internally uses `pyirf` to calculate the **IRFs**.

Background

No background **IRF** is created, as this is a point-source analysis with data taken in wobble-mode. The background counts are estimated from the observations. In a different case, a background model would need to be created from **MC**-protons and **MC**-electrons with the same cuts as described below. For this analysis, the background estimation is explained in [section 4.4](#), and the results are shown in [section 5.5](#).

Point Spread Function and Field of View Offset Bins

The **PSF** can, in general, be highly dimensional (see [section 4.4](#)), but for LST-1 it is parameterized with radial symmetry. For this point-like analysis of a known source position, with observations taken in wobble-mode, a single **FoV** offset bin is used, which centers at the wobble distance. In this case, it is a bin from 0.3° to 0.5° . In this bin, the **PSF** is assumed to be constant. The size of the source region in this bin is still energy-dependent, and its calculation is described below.

Effective Area

The effective area is calculated as

$$A_{\text{eff},i} = \frac{n_{\text{reconstructed},i}}{n_{\text{simulated},i}} \cdot A_{\text{simulated},i} \quad (5.11)$$

for each energy bin $i \in \{E_{\text{true}}\}$. [Figure 5.6](#) shows the energy-dependent effective area binned in true energy. Low-zenith distance observations have a much larger effective area in the low-energy region than high-zenith distance observations, which in turn have a larger effective area in the high-energy region. In high-zenith distance observations, the **EAS** have to travel through much more air mass compared to low-zenith observations. Therefore, the Cherenkov photons created in lower primary energy **EASs** do not reach the ground in sufficient numbers. On the other hand, in low-zenith observations, the highest energies create huge **EASs**, which saturate the camera entirely. Both effects reduce the effective area.

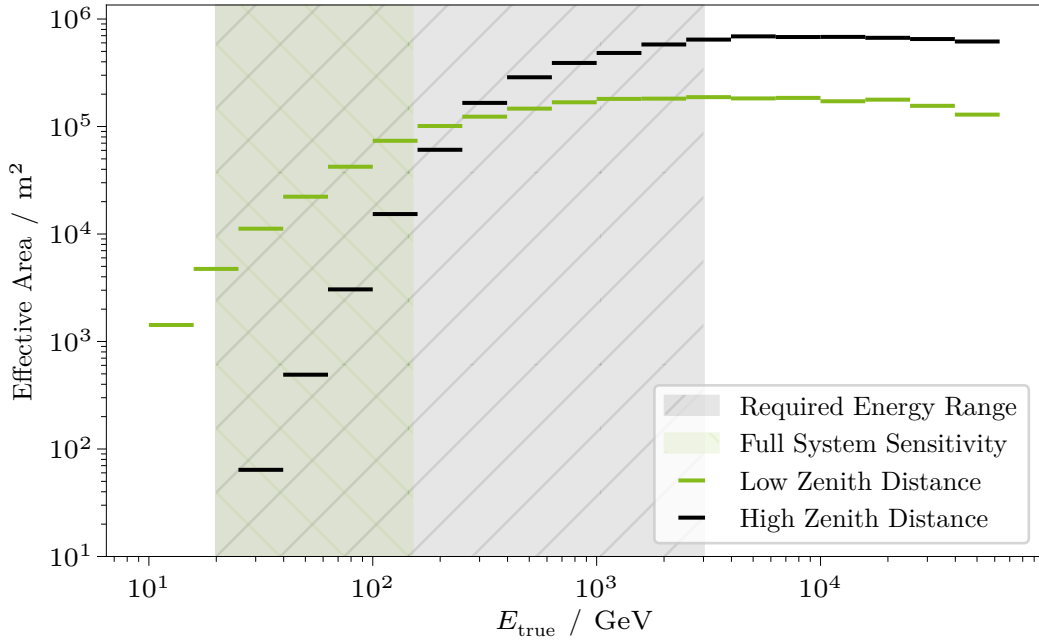


Figure 5.6: Energy-dependent effective area A_{eff} . The low-zenith distance observation has a larger A_{eff} in the lower energies and a smaller A_{eff} in the higher energies compared to the high-zenith observation. In addition to the effective area, this plot shows the *required energy range*, that is the range in which the LSTs are required to operate, and the *full system sensitivity*, that is the energy range in which the LSTs have the most impact for the array-sensitivity of CTA, compared to the other telescope types.

Energy Dispersion

The energy dispersion is calculated by histogramming the true energy, versus the relative estimated energy $\mu = E_{\text{reco}}/E_{\text{true}}$, and the FoV offset bins and normalizing both histograms. Just one FoV offset bin is used here because this is a point-like analysis of a known source position at a fixed wobble offset. Consult [section 4.4](#) for more information. [Figure 5.7](#) shows the energy dispersion for observations with low and high zenith distances.

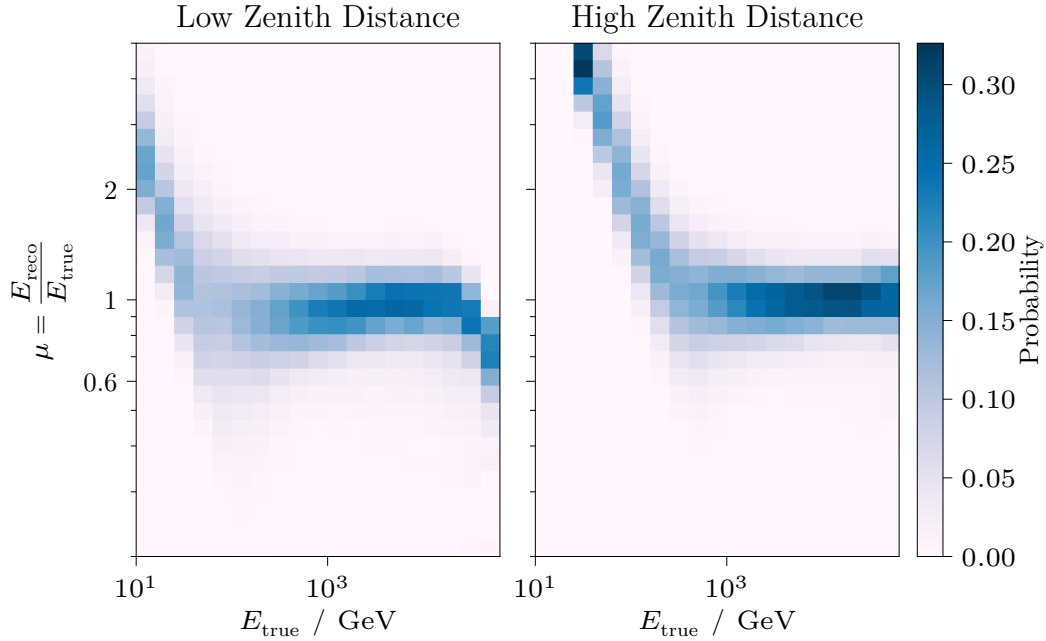


Figure 5.7: The energy dispersion matrix (also shown in figure 4.7). The low-zenith distance observation (left) has better properties for lower energies and worse for higher energies, compared to the high zenith distance observation (right).

Gammaness Cut

The gammaness cut is made at $p_\gamma = 70\%$ efficiency, and is calculated as the $1 - p_\gamma$ percentile of the events per reconstructed energy bin. A necessary requirement for the efficiency cut is at least 100 events per bin, otherwise a constant fill value is used. The fill value is set by `lstchain` to the maximum gammaness of all events, so basically to 1, discarding all events in low statistic bins. In addition a maximal and minimal viable cut are set to $g_{\min} = 0.4$ and $g_{\max} = 1.0$. In the used version of `pyirf` (version 0.6.0, [82]) the viable cut range is applied *after* the fill value is set, so that in effect the fill value is the maximal viable cut as configured. This is unexpected and might introduce effects that are not investigated. In the most recent version of `pyirf` (version 0.8.1, [71]) this changes. At the time of writing, the development branch of `lstchain` still uses `pyirf` 0.6.0.

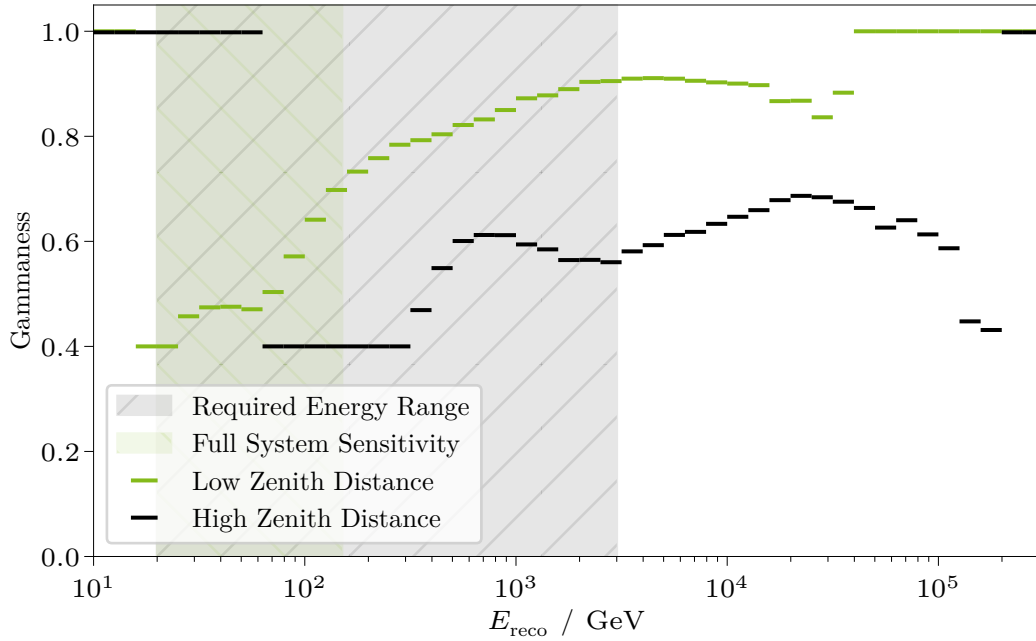


Figure 5.8: Energy-dependent gammaness cut. Higher cuts are tighter. Energy-dependent IRFs for the test node associated with the runs with highest and lowest zenith distance, compare figure 5.5. The low-zenith distance observation has tighter cuts.

The highlighted energy ranges for CTA/LST are defined in true energy, but the plot axis shows reconstructed energy, neglecting the energy dispersion. Still, they are displayed to show the performance of LST-1 in those regions, and that LST-1 can observe much higher energies than required.

Figure 5.8 shows the gammaness cuts in dependency of the reconstructed energy. In the whole energy regime, the low-zenith observation has tighter cuts than the high-zenith observations. This means the model estimates the gammaness of simulated gammas in low-zenith observations closer to one for low-zenith observations. There are two possible explanations. First, it is more difficult for the model to separate gammas and protons for high-zenith observations. Second, the model generally estimates lower gammaness values for high-zenith observations, even for protons. The latter case has no implications for the separation performance, whereas the former needs an improved model. This needs to be investigated.

Theta Cut

The θ_{\max} cut is the radius of a region containing $p_{\theta} = 68\%$ of the gamma-like events. This time, the constant fill value for low-statistic bins can be configured. In this analysis it is set to 0.35° for bins with less than 100 events, so that the wobble regions do not overlap. Figure 5.9 shows the θ_{\max} cut.

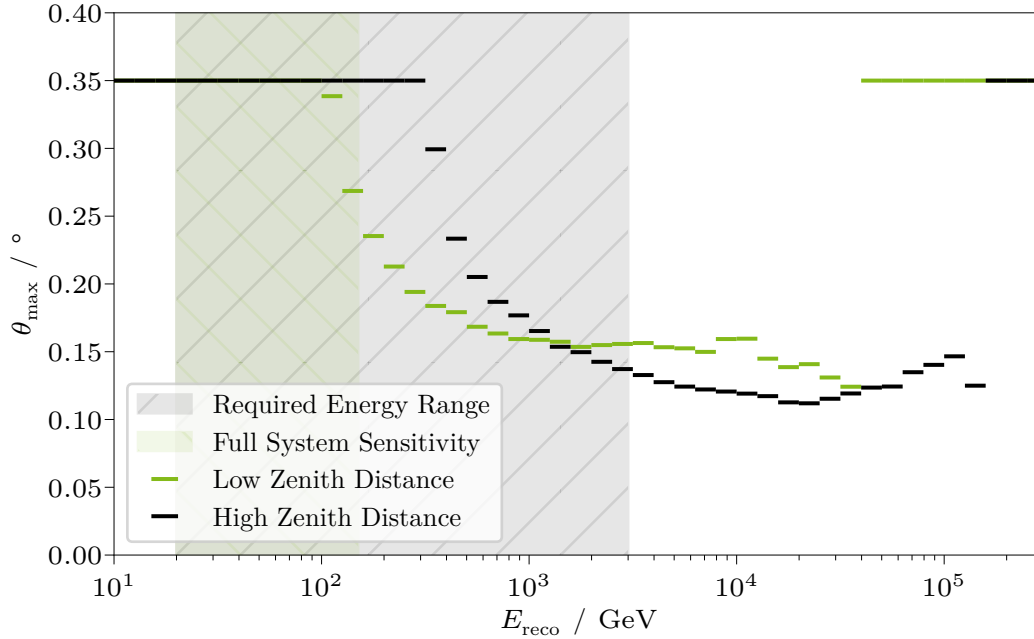


Figure 5.9: Energy-dependent θ_{\max} cut, lower cuts are tighter. Higher energies have tighter cuts, showing that the direction reconstruction is better at higher energies. Even more so for high-zenith observations, due to even more elongated shower images. θ_{\max} is the radius of the on- and off-regions used for the signal and background estimation as explained in figure 4.10. The highlighted regions are for true energies, but displayed on a reconstructed energy axis.

5.4 Application of Models

Processing to DL2 is straightforward after selecting the declination line corresponding to the source's path. The command line tool `lstchain_dl1_to_dl2` applies the

trained models to observations. By providing the observation data, the model from the selected declination line, and the configuration file of the model's training, a DL2 file is created. At this stage, it is possible to select events that fulfill certain quality criteria. This was not done for training the models, except for discarding events where image parameterization failed, and thus is not done up to this point for analysis of the observed data. Selecting quality events for the training of the models would certainly result in better models and is a possible improvement for future analyses. The configuration file for `lstchain_d11_to_d12` is shown in [appendix 2.2](#). This step applies the trained models to the observed data. Afterward, the data has four new features: estimated energy E_{reco} , estimated arrival direction, and the estimation of the particle type: `gammaness`. [Figure 5.10](#) shows the reconstructed source position of all observed events, including gammas and non-gamma events.

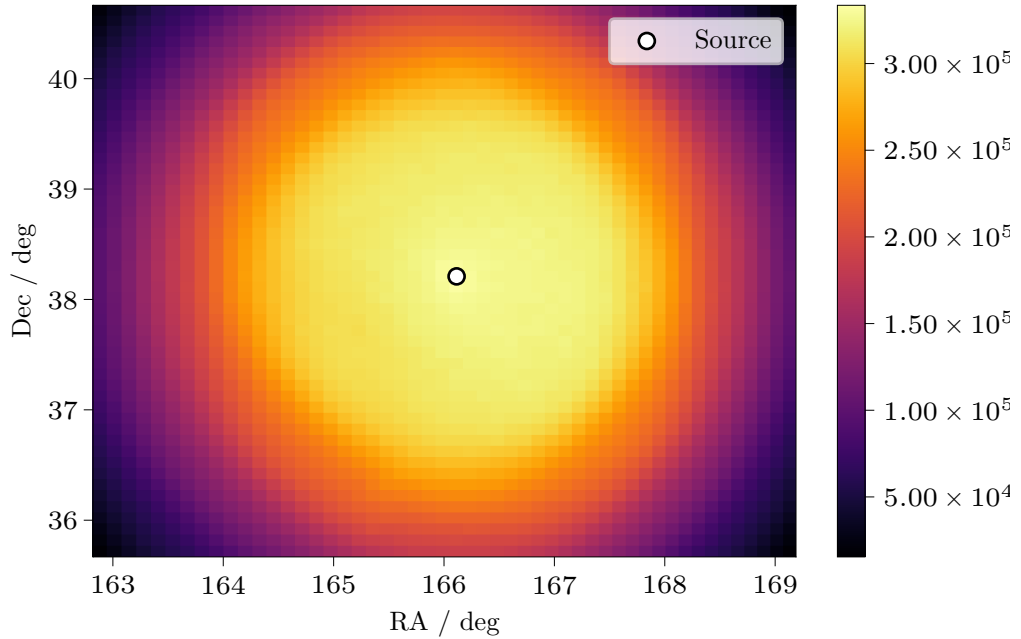


Figure 5.10: Skymap of all DL2 events. The position of Mrk 421 is marked at the center. Most data in this plot are non-gamma events, that need to be discarded for the further analysis. It is done by the applying the `gammaness` cut, as explained in [section 5.3](#) and [figure 5.8](#).

5.5 List of Gamma-like Events

In the DL2→DL3 step, the aforementioned gammaness and θ_{\max} cuts are applied. A DL3 file is created that has a standardized format [44] and can be read by the high-level science analysis tool `Gammapy`. The current DL3 format is expected to be extended and refined by the CTA Consortium. In addition to the list of gamma-like events, the respective IRFs are appended to the DL3 files for each observation.

Background Estimation

The selected gamma-like events are shown in figure 5.11. A clear peak is visible in

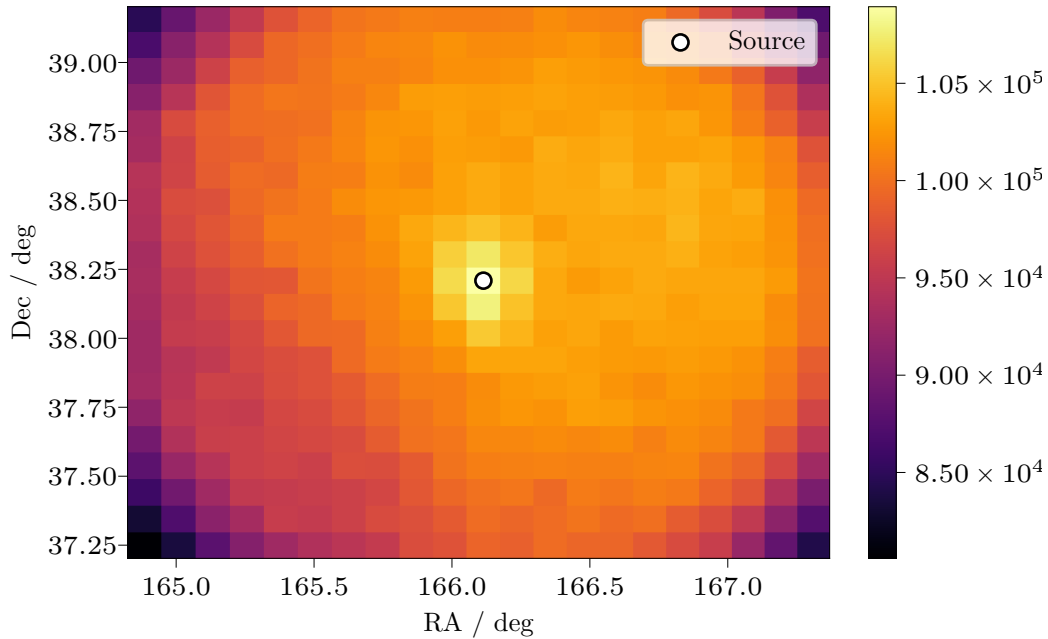


Figure 5.11: Skymap of all DL3 gamma-like events that are observed from the direction of Mrk 421. A clear peak is visible at the center. The off-positions are not marked here, as the off-counts come from off-positions in camera coordinates. Nonetheless, at distances of about 0.8° to the source, less events are reconstructed than in the center.

the center, where the source is marked with a white dot. The angular resolution, described by the PSF, is clearly visible due to the dispersion of the events from

the point source. In addition, the large counts throughout the FoV originate from misclassified hadrons.

The on- and off-counts of these observations yield a significance via equation (4.27) of

$$S_{\text{LiMa}} = 37.63 \sigma. \quad (5.12)$$

The squared angular distances θ^2 of the on- and off-counts to the source position are shown in figure 5.12. Shown are three histograms: the whole energy range, a low-energy bin, and a high-energy bin.

Event Spectrum

The rate of all reconstructed events are shown in figure 5.13. Three histograms are shown: all triggered events, the events classified as gammas, and the gamma-like events in the on-region. The lines represent power laws after an initial threshold, where the spectrum after the gammaness cut (green) is steeper than the spectrum before (black).

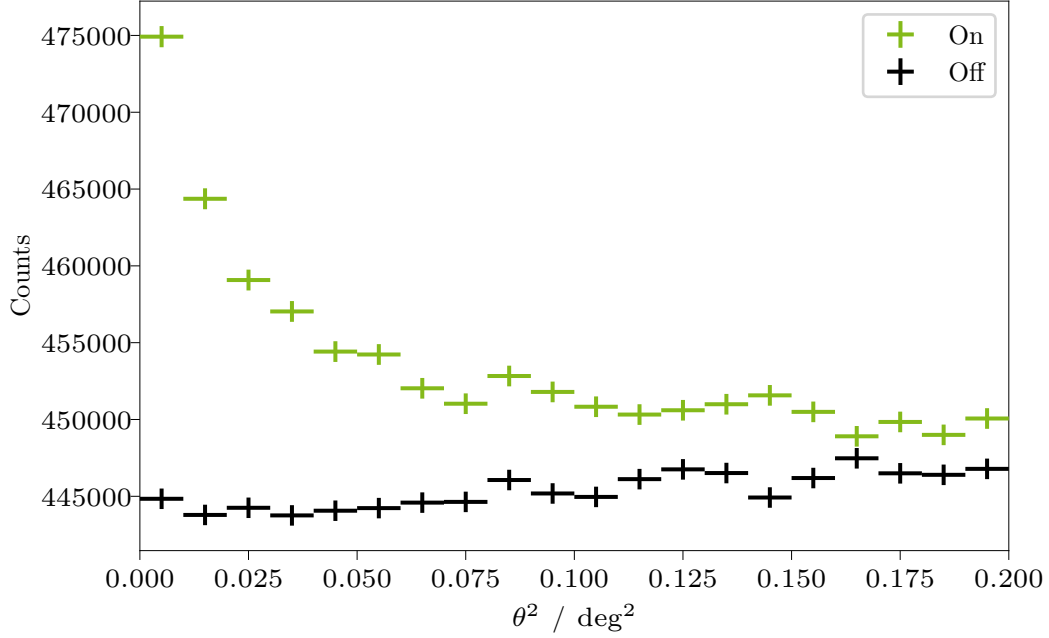
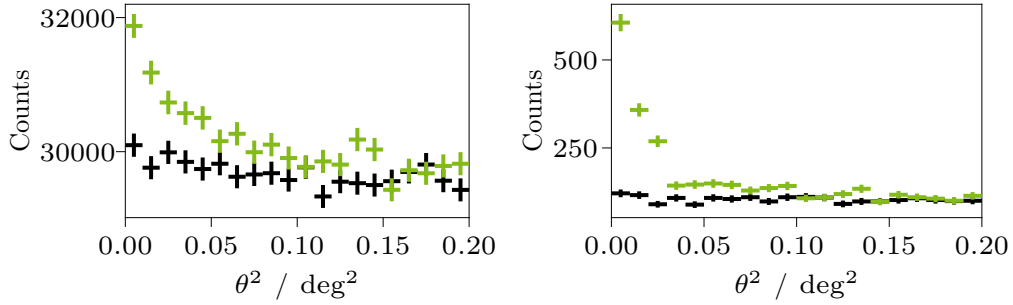

 (a) θ^2 plot of the whole energy regime.

 (b) θ^2 plot in a low-energy range from 100 GeV to 125 GeV. (c) θ^2 plot in a high-energy range from 1.0 TeV to 1.3 TeV.

Figure 5.12: θ^2 plot, distribution of the squared angular distance of the on-counts (green) and off-counts (black) to the center of the on-region. The peak of the on-counts is clearly visible. This observation has a significance of $S_{\text{LiMa}} = 37.63 \sigma$.

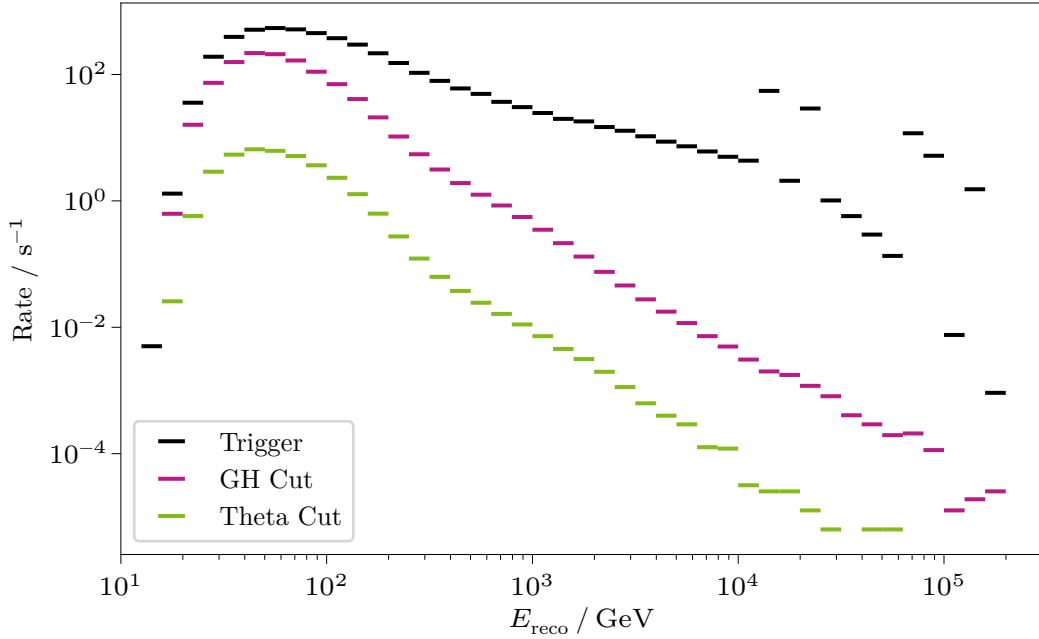


Figure 5.13: Event rate of this analysis. The rates are shown for all triggered events (black), the selected gamma candidates after the gammaness cut (pink), and the selected on-events after the θ_{\max} cut (green).

5.6 High-Level Analysis

The data is now reduced to one [Data Level 4 \(DL4\)](#) dataset for the whole observation period by binning the gamma-like events into histograms of reconstructed energies $N(E_{\text{reco}})$, possibly interpolating the exposure, background, PSF and energy dispersion. These reduced datasets are used in the following high-level analysis.

Flux Fitting

Gammapy can forward fold spectral flux models $\Phi(E)$ with the IRFs R

$$\hat{N}(E_{\text{reco}}) = t_{\text{eff}} \int_{E_{\text{true}}} dE_{\text{true}} R \times \Phi(E_{\text{true}}), \quad (5.13)$$

to compare the result with the reconstructed event spectrum $N(E_{\text{reco}})$. The proposed flux model is a log-parabola

$$\Phi(E \mid \alpha, \beta, E_{\text{ref.}}) = \Phi_0 \frac{E^{-\alpha - \beta \log\left(\frac{E}{E_{\text{ref.}}}\right)}}{E_{\text{ref.}}} \quad (5.14)$$

and is fitted as shown in figure 5.14. The results of the fit are

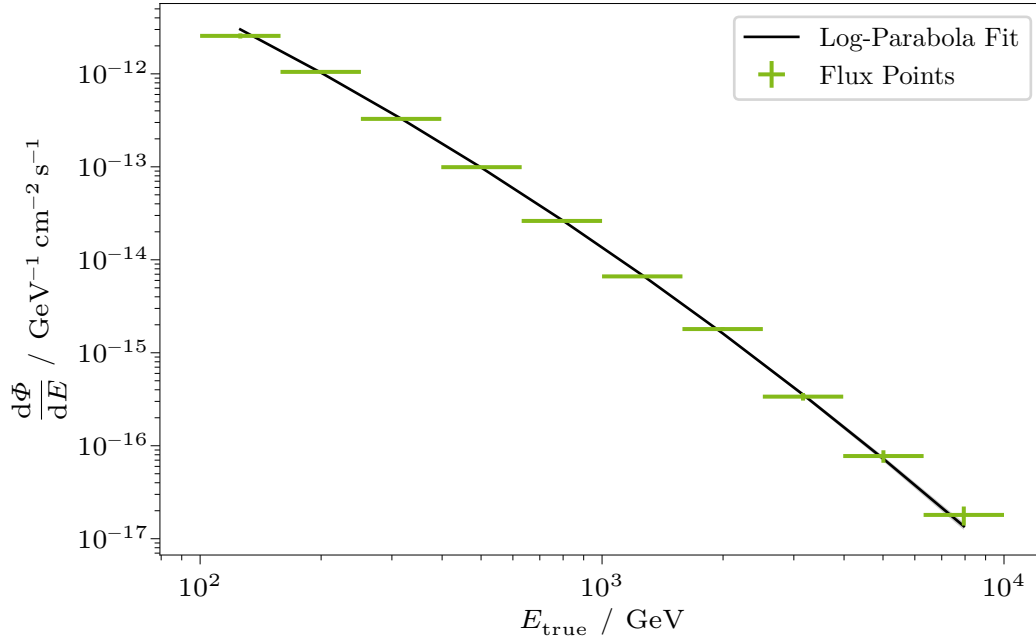


Figure 5.14: Forward folded log-parabola (5.14) spectral model. Fitted parameters in (5.15) to (5.18). The green flux points are calculated from the fitted model in the respective bins.

$$E_{\text{ref.}} = 1 \text{ TeV} \quad (\text{fixed}) \quad (5.15)$$

$$\Phi_0 = (1.369 \pm 0.021) \times 10^{-11} \text{ cm}^{-2} \text{ TeV}^{-1} \text{ s}^{-1} \quad (5.16)$$

$$\alpha = (2.968 \pm 0.023) \quad (5.17)$$

$$\beta = (1.770 \pm 0.093) \times 10^{-1}. \quad (5.18)$$

Light Curve

The light curve is the differential flux integrated and binned into time bins. Figure 5.15 shows the integrated flux from 10^2 GeV to 10^4 GeV in a run-wise binning.

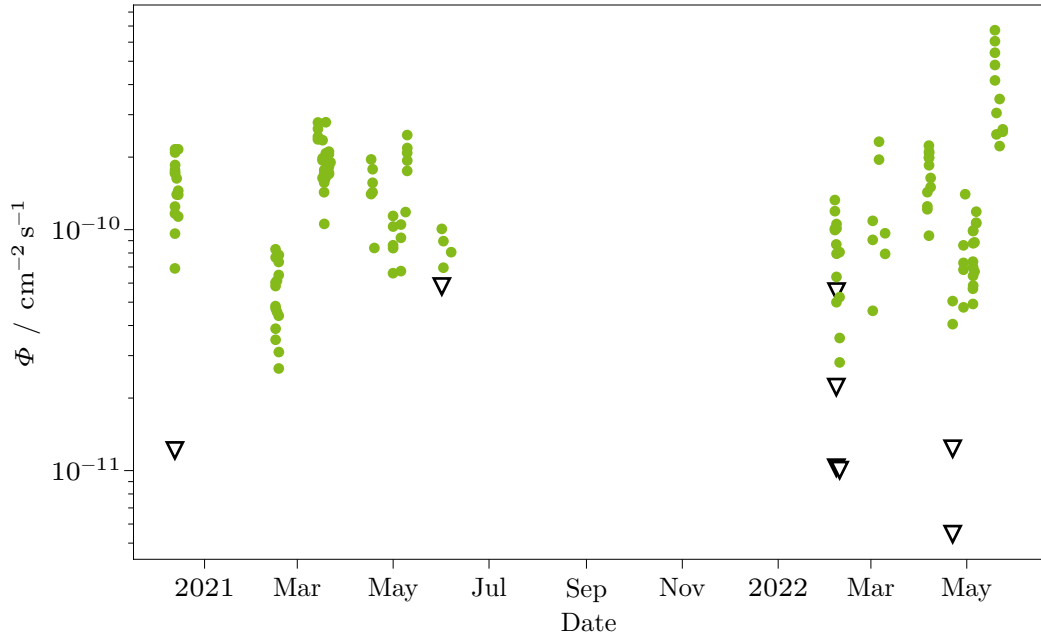


Figure 5.15: Light Curve showing the integrated flux from 10^2 GeV to 10^4 GeV for the whole observation with a run-wise binning. From July 2021 to February 2022 no data was taken, as Mrk 421 was below the horizon. Upper limits are marked with a downward facing triangle.

In the light curve no sudden changes of the flux indicate a flare in the observed period.

6 Unfolding

Easy is the path to wisdom for those
not blinded by ego.

Star Wars: The Clone Wars
S01E03 *Shadow of Malevolence*

Calculating the astrophysical flux from the event counts of an observation with an instrument that has a nonzero energy dispersion is an inverse problem. Inverse problems are generally ill-posed and ill-conditioned.

Instead of measuring the distribution $f(x)$ of the sought physical quantity x , the distribution $g(y)$ of the observed quantities y is measured. In addition, an irreducible background $b(y)$ is measured. The problem is described by the Fredholm equation of the first kind,

$$g(y) = \int A(x, y) f(x) dx + b(y), \quad (6.1)$$

where $A(x, y)$ is the folding kernel, which gives probabilities of measuring the value y instead of the true value x . Reconstructing the true distribution $f(x)$ from the measured distribution $g(y)$ is called *unfolding*. In contrast to forward folding or fitting, and bin-by-bin acceptance corrections, unfolding is model-independent and considers all simulated measurement processes and detector and analysis effects. [Figure 6.1](#) gives a schematic overview of the processes.

In general, $A(x, y)$ is calculated via MC and binned according to the histograms of the measured distribution $g(y)$ and the true distribution $f(x)$. The Fredholm equation is accordingly described via discrete matrices and vectors

$$\vec{g} = \mathbf{A}\vec{f} + \vec{b}. \quad (6.2)$$

The folding kernel \mathbf{A} is a description of the detector response, summarizing all known detector and analysis effects.

The problem being ill-posed and ill-conditioned means that information gets lost during the translation of \vec{f} into \vec{g} via \mathbf{A} . This can be shown by solving the Fredholm equation using the (pseudo-) inverse

$$\vec{f} = \mathbf{A}^{-1} (\vec{g} - \vec{b}). \quad (6.3)$$

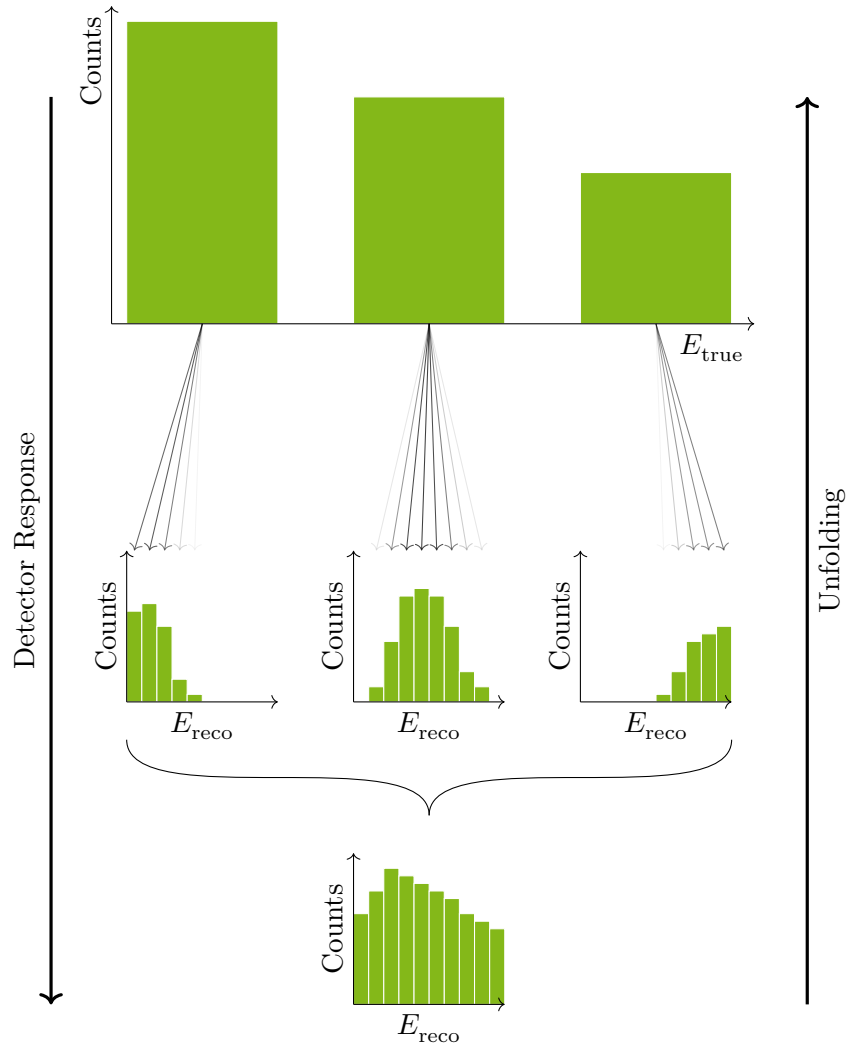


Figure 6.1: Schematic representation of the measurement process and unfolding of the energy spectrum of a gamma-ray observation. Figure idea adapted from T. Hoinka. The true energy (top) follows a power law, and in the lowest and highest energies, the reconstruction is limited by the effective area and smeared by the energy dispersion (center). The count-spectrum (bottom) resembles a typical one, compare figure 5.13.

This leads to oscillating and thus unphysical results in \vec{f} , as is shown in figure 6.2. To deal with this problem, *regularization methods* need to be employed. Regularization reduces the oscillations of the unfolded spectrum but increases the correlation between neighboring bins. In the simple case of inversion (6.3), small eigenvalues of the inverse can be discarded. This is shown on a toy distribution in figure 6.2. A detailed description can be found in appendix 3.

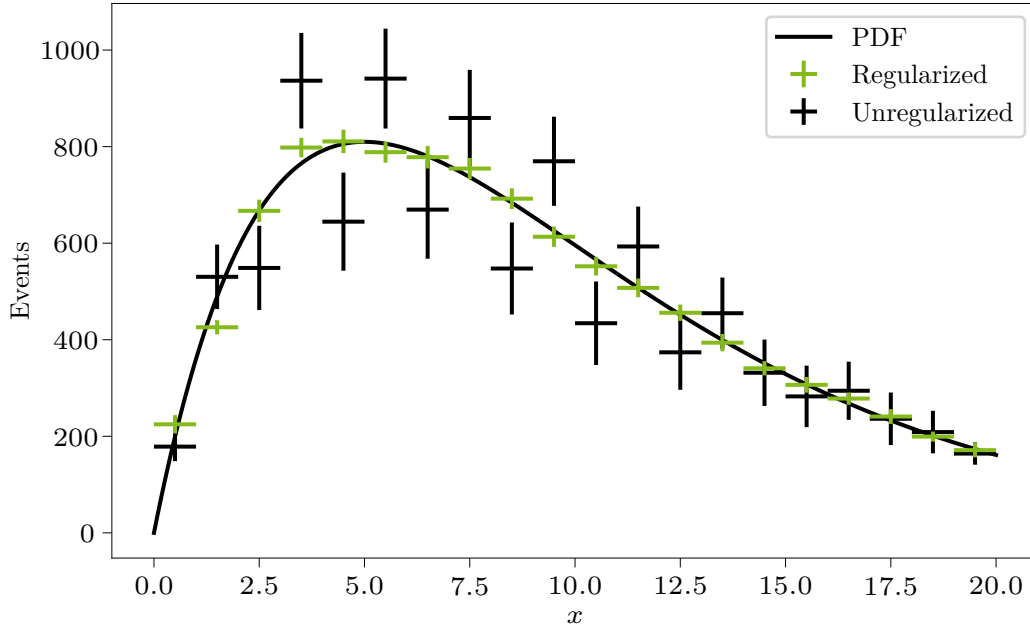


Figure 6.2: Unfolding with the inverse \mathbf{A}^{-1} and regularization via cutting off half of the eigenvalues. A detailed description can be found in appendix 3.

Using the inverse response matrix \mathbf{A}^{-1} is not the only way to solve inverse problems. An overview of unfolding methods for astroparticle physics is found in [33]. There are iterative methods, for example, *Iterative Bayesian Unfolding (IBU)*, where the unfolded result in each iteration is a Bayesian prior for the next iteration. The regularization strength is handled via the number of iterations. There are machine learning methods, one of them being the *Dortmund Spectrum Estimation Algorithm (D-SEA)*, developed by Ruhe et al. [91], where a machine learning classifier learns the bin number of each event [34].

6.1 Likelihood Unfolding

The most common unfolding algorithm in gamma-ray astronomy is likelihood unfolding, tightly coupled to the method of maximum likelihood estimation. In a maximum likelihood analysis, the likelihood of an observation given parameters

$$L = \prod_i f(x_i | \Theta) \quad (6.4)$$

is maximized:

$$\frac{\partial L}{\partial \Theta_k} = 0 \quad \text{for all } k. \quad (6.5)$$

That leads to an estimate for model parameters Θ . In the maximum likelihood method, usually the negative logarithmic likelihood

$$l = -\log L = -\sum_i f(x_i | \Theta), \quad (6.6)$$

is used. The logarithm is monotonic, meaning the location of the maximum does not shift. The negative is used because a huge number of numeric algorithms exist for minimization. The likelihood unfolding shown here is called **Regularized Unfolding (RUN)**, from Blobel [30]. It is made up of the Poissonian likelihood

$$p(k; \lambda) = \frac{e^{-\lambda} \lambda^k}{k!} \quad (6.7)$$

of the observed counts $k = g_i$ and the predicted counts from equation (6.2) $\lambda = \mathbf{A}_i f_i$ per energy bin i . Note that

$$b = 0, \quad (6.8)$$

as the background is assumed to be known and estimated from the wobble background and subtracted, as in section 4.4. The negative logarithmic likelihood is consequently

$$l = \sum_{i=0}^n \left\{ \sum_j (\mathbf{A}_{ij} \hat{f}_j) - g_i \log \left[\sum_j (\mathbf{A}_{ij} \hat{f}_j) \right] \right\}, \quad (6.9)$$

or

$$l = \mathbf{A} \hat{f} - g \log(\mathbf{A} \hat{f}), \quad (6.10)$$

with \hat{f} being the estimated flux.

Regularization

The regularization term used in **RUN** is the Tikhonov regularization [98]. In the Tikhonov regularization, the unfolded solution is assumed to be flat, having a vanishing second derivative. In astroparticle physics, this assumption holds for the acceptance-corrected flux in log-log space [31]. The second derivative is calculated via the method of finite elements, with

$$R_\tau(f) = \frac{\tau}{2} \sum_{i=2}^{n-1} (f_{i-1} - 2f_i + f_{i+1})^2 = \frac{\tau}{2} (\mathbf{C}f)^2, \quad (6.11)$$

where

$$\mathbf{C} = \begin{pmatrix} 1 & -2 & 1 & \cdots & 0 \\ \vdots & & \ddots & & \vdots \\ 0 & \cdots & 1 & -2 & 1 \end{pmatrix}, \quad (6.12)$$

a matrix of dimension $n \times (n-2)$ with n being the number of true bins.

The regularization strength in (6.11) is given by the parameter τ . With τ being zero, no regularization is applied, a larger τ means stronger regularization and $\tau \rightarrow \infty$ completely flattens the result. The best compromise between a flattened result and small bin-to-bin correlations is applied when the mean global correlation

$$\rho_{\text{global}} = \sum_{i=1}^n \sqrt{1 - ((V_f)_{ii}(V_f^{-1})_{ii})^{-1}}, \quad (6.13)$$

is minimized [11, p. 298], where V_f is the covariance of the unfolded bins at the minimum.

The regularization factor and mean global correlation are not calculated on all f_i , but both the first and last bins are excluded. These bins are called *underflow* and *overflow bins*. These bins can be included in the simulations, as they have a lower and upper bound. In observations, these bins are semi-unconstrained, as particles with lower or higher energy will probably be reconstructed in these outer bins.

Uncertainty Estimation

The statistical uncertainties are calculated from the inverse of the Hessian in the minimum

$$\sigma_i = (\mathbf{H}_f)_{ii}^{-1} |_{\text{min}}, \quad (6.14)$$

where

$$(\mathbf{H}_f)_{ij} = \frac{\partial^2 f}{\partial x_i \partial x_j}. \quad (6.15)$$

Implementation

With the implementation of `RUN` in `Gammapy`, it is possible to use the existing software, in particular, the `DL4` format and the handling of `IRFs`, to process the data and subsequently perform unfolding as an alternative to forward folding. The unfolding is implemented as a spectral model $M(E)$, where

$$M(E) = f_i \quad \forall E_i \leq E < E_{i+1} \quad (6.16)$$

is a histogram or step function, with the bin edges E_i and the unfolded flux or step height f_i . That way, the implementation can use the fitting and minimizing features provided by `Gammapy`. To prove the correctness of this implementation, a power law is unfolded. In this simulation, the response matrix \mathbf{A} is a Gaussian energy dispersion, f is a binned distribution following a power law, and g is created by folding a random sample following f with \mathbf{A} to obtain a realistic distribution g_{sim} of a characteristic observation. On this dataset, the optimal regularization strength τ is found as explained above. The minimal mean global correlation is shown in figure 6.3a. With this optimized τ , 200 realizations of g_{sim} are drawn and unfolded. In each unfolded bin, the true value of f , the median and central 1σ quantile (from $q_{0.16}$ to $q_{0.84}$) of \hat{f} is shown in figure 6.4a. In figure 6.4b the *pull statistic*

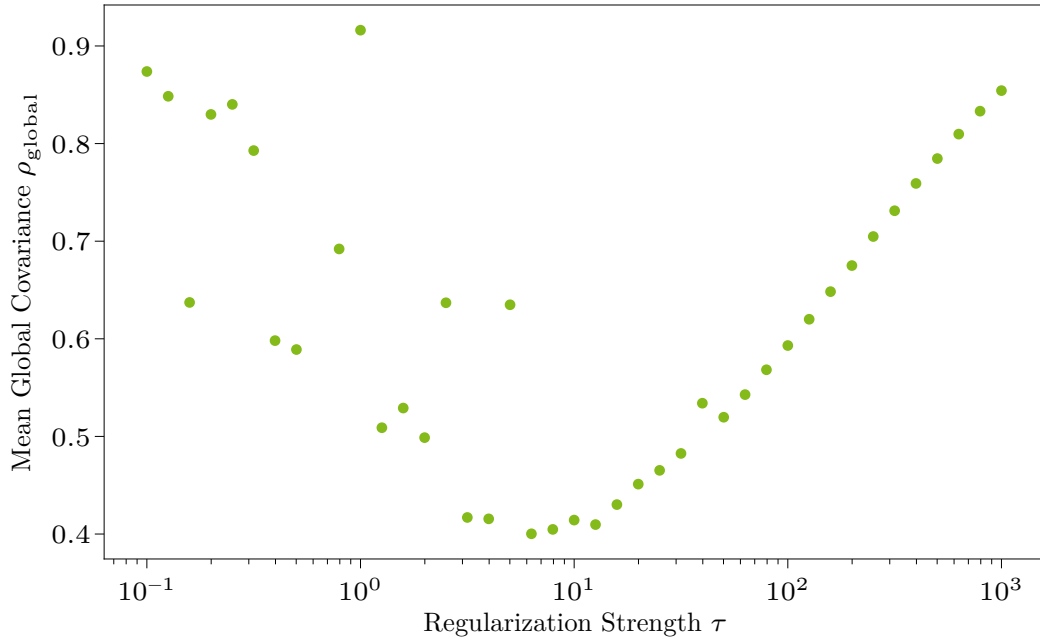
$$\text{Pull} = \frac{\frac{d\Phi}{dE}_{\text{est}} - \frac{d\Phi}{dE}_{\text{true}}}{\sigma_{\frac{d\Phi}{dE}}} \quad (6.17)$$

of the 200 simulations is shown per bin, as well as the median and central 1σ quantile.

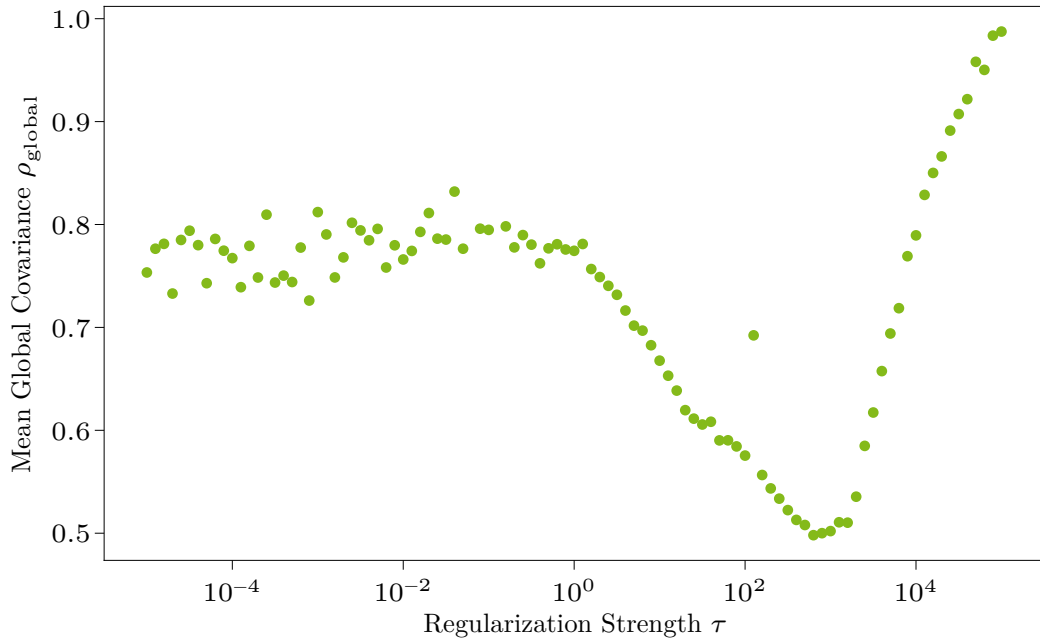
A great advantage of unfolding with `Gammapy` is the possibility to unfold many different observations k at once, using the same unfolded flux points f as the solution

$$l_{\text{total}} = R_\tau(f) + \sum_{k \in \text{Obs}} \mathbf{A}_k f - g_k \log(\mathbf{A}_k f), \quad (6.18)$$

where f is independent of k . In the `IRFs` (section 4.4) all known detector effects and analysis effects are encoded, thereby the folding kernel \mathbf{A}_k and thus the acceptance correction is taken care of per dataset k .

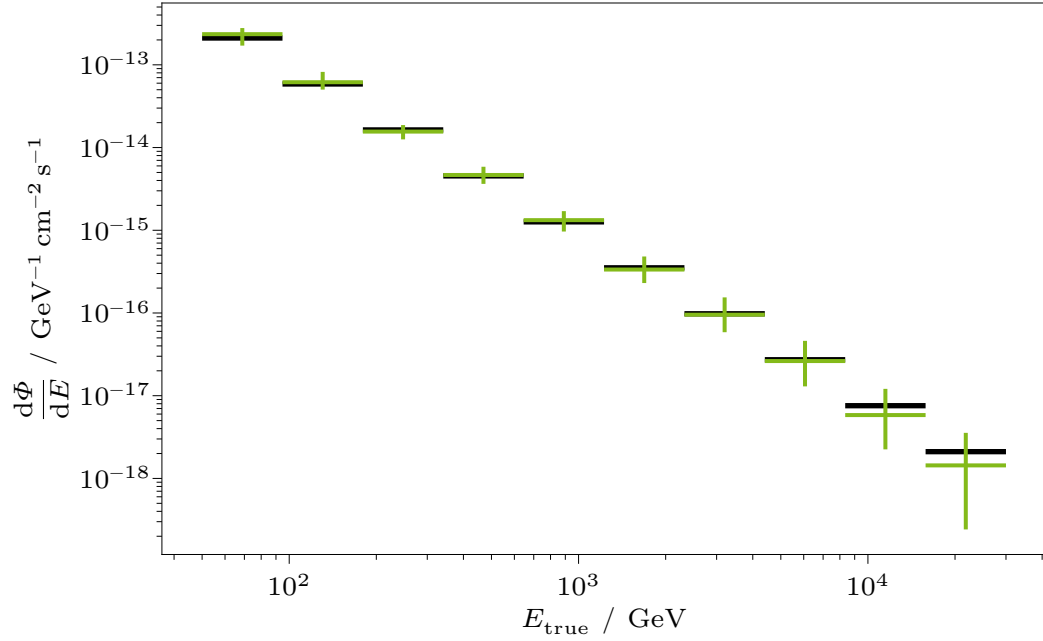


(a) The mean global correlation for the pull statistic. To the left of the minimum the unfolded result oscillates more, and to the right of it the regularization over-flattens the result.

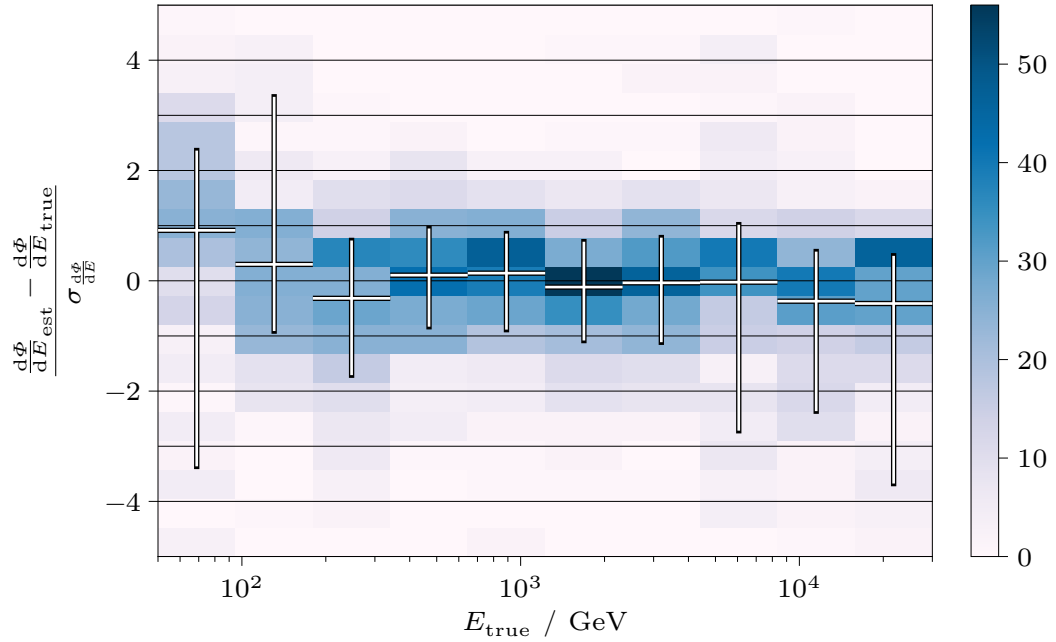


(b) The mean global correlation for the unfolding of the Mrk 421 flux in figure 6.6.

Figure 6.3: Optimization of the regularization strength τ using the mean global correlation ρ_{global} (6.13).



(a) A power law, simulated 200 times and unfolded with **Gammapy**. Displayed are the true spectrum (black), the median and central 1σ quantile (green, error bars). The regularization strength is optimized by means of ρ_{global} as shown in figure 6.3a.



(b) Pull statistic, the relative deviation of the true flux and the unfolded flux. Shown is each result \hat{f} in the 2d-histogram, as well as the median and the central 1σ quantile in each bin.

Figure 6.4: Pull statistic for the evaluation of the unfolding implementation.

Crab Nebula Crosscheck

Observations of the Crab Nebula during the same period as the Mrk 421 data are unfolded with this unfolding implementation. As explained in [chapter 2](#), the Crab Nebula is the standard candle in VHE gamma-ray astronomy and can be used as a calibration source and for a crosscheck of the analysis. The same steps are carried out as for the Mrk 421 analysis, as detailed in [chapter 5](#). For the All-Sky-MC from [section 5.2](#) and [figure 5.3](#), the declination line at 22.76° is used. [Figure 6.5](#) shows a fitted log-parabola spectrum, the unfolding, and the reference model from Meyer [75], as observed by the MAGIC telescopes. The unfolded flux points are larger than the forward folded ones for the whole energy range. In the high-energy bins, the differences lie well inside the errors of both models. In the low-energy bins, the unfolded flux points match the reference spectrum even better than the forward folded spectrum. The optimal regularization strength and the correlation matrix

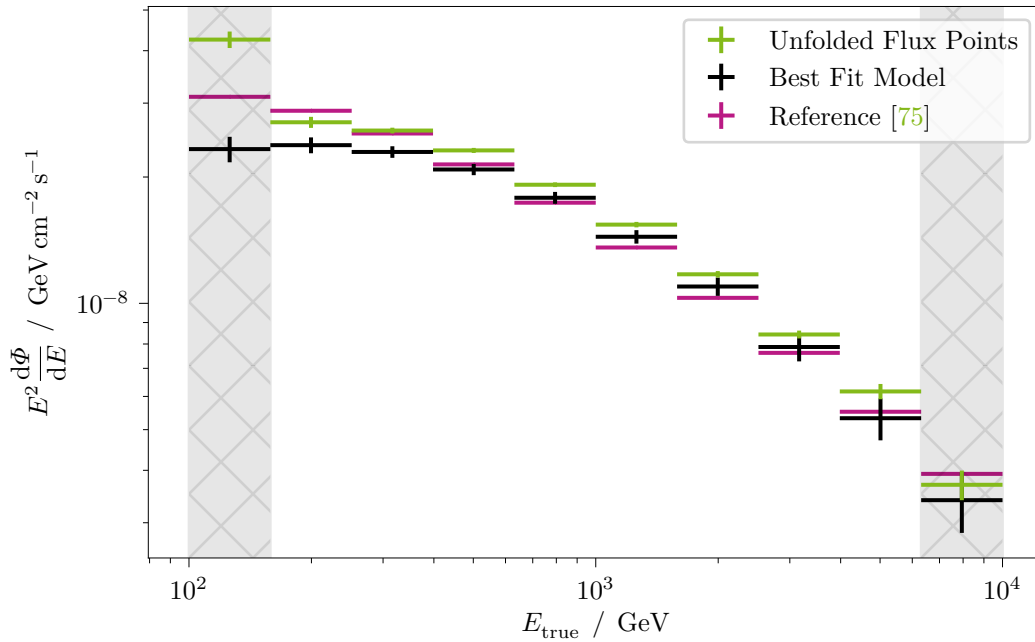


Figure 6.5: Observations of the Crab Nebula with a fitted log-parabola, the unfolded flux points from this analysis, and the reference model from Meyer [75].

can be found in [appendix 4](#).

6.2 Unfolding of LST-1 Data

The aforementioned implementation in `Gammapy` is used to unfold observations of the blazar Mrk 421 by LST-1. The data used in unfolding is the same as selected through [chapter 5](#) and was fitted in [figure 5.14](#).

In total, 146 runs are selected for the analysis. These 146 observations have such a pointing that only 9 IRFs from the All-Sky MC are used, compare [figure 5.5](#). This makes it possible to *stack* those observations with identical IRFs. The act of stacking is carried out by adding the histograms of observed counts from the measurement and exposures

$$g = \sum_k g_k \quad (6.19)$$

$$e = \sum_k e_k = \sum_k A_{\text{eff}_k} t_{\text{eff}_k}. \quad (6.20)$$

The effective area

$$A_{\text{eff}_k} = A_{\text{eff}} \quad \forall k \quad (6.21)$$

is the same, but the effective time t_{eff_k} differs between observations k . The stacking reduces the computational load by more than an order of magnitude.

The optimal regularization strength τ is found as the point with minimal mean global correlation and shown in [figure 6.3b](#).

Finally, [figure 6.6](#) shows the unfolded flux of Mrk 421, as observed by LST-1 in 146 runs for 41.65 h during one and a half years. Compared to the forward folded flux from [figure 5.14](#) and (5.15) to (5.18), the unfolded flux points are larger than the fit for the whole energy range. In the high-energy bins, the difference is covered by the statistical errors, but not so in the low-energy bins. On the other hand, the first two unfolded flux points hint at a feature that is not fitted due to the model constraints of the forward folding. [Figure 6.7](#) shows the correlation matrix of the unfolded bins. Low bin indices correspond to lower energies, the overflow and underflow bins are not shown. The correlation is negative for lower energy bins and positive for higher energy bins. In [figure 6.8](#), the unfolded flux points are shown together with the lower-energy flux points for a complete overview of Mrk 421. This work extends the measured range of the multi-wavelength spectrum of Mrk 421 to the highest energies.

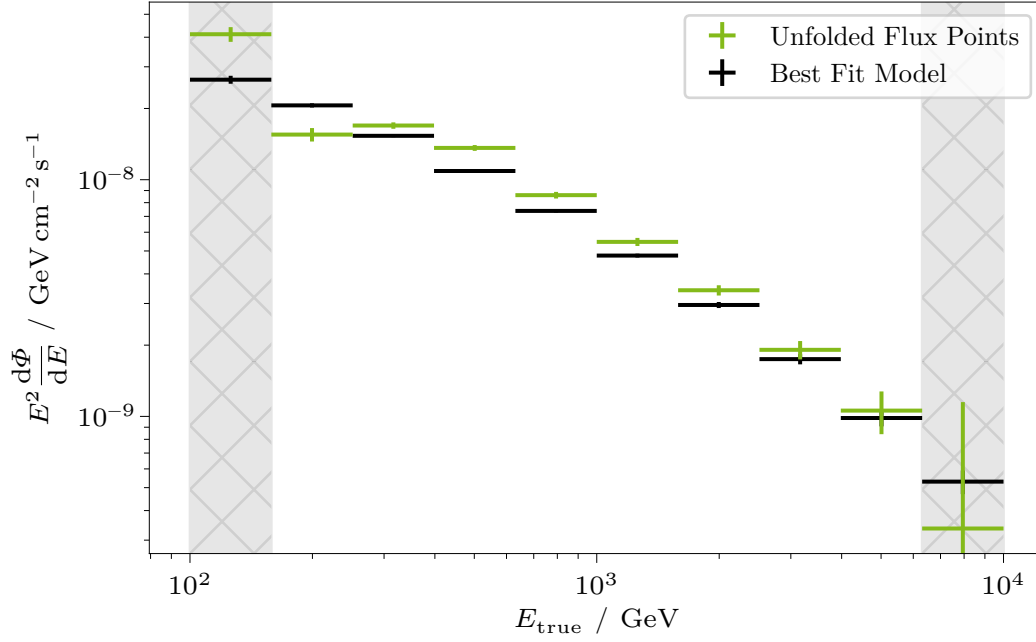


Figure 6.6: Unfolded flux of Mrk 421 with the LST-1 datasets produced as described in [chapter 5](#) and stacked as described in the main text of this chapter. The optimal regularization strength τ is found as described in the main text and shown in [figure 6.3b](#). The shaded areas denote the underflow and overflow bins.

In addition, the fitted log-parabola from [figure 5.14](#) is shown in a binned manner. The unfolded result is larger than the fit over the whole energy range, except for the first flux points, which hints at a feature missed by the forward folding.

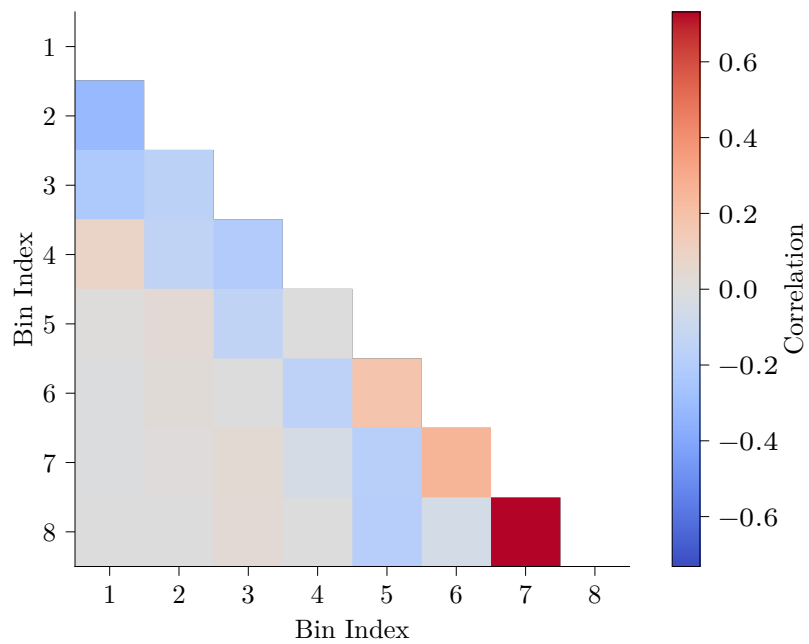


Figure 6.7: Correlation matrix of the unfolding shown in figure 6.6. The underflow and overflow bins are not displayed. The self-correlation of each bin is also not displayed to have a more extensive visual range in the color bar. The correlation is visible for two to three neighboring bins, with negative correlations in the lower bins (lower energies) and vice versa for the higher bins.

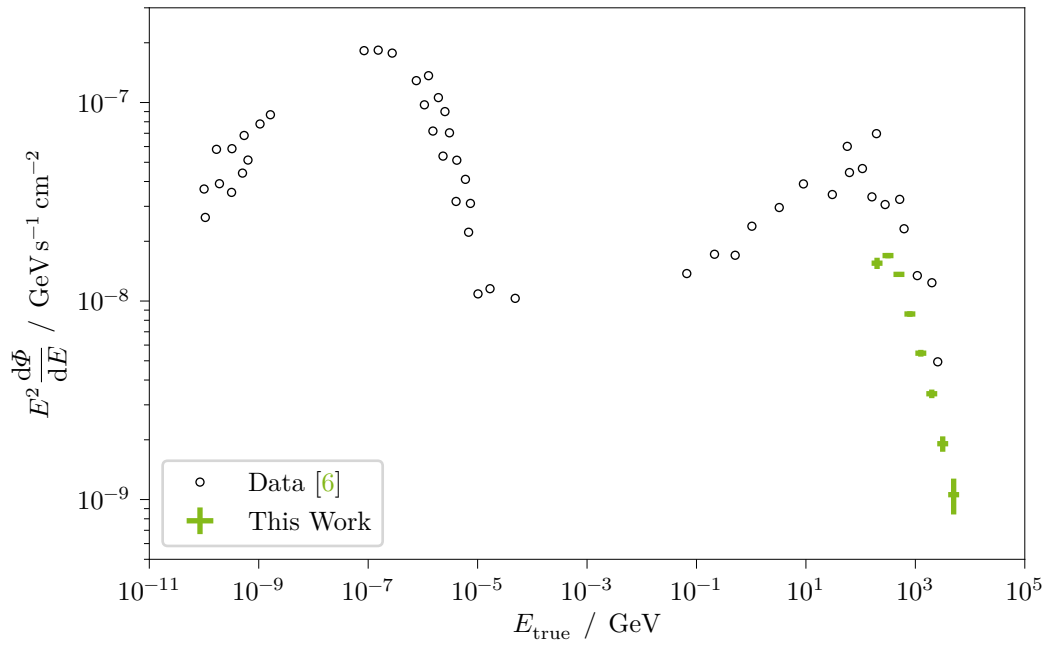


Figure 6.8: Unfolded flux points of this work (green) together with the SSC model and data points from [6] that was shown earlier in figure 2.5. This work extends the measured range of the multi-wavelength spectrum of Mrk 421 to the highest energies.

7 Conclusions and Outlook

Stick a fork in me, I'm done.

Chandler Bing
Friends S02E13 *The One After the Super Bowl* (2)

In this work, I have presented a new analysis chain for the analysis of data from the LST-1. With this, I analyzed data of the blazar Mrk 421. Furthermore, I have developed a prototype for unfolding in the open-source high-level gamma-ray analysis software **Gammapy**, and demonstrated its functionality. LST-1 is an excellent experiment for **VHE** gamma-ray astronomy, especially in the GeV–TeV regime. LST-1 is thus a pioneer for the **CTA**, of which it is the first prototype at its final location. Three more **LSTs** are planned in the north, which are already under construction⁷. The inauguration of the other three **LSTs** will complete the low-energy detector of **CTA** and bring out the maximum sensitivity of telescopes in this energy range.

The analysis chain enables fully automated analyses of point-like sources after a few configuration steps. It will be used to analyze various **AGN** in the **LST AGN Zoo** paper (in preparation). Further developments of the analysis chain are very user-friendly, as it is based on the workflow manager **snakemake** [76]. As I write this thesis, we are working on an automatic Bayesian Blocks analysis, which divides the light curve into blocks of similar spectra.

The light curve I generated in this work shows that the source Mrk 421 was relatively constant over the observation period. The Bayesian Blocks analysis, which is currently being worked on, will quantify and could confirm this assumption. Additionally, it provides the opportunity to divide the data into subsets of different intensity states of Mrk 421 and then unfold the flux for shorter periods with similar flux levels instead of unfolding the whole period. This allows a closer look at the source, which has shown variability in gamma rays in the past, and further investigates possibly different spectra in the different periods.

The general analysis software for **LST** data, **lstchain**, is being worked on by a multinational team that I was part of. It works very well, as demonstrated in the

⁷Watch live construction: <https://lst1.iac.es/webcams.html>

LST-1 performance paper [41], but there is still potential for further improvements. Presently, the IRFs are still a weak point of the analysis chain. First, the newer and up-to-date version of `pyirf` [71] must be used, which is not the case even in the currently released version of `lstchain`. Using the old version leads to unexpected behavior, as explained in section 5.3. Currently, discrete points in the equatorial coordinate system must be selected for the analysis, hoping to sufficiently mirror the observed data. A working group is already working on the interpolation of the coordinates to provide more accurate IRFs for a given observation [46]. Here, the nearest three IRFs from the test nodes of the All-Sky MC are interpolated for each observation.

A further issue is the All-Sky MC. Training datasets are produced only for a limited amount of possible source tracks along their declination lines. The All-Sky MC does not cover all tracks that were observed in the past, such as that of Mrk 421. Also, the grid of test nodes does not cover the whole sky. The resulting problem is that for this analysis, the used model was not trained on simulations that match the observations, and the IRFs that were created from the grid test nodes also do not match the observations. It is assumed that both issues cancel out, but much better performance will be achieved by creating IRFs on those declination lines on which the model was trained in the first place. That would make the simulated training data and the detector description match the observation conditions perfectly.

The particle classifier needs a thorough examination for high-zenith conditions. As shown in figure 5.8, the gamma efficiency yields much smaller gammaness cuts for high-zenith observations than for low-zenith observations. Since no test datasets of proton simulations exist, it could not be ruled out here that this does not mean that the classifier is worse at high zenith distances. This needs to be investigated to rule out a bad model performance. With the test datasets and the IRFs created on the respective declination lines, this might improve regardless.

With three more LSTs to come, the direction reconstruction and the background suppression of an LST array will surpass the mono LST performance by a large margin. Most recently of all stereo IACT observatories, MAGIC showed us the performance boost of stereo observations [12], and the same improvement is expected once LST-2 is built and is observing.

The prototype implementation of an unfolding method based on the RUN algorithm, which I have implemented for `Gammapy`, was tested and proven to work on toy simulations. More work must be done to officially include this implementation in a released version of `Gammapy`. In the `Gammapy` code, regularization will be treated as a prior. However, priors are not yet available in `Gammapy`. I have started writing a *Proposal for Implementation in Gammapy (PIG)*, which is currently being

pursued⁸. After accepting this **PIG** for priors on model parameters, the unfolding implementation can be quickly accepted. My work gives a solid foundation for the implementation and further evaluation of Regularized Unfolding with the possibility to cross-check the final official implementation with the automatic analysis framework also presented in this thesis.

⁸<https://github.com/gammapy/gammapy/pull/4381>

Bibliography

- [1] A. Aab et al. “Large-scale Cosmic-Ray Anisotropies above 4 EeV Measured by the Pierre Auger Observatory”. In: *The Astrophysical Journal* 868.1 (Nov. 2018), p. 4. DOI: 10.3847/1538-4357/aae689 (cit. on p. 5).
- [2] M. G. Aartsen et al. “Measurement of the cosmic ray energy spectrum with IceTop-73”. In: *Physical Review D* 88, 042004 (Aug. 2013), p. 042004. DOI: 10.1103/PhysRevD.88.042004 (cit. on p. 6).
- [3] M. G. Aartsen et al. “The IceCube Neutrino Observatory: instrumentation and online systems”. In: *Journal of Instrumentation* 12.3 (Mar. 2017), P03012. DOI: 10.1088/1748-0221/12/03/P03012 (cit. on p. 11).
- [4] R. U. Abbasi et al. “First Observation of the Greisen-Zatsepin-Kuzmin Suppression”. In: *Physical Review Letters* 100, 101101 (Mar. 2008), p. 101101. DOI: 10.1103/PhysRevLett.100.101101 (cit. on p. 6).
- [5] B. P. Abbott et al. “Multi-messenger Observations of a Binary Neutron Star Merger”. In: *The Astrophysical Journal Letters* 848.2 (Oct. 2017), p. L12. DOI: 10.3847/2041-8213/aa91c9 (cit. on p. 12).
- [6] A. A. Abdo et al. “FERMI-LARGE AREA TELESCOPE OBSERVATIONS OF MARKARIAN 421: THE MISSING PIECE OF ITS SPECTRAL ENERGY DISTRIBUTION”. In: *The Astrophysical Journal* 736.2 (July 2011), p. 131. DOI: 10.1088/0004-637x/736/2/131 (cit. on pp. 8, 11, 83).
- [7] S. Abdollahi et al. “Fermi Large Area Telescope Fourth Source Catalog”. In: *The Astrophysical Journal Supplement Series* 247.1, 33 (Mar. 2020), p. 33. DOI: 10.3847/1538-4365/ab6bcb (cit. on p. 9).
- [8] F. Acernese et al. “Advanced Virgo: a second-generation interferometric gravitational wave detector”. In: *Classical and Quantum Gravity* 32.2 (Dec. 2014), p. 024001. DOI: 10.1088/0264-9381/32/2/024001 (cit. on p. 12).
- [9] A. Acharyya et al. “Monte Carlo studies for the optimisation of the Cherenkov Telescope Array layout”. In: *Astroparticle Physics* 111 (Sept. 2019), pp. 35–53. DOI: 10.1016/j.astropartphys.2019.04.001 (cit. on p. 29).

- [10] C. B. Adams et al. “Design and performance of the prototype Schwarzschild-Couder telescope camera”. In: *Journal of Astronomical Telescopes, Instruments, and Systems* 8.01 (Feb. 2022). DOI: 10.1117/1.jatis.8.1.014007 (cit. on p. 18).
- [11] J.-M. Alameddine et al. *Discovery in Physics*. Ed. by K. Morik and W. Rhode. De Gruyter, Nov. 2022. DOI: 10.1515/9783110785968 (cit. on p. 75).
- [12] J. Aleksić et al. “Performance of the MAGIC stereo system obtained with Crab Nebula data”. In: *Astroparticle Physics* 35.7 (2012), pp. 435–448. ISSN: 0927-6505. DOI: 10.1016/j.astropartphys.2011.11.007 (cit. on pp. 31, 86).
- [13] J. Aleksić et al. “The major upgrade of the MAGIC telescopes, Part II: A performance study using observations of the Crab Nebula”. In: *Astroparticle Physics* 72 (2016), pp. 76–94. ISSN: 0927-6505. DOI: 10.1016/j.astropartphys.2015.02.005 (cit. on p. 18).
- [14] P. Alken et al. “International Geomagnetic Reference Field: the thirteenth generation”. In: *Earth, Planets and Space* 73.1 (Feb. 2021). DOI: 10.1186/s40623-020-01288-x (cit. on p. 56).
- [15] M. Amenomori et al. “The All-Particle Spectrum of Primary Cosmic Rays in the Wide Energy Range from 10^{14} to 10^{17} eV Observed with the Tibet-III Air-Shower Array”. In: *Astrophysical Journal* 678 (May 2008), pp. 1165–1179. DOI: 10.1086/529514 (cit. on p. 6).
- [16] H. Anderhub et al. “Design and operation of FACT – the first G-APD Cherenkov telescope”. In: *Journal of Instrumentation* 8.06 (June 2013), P06008. DOI: 10.1088/1748-0221/8/06/P06008 (cit. on p. 18).
- [17] A. Arbet-Engels et al. “The relentless variability of Mrk 421 from the TeV to the radio”. In: *Astronomy & Astrophysics* 647 (Mar. 2021), A88. DOI: 10.1051/0004-6361/201935557 (cit. on p. 10).
- [18] Astropy Collaboration et al. “Astropy: A community Python package for astronomy”. In: *Astronomy & Astrophysics* 558, A33 (Oct. 2013), A33. DOI: 10.1051/0004-6361/201322068 (cit. on p. 51).
- [19] Astropy Collaboration et al. “The Astropy Project: Building an Open-science Project and Status of the v2.0 Core Package”. In: *The Astronomical Journal* 156.3, 123 (July 2018), p. 123. DOI: 10.3847/1538-3881/aabc4f (cit. on p. 51).
- [20] Astropy Collaboration et al. “The Astropy Project: Sustaining and Growing a Community-oriented Open-source Project and the Latest Major Release (v5.0) of the Core Package”. In: *The Astrophysical Journal* 935.2, 167 (Aug. 2022), p. 167. DOI: 10.3847/1538-4357/ac7c74 (cit. on p. 51).

-
- [21] W. B. Atwood et al. “The Large Area Telescope on the Fermi Gamma-Ray Space Telescope Mission”. In: *The Astrophysical Journal* 697.2 (June 2009), pp. 1071–1102. DOI: 10.1088/0004-637X/697/2/1071 (cit. on pp. 8, 17).
- [22] S. Bass et al. “Microscopic models for ultrarelativistic heavy ion collisions”. In: *Progress in Particle and Nuclear Physics* 41 (1998), pp. 255–369. ISSN: 0146-6410. DOI: 10.1016/S0146-6410(98)00058-1 (cit. on p. 27).
- [23] V. Beckmann and C. R. Shrader. *Active Galactic Nuclei*. en. Weinheim, Germany: Wiley-VCH Verlag, Aug. 2012 (cit. on p. 10).
- [24] A. R. Bell. “The acceleration of cosmic rays in shock fronts - I”. In: *Monthly Notices of the Royal Astronomical Society* 182.2 (Feb. 1978), pp. 147–156. DOI: 10.1093/mnras/182.2.147 (cit. on p. 6).
- [25] K. Bernlöhr et al. “Monte Carlo design studies for the Cherenkov Telescope Array”. In: *Astroparticle Physics* 43 (Mar. 2013), pp. 171–188. DOI: 10.1016/j.astropartphys.2012.10.002 (cit. on pp. 27, 29).
- [26] K. Bernlöhr. “Simulation of imaging atmospheric Cherenkov telescopes with CORSIKA and `sim_telarray`”. In: *Astroparticle Physics* 30.3 (2008), pp. 149–158. ISSN: 0927-6505. DOI: 10.1016/j.astropartphys.2008.07.009 (cit. on p. 26).
- [27] K. Bernlöhr. *The IACT/ATMO package for CORSIKA*. Feb. 10, 2023. URL: <https://www.mpi-hd.mpg.de/hfm/~bernlohr/iact-atmo/> (visited on 2023-07-29) (cit. on p. 26).
- [28] M. Bertaina et al. “KASCADE-Grande energy spectrum of cosmic rays interpreted with post-LHC hadronic interaction models”. In: *Proceedings of the 34th International Cosmic Ray Conference*. Vol. 34. ICRC 2015. July 2015, 359, p. 359. DOI: 10.22323/1.236.0359 (cit. on p. 6).
- [29] A. Biland et al. “Calibration and performance of the photon sensor response of FACT — the first G-APD Cherenkov telescope”. In: *Journal of Instrumentation* 9.10 (Oct. 2014), P10012. DOI: 10.1088/1748-0221/9/10/P10012 (cit. on p. 18).
- [30] V. Blobel. “Unfolding methods in high-energy physics experiments”. In: *Proceedings of the 1984 CERN School of Computing* (1985). DOI: 10.5170/CERN-1985-009.88 (cit. on p. 74).
- [31] M. Börner. “Bestimmung des Energiespektrums von atmosphärischen Myonenneutrinos mit 3 Jahren Daten des IceCube-Detektors”. de. PhD thesis. TU Dortmund University, 2018. DOI: 10.17877/DE290R-19089 (cit. on p. 75).

- [32] K. Brügge. “Unmasking the gamma-ray sky: comprehensive and reproducible analysis for Cherenkov telescopes”. en. PhD thesis. TU Dortmund University, 2019. DOI: 10.17877/DE290R-20440 (cit. on pp. 6, 20).
- [33] M. Bunse. “Machine learning for acquiring knowledge in astro-particle physics”. en. PhD thesis. TU Dortmund University, 2022. DOI: 10.17877/DE290R-23021 (cit. on p. 73).
- [34] M. Bunse et al. “Unification of Deconvolution Algorithms for Cherenkov Astronomy”. In: *2018 IEEE 5th International Conference on Data Science and Advanced Analytics (DSAA)*. IEEE, Oct. 2018. DOI: 10.1109/dsaa.2018.00012 (cit. on p. 73).
- [35] Cherenkov Telescope Array Consortium. *Science with the Cherenkov Telescope Array*. WORLD SCIENTIFIC, Feb. 2018. DOI: 10.1142/10986 (cit. on pp. 19, 21).
- [36] Cherenkov Telescope Array Observatory gGmbH. *CTAO Adopts the Gammapy Software Package for Science Analysis*. June 10, 2021. URL: <https://www.cta-observatory.org/ctao-adopts-the-gammapy-software-package-for-science-analysis> (visited on 2023-05-17) (cit. on p. 49).
- [37] Cherenkov Telescope Array Observatory gGmbH. *CTAO Releases the Layout of its Arrays for the Alpha Configuration*. July 15, 2022. URL: <https://www.cta-observatory.org/ctao-releases-layouts-for-alpha-configuration> (cit. on pp. 19, 20).
- [38] Cherenkov Telescope Array Observatory gGmbH. *Large-Sized Telescope*. 2023. URL: <https://www.cta-observatory.org/project/technology/lst/> (cit. on p. 19).
- [39] *CORSIKA 8 – Contributions to the 37th International Cosmic Ray Conference in Berlin Germany (ICRC 2021)*. 2021. DOI: 10.48550/arXiv.2112.11761 (cit. on p. 27).
- [40] J. Cortina. “Status of the Large Size Telescopes of the Cherenkov Telescope Array”. In: *Proceedings of 36th International Cosmic Ray Conference — PoS(ICRC2019)*. Vol. 358. 2019, p. 653. DOI: 10.22323/1.358.0653 (cit. on pp. 19–21, 28).
- [41] CTA-LST Project et al. “Observations of the Crab Nebula and Pulsar with the Large-Sized Telescope Prototype of the Cherenkov Telescope Array”. In: *arXiv* (2023). DOI: 10.48550/ARXIV.2306.12960 (cit. on pp. 21, 86).
- [42] H. D. Curtis. “Descriptions of 762 Nebulae and Clusters Photographed with the Crossley Reflector”. In: *Publications of Lick Observatory* 13 (Jan. 1918), pp. 9–42. URL: <https://ui.adsabs.harvard.edu/abs/1918PLicO..13...9C> (cit. on p. 8).

-
- [43] C. Deil et al. “Gammapy - A prototype for the CTA science tools”. In: *35th International Cosmic Ray Conference (ICRC2017)*. Vol. 301. International Cosmic Ray Conference. June 2017, 766, p. 766. DOI: 10.22323/1.301.0766 (cit. on pp. 49, 51).
- [44] C. Deil et al. *Data formats for gamma-ray astronomy - version 0.3*. Nov. 2022. DOI: 10.5281/zenodo.7304668 (cit. on p. 65).
- [45] H. Dembinski et al. *scikit-hep/iminuit*. June 2023. DOI: 10.5281/zenodo.8191656 (cit. on p. 51).
- [46] R. M. Dominik et al. “Interpolation of Instrument Response Functions for the Cherenkov Telescope Array in the Context of pyirf”. In: *Proceedings of 38th International Cosmic Ray Conference — PoS(ICRC2023)*. Vol. 444. 2023, p. 618. DOI: 10.22323/1.444.0618 (cit. on p. 86).
- [47] E. Dwek and F. Krennrich. “The extragalactic background light and the gamma-ray opacity of the universe”. In: *Astroparticle Physics* 43 (2013), pp. 112–133. ISSN: 0927-6505. DOI: 10.1016/j.astropartphys.2012.09.003 (cit. on p. 8).
- [48] S. Einecke. “The data mining guide to the galaxy”. en. PhD thesis. TU Dortmund University, 2017. DOI: 10.17877/DE290R-18295 (cit. on p. 10).
- [49] R. Engel et al. “Towards A Next Generation of CORSIKA: A Framework for the Simulation of Particle Cascades in Astroparticle Physics”. In: *Computing and Software for Big Science* 3.1 (Dec. 2018). DOI: 10.1007/s41781-018-0013-0 (cit. on p. 27).
- [50] F. Fenu and Pierre Auger Collaboration. “The cosmic ray energy spectrum measured using the Pierre Auger Observatory”. In: *Proceedings of the 35th International Cosmic Ray Conference*. Vol. 301. ICRC 2017. 2017, 486, p. 486 (cit. on p. 6).
- [51] A. Ferrari et al. “FLUKA: A Multi-Particle Transport Code”. In: *SLAC* (Dec. 2005). DOI: 10.2172/877507 (cit. on p. 27).
- [52] E. Garcia, T. Vuillaume, and L. Nickel. *The lstMCpipe library*. 2022. arXiv: 2212.00120 [astro-ph.IM] (cit. on p. 55).
- [53] H. E. S. S. Collaboration. *Largest ever Cherenkov telescope sees first light*. 2012. URL: https://www.mpi-hd.mpg.de/hfm/HESS/pages/press/2012/HESS_II_first_light (cit. on p. 18).
- [54] H. E. S. S. Collaboration et al. “The H. E. S. S. Galactic plane survey”. In: *Astronomy & Astrophysics* 612, A1 (Apr. 2018), A1. DOI: 10.1051/0004-6361/201732098 (cit. on p. 49).

- [55] C. R. Harris et al. “Array programming with NumPy”. In: *Nature* 585.7825 (Sept. 2020), pp. 357–362. DOI: 10.1038/s41586-020-2649-2 (cit. on p. 51).
- [56] D. Heck et al. *CORSIKA: a Monte Carlo code to simulate extensive air showers*. 1998. URL: <https://ui.adsabs.harvard.edu/abs/1998cmcc.book.....H> (cit. on pp. 25, 26).
- [57] HEGRA Collaboration et al. “Performance of the stereoscopic system of the HEGRA imaging air Čerenkov telescopes: Monte Carlo simulations and observations”. In: *Astroparticle Physics* 10.4 (May 1999), pp. 275–289. DOI: 10.1016/S0927-6505(98)00062-0 (cit. on p. 17).
- [58] W. Heitler. *The quantum theory of radiation*. 2nd ed. Oxford University Press, 1944. URL: <https://archive.org/details/in.ernet.dli.2015.37198> (cit. on pp. 12, 13).
- [59] V. F. Hess. “Über Beobachtungen der durchdringenden Strahlung bei sieben Freiballonfahrten”. In: *Phys. Z.* 13 (1912), pp. 1084–1091. URL: <https://inspirehep.net/literature/1623161> (cit. on pp. 1, 5).
- [60] A. M. Hillas. “Čerenkov Light Images of EAS Produced by Primary Gamma Rays and by Nuclei”. In: *19th International Cosmic Ray Conference (ICRC19), Volume 3*. Vol. 3. International Cosmic Ray Conference. Aug. 1985, p. 445. URL: <https://ui.adsabs.harvard.edu/abs/1985ICRC...3..445H> (cit. on p. 31).
- [61] J. D. Hunter. “Matplotlib: A 2D graphics environment”. In: *Computing in Science & Engineering* 9.3 (2007), pp. 90–95. DOI: 10.1109/MCSE.2007.55 (cit. on p. 51).
- [62] IceCube Collaboration et al. “Multimessenger observations of a flaring blazar coincident with high-energy neutrino IceCube-170922A”. In: *Science* 361.6398 (2018), eaat1378. DOI: 10.1126/science.aat1378 (cit. on p. 9).
- [63] M. Jacquemont et al. “GammaLearn: A Deep Learning Framework for IACT Data”. In: *Proceedings of 36th International Cosmic Ray Conference — PoS(ICRC2019)*. Vol. 358. 2019, p. 705. DOI: 10.22323/1.358.0705 (cit. on p. 31).
- [64] F. James and M. Roos. “Minuit: A System for Function Minimization and Analysis of the Parameter Errors and Correlations”. In: *Comput. Phys. Commun.* 10 (1975), pp. 343–367. DOI: 10.1016/0010-4655(75)90039-9 (cit. on p. 51).
- [65] J. V. Jelley. “Čerenkov radiation and its applications”. In: *British Journal of Applied Physics* 6.7 (July 1955), p. 227. DOI: 10.1088/0508-3443/6/7/301 (cit. on p. 14).

-
- [66] J.-H. Koehne et al. “PROPOSAL: A tool for propagation of charged leptons”. In: *Computer Physics Communications* 184.9 (2013), pp. 2070–2090. ISSN: 0010-4655. DOI: 10.1016/j.cpc.2013.04.001 (cit. on p. 27).
- [67] K. Kosack et al. *cta-observatory/ctapipe*. Version v0.12.0. Nov. 2021. DOI: 10.5281/zenodo.5720333 (cit. on p. 51).
- [68] K. Kosack et al. *cta-observatory/ctapipe*. Version v0.19.3. June 2023. DOI: 10.5281/zenodo.8063139 (cit. on p. 29).
- [69] T.-P. Li and Y.-Q. Ma. “Analysis methods for results in gamma-ray astronomy.” In: *The Astrophysical Journal* 272 (Sept. 1983), pp. 317–324. DOI: 10.1086/161295 (cit. on p. 46).
- [70] LIGO Scientific Collaboration et al. “Advanced LIGO”. In: *Classical and Quantum Gravity* 32.7 (Mar. 2015), p. 074001. DOI: 10.1088/0264-9381/32/7/074001 (cit. on p. 12).
- [71] M. Linhoff et al. *cta-observatory/pyirf*. Version v0.8.1. Mar. 2023. DOI: 10.5281/zenodo.7741289 (cit. on pp. 61, 86).
- [72] M. Linhoff et al. “ctapipe - Prototype Open Event Reconstruction Pipeline for the Cherenkov Telescope Array”. In: *Proceedings of 38th International Cosmic Ray Conference — PoS(ICRC2023)*. July 2023. DOI: 10.22323/1.444.0703. URL: <https://doi.org/10.22323/1.444.0703> (cit. on p. 29).
- [73] R. Lopez-Coto et al. *cta-observatory/cta-1stchain*. Version v0.9.13. Jan. 2023. DOI: 10.5281/zenodo.7565826 (cit. on p. 51).
- [74] MAGIC Collaboration et al. “Investigation of the correlation patterns and the Compton dominance variability of Mrk 421 in 2017”. In: *Astronomy & Astrophysics* 655 (Nov. 2021), A89. DOI: 10.1051/0004-6361/202141004 (cit. on p. 10).
- [75] M. Meyer, D. Horns, and H.-S. Zechlin. “The Crab Nebula as a standard candle in very high-energy astrophysics”. In: *Astronomy & Astrophysics* 523, A2 (Nov. 2010), A2. DOI: 10.1051/0004-6361/201014108 (cit. on p. 79).
- [76] F. Mölder et al. “Sustainable data analysis with Snakemake [version 2; peer review: 2 approved]”. In: *F1000Research* 10.33 (2021). DOI: 10.12688/f1000research.29032.2 (cit. on pp. 51, 85).
- [77] M. Nagano and A. A. Watson. “Observations and implications of the ultrahigh-energy cosmic rays”. In: *Reviews of Modern Physics* 72 (3 June 2000), pp. 689–732. DOI: 10.1103/RevModPhys.72.689 (cit. on p. 17).

- [78] NASA, ESA, NRAO/AUI/NSF and G. Dubner (University of Buenos Aires). *Observatories Combine to Crack Open the Crab Nebula*. May 10, 2017. URL: <https://www.nasa.gov/feature/goddard/2017/observatories-combine-to-crack-open-the-crab-nebula> (visited on 2023-07-26) (cit. on p. 7).
- [79] W. R. Nelson, H. Hirayama, and D. W. Rogers. *EGS4 code system*. Dec. 1985. URL: <https://www.osti.gov/biblio/6137659> (cit. on p. 27).
- [80] D. Nieto Castaño et al. “CTLearn: Deep Learning for Gamma-ray Astronomy”. In: *Proceedings of 36th International Cosmic Ray Conference — PoS(ICRC2019)*. Vol. 358. 2019, p. 752. DOI: 10.22323/1.358.0752 (cit. on p. 31).
- [81] M. Nöthe. “Monitoring the high energy universe”. en. PhD thesis. TU Dortmund University, 2020. DOI: 10.17877/DE290R-21143 (cit. on p. 27).
- [82] M. Nöthe et al. *cta-observatory/pyirf*. Version v0.6.0. Jan. 2022. DOI: 10.5281/zenodo.5833284 (cit. on pp. 51, 61).
- [83] D. W. Pankenier. “Notes on translations of the East Asian records relating to the supernova of AD 1054”. In: *Journal of Astronomical History and Heritage* 9 (June 2006), pp. 77–82 (cit. on p. 2).
- [84] Particle Data Group et al. “Review of Particle Physics”. In: *Progress of Theoretical and Experimental Physics* 2022.8 (Aug. 2022), p. 083C01. ISSN: 2050-3911. DOI: 10.1093/ptep/ptac097 (cit. on p. 12).
- [85] F. Pedregosa et al. “Scikit-learn: Machine Learning in Python”. In: *Journal of Machine Learning Research* 12 (2011), pp. 2825–2830 (cit. on p. 37).
- [86] J. S. Perkins, G. Maier, and The VERITAS Collaboration. *VERITAS Telescope 1 Relocation: Details and Improvements*. 2009. DOI: 10.48550/ARXIV.0912.3841 (cit. on p. 18).
- [87] D. Pohl et al. “15 Years Later: A Historic Look Back at ”Quake 3: Ray Traced””. In: *Proceedings of the 2020 Federated Conference on Computer Science and Information Systems*. IEEE, July 2020. DOI: 10.15439/2020f3 (cit. on p. 27).
- [88] M. Punch et al. “Detection of TeV photons from the active galaxy Markarian 421”. In: *Nature* 358.6386 (Aug. 1992), pp. 477–478. DOI: 10.1038/358477a0 (cit. on p. 10).
- [89] M. Reininghaus and R. Ulrich. “CORSIKA 8 – Towards a modern framework for the simulation of extensive air showers”. In: *EPJ Web of Conferences* 210 (Oct. 2019), p. 02011. DOI: 10.1051/epjconf/201921002011 (cit. on p. 27).

-
- [90] A. Rohatgi. *Webplotdigitizer: Version 4.6*. 2022. URL: <https://automeris.io/WebPlotDigitizer> (cit. on p. 11).
- [91] T. Ruhe et al. “D-SEA: A Data Mining Approach to Unfolding”. In: *33rd International Cosmic Ray Conference*. 2013, p. 0212 (cit. on p. 73).
- [92] A. Sandrock, J.-M. Alameddine, and F. Riehn. “Validation of Electromagnetic Showers in CORSIKA 8”. In: *arXiv e-prints* (Aug. 2023). DOI: 10.48550/arXiv.2308.07112 (cit. on p. 27).
- [93] Schmidt, Fabian, University of Leeds, UK. *Proton shower*. https://www-zeuthen.desy.de/~jknapp/fs/proton_11_0deg.xz.png. Possibly created earlier, date from earliest Wayback Machine snapshot I could find: <https://web.archive.org/web/20140421034252/https://www-zeuthen.desy.de/~jknapp/fs/proton-showers.html>. 2014 (cit. on p. 28).
- [94] SIMBAD astronomical database. *Mrk 421 – BL Lac*. 2020. URL: <https://simbad.u-strasbg.fr/simbad/sim-id?Ident=Mrk+421> (cit. on p. 10).
- [95] L. A. Tejedor et al. “A Trigger Interface Board for the Large and Medium Sized telescopes of the Cherenkov Telescope Array”. In: *Nuclear Instruments and Methods in Physics Research Section A: Accelerators, Spectrometers, Detectors and Associated Equipment* 1027 (2022), p. 166058. ISSN: 0168-9002. DOI: 10.1016/j.nima.2021.166058 (cit. on pp. 22, 30).
- [96] J. Thorne et al. *AGN Unification Diagram*. Was originally created to be included in the introduction of Thorne, 2022. Mar. 2022. DOI: 10.5281/zenodo.6381013 (cit. on p. 10).
- [97] J. Thorne et al. “Deep Extragalactic Visible Legacy Survey (DEVILS): identification of AGN through SED fitting and the evolution of the bolometric AGN luminosity function”. In: *Monthly Notices of the Royal Astronomical Society* 509.4 (Feb. 2022), pp. 4940–4961. DOI: 10.1093/mnras/stab3208 (cit. on p. 10).
- [98] A. N. Tikhonov. “On the stability of inverse problems”. In: *Proceedings of the USSR Academy of Sciences* 39 (1943), pp. 195–198 (cit. on p. 75).
- [99] T. Vincenty. “DIRECT AND INVERSE SOLUTIONS OF GEODESICS ON THE ELLIPSOID WITH APPLICATION OF NESTED EQUATIONS”. In: *Survey Review* 23.176 (Apr. 1975), pp. 88–93. DOI: 10.1179/sre.1975.23.176.88 (cit. on p. 56).
- [100] P. Virtanen et al. “SciPy 1.0: Fundamental Algorithms for Scientific Computing in Python”. In: *Nature Methods* 17 (2020), pp. 261–272. DOI: 10.1038/s41592-019-0686-2 (cit. on p. 51).

Bibliography

- [101] T. C. Weekes et al. “Observation of TeV Gamma Rays from the Crab Nebula Using the Atmospheric Cerenkov Imaging Technique”. In: *The Astrophysical Journal* 342 (July 1989), p. 379. DOI: 10.1086/167599 (cit. on pp. 2, 17).
- [102] M. Wenger et al. “The SIMBAD astronomical database. The CDS reference database for astronomical objects”. In: *Astronomy & Astrophysics Supplement* 143 (Apr. 2000), pp. 9–22. DOI: 10.1051/aas:2000332 (cit. on p. 10).

Appendix

1 Run List

1	Night: Runs
	20201212: 3216 3217 3218 3219 3220 3221 3222 3223 3224 3225 3226 3227
	20201213: 3238 3239
	20201214: 3247 3248 3249 3250
5	20210214: 3661 3662 3663 3664 3665 3666 3667 3668
	20210215: 3687 3688
	20210216: 3715 3716 3717 3718 3720 3721
	20210217: 3732 3733 3734 3735 3736 3737
	20210313: 4016 4017 4018 4019
10	20210316: 4097 4098 4099 4100
	20210317: 4131 4132 4133 4134 4135 4136 4137 4138
	20210318: 4153 4154 4155 4156
	20210320: 4184 4185 4186 4187 4188
	20210321: 4208
15	20210416: 4441 4442 4443
	20210417: 4457 4458 4459
	20210418: 4479
	20210430: 4568 4569 4570 4571 4572
	20210505: 4612 4613 4614
20	20210508: 4649
	20210509: 4667 4668 4669 4670 4671
	20210531: 4852 4853
	20210601: 4868 4869
	20210606: 4939
25	20220205: 6900 6901 6902 6903
	20220206: 6939 6940 6941 6947 6948 6949 6950 6951 6952
	20220208: 6993 6994 6997 6998 6999
	20220209: 7026
	20220301: 7182 7183 7184
30	20220305: 7289 7290
	20220309: 7369 7370
	20220405: 7648 7649 7650
	20220406: 7684 7685 7687 7688 7689 7690 7692
	20220407: 7709 7710
35	20220421: 7849 7850 7851 7852
	20220428: 7962 7963 7964 7965
	20220429: 7995
	20220504: 8117 8118 8119 8124 8125 8126 8127 8128 8129
	20220505: 8180 8183
40	20220506: 8215 8216 8217
	20220518: 8350 8351 8352 8353 8354
	20220519: 8359 8360
	20220521: 8386 8387
	20220523: 8422 8423

2 Configuration Files

2.1 Lstchain Create IRF

```
1 {
  "DL3Cuts": {
    "max_gh_cut": 0.95,
    "min_gh_cut": 0.1,
    5 "gh_efficiency": 0.9,
    "max_theta_cut": 0.4,
    "min_theta_cut": 0.05,
    "theta_containment": 0.68
  },
  10 "IRFFITSWriter": {
    "energy_dependent_theta": true,
    "energy_dependent_gh": true,
    "point_like": true,
    "overwrite": true
  15 }
}
```

2.2 Lstchain DL1 to DL2

```
1 {
  "source_config": {
    "EventSource": {
    5 "allowed_tels": [1],
    "max_events": null
    },
    "LSTEventSource": {
    10 "default_trigger_type": "ucts",
    "allowed_tels": [1],
    "min_flatfield_adc": 3000,
    "min_flatfield_pixel_fraction": 0.8,
    "calibrate_flatfields_and_pedestals": false,
    "EventTimeCalculator": {
    15 "dragon_reference_counter": null,
    "dragon_reference_time": null
    },
    "PointingSource": {
    "drive_report_path": null
    },
    20 "LSTROCorrections": {
    "calib_scale_high_gain": 1.088,
    "calib_scale_low_gain": 1.004,
    "drs4_pedestal_path": null,
    "calibration_path": null,
  }
}
```

```
25     "drs4_time_calibration_path": null
    }
  },
  "events_filters": {
30     "intensity": [0, Infinity],
    "width": [0, Infinity],
    "length": [0, Infinity],
    "wl": [0, Infinity],
    "r": [0, Infinity],
35     "leakage_intensity_width_2": [0, Infinity]
  },
  "n_training_events": {
    "gamma_regressors": 1.0,
    "gamma_tmp_regressors": 0.8,
40     "gamma_classifier": 0.2,
    "proton_classifier": 1.0
  },
  "tailcut": {
45     "picture_thresh": 8,
    "boundary_thresh": 4,
    "keep_isolated_pixels": false,
    "min_number_picture_neighbors": 2,
    "use_only_main_island": false,
    "delta_time": 2
50  },
  "tailcuts_clean_with_pedestal_threshold": {
    "picture_thresh": 8,
    "boundary_thresh": 4,
55     "sigma": 2.5,
    "keep_isolated_pixels": false,
    "min_number_picture_neighbors": 2,
    "use_only_main_island": false,
    "delta_time": 2
60  },
  "dynamic_cleaning": {
    "apply": true,
    "threshold": 267,
    "fraction_cleaning_intensity": 0.03
65  },
  "random_forest_energy_regressor_args": {
    "max_depth": 30,
    "min_samples_leaf": 10,
    "n_jobs": -1,
    "n_estimators": 150,
70     "bootstrap": true,
    "criterion": "squared_error",
    "max_features": "auto",
    "max_leaf_nodes": null,
    "min_impurity_decrease": 0.0,
```

```
75     "min_samples_split": 10,
      "min_weight_fraction_leaf": 0.0,
      "oob_score": false,
      "random_state": 42,
      "verbose": 0,
80     "warm_start": false
  },
  "random_forest_disp_regressor_args": {
    "max_depth": 30,
    "min_samples_leaf": 10,
85    "n_jobs": -1,
    "n_estimators": 150,
    "bootstrap": true,
    "criterion": "squared_error",
    "max_features": "auto",
90    "max_leaf_nodes": null,
    "min_impurity_decrease": 0.0,
    "min_samples_split": 10,
    "min_weight_fraction_leaf": 0.0,
    "oob_score": false,
95    "random_state": 42,
    "verbose": 0,
    "warm_start": false
  },
  "random_forest_disp_classifier_args": {
100    "max_depth": 30,
    "min_samples_leaf": 10,
    "n_jobs": -1,
    "n_estimators": 100,
    "criterion": "gini",
105    "min_samples_split": 10,
    "min_weight_fraction_leaf": 0.0,
    "max_features": "auto",
    "max_leaf_nodes": null,
    "min_impurity_decrease": 0.0,
110    "bootstrap": true,
    "oob_score": false,
    "random_state": 42,
    "verbose": 0.0,
    "warm_start": false,
115    "class_weight": null
  },
  "random_forest_particle_classifier_args": {
    "max_depth": 30,
    "min_samples_leaf": 10,
120    "n_jobs": -1,
    "n_estimators": 100,
    "criterion": "gini",
    "min_samples_split": 10,
    "min_weight_fraction_leaf": 0.0,
```

```
125     "max_features": "auto",
      "max_leaf_nodes": null,
      "min_impurity_decrease": 0.0,
      "bootstrap": true,
      "oob_score": false,
130     "random_state": 42,
      "verbose": 0.0,
      "warm_start": false,
      "class_weight": null
    },
135     "energy_regression_features": [
      "log_intensity",
      "width",
      "length",
      "x",
140     "y",
      "wl",
      "skewness",
      "kurtosis",
      "time_gradient",
145     "leakage_intensity_width_2",
      "az_tel",
      "alt_tel"
    ],
    "disp_method": "disp_norm_sign",
150     "disp_regression_features": [
      "log_intensity",
      "width",
      "length",
      "wl",
155     "skewness",
      "kurtosis",
      "time_gradient",
      "leakage_intensity_width_2",
      "az_tel",
160     "alt_tel"
    ],
    "disp_classification_features": [
      "log_intensity",
      "width",
165     "length",
      "wl",
      "skewness",
      "kurtosis",
      "time_gradient",
170     "leakage_intensity_width_2",
      "az_tel",
      "alt_tel"
    ],
    "particle_classification_features": [
```

```
175     "log_intensity",
        "width",
        "length",
        "x",
        "y",
180     "wl",
        "signed_skewness",
        "kurtosis",
        "signed_time_gradient",
        "leakage_intensity_width_2",
185     "log_reco_energy",
        "reco_disp_norm",
        "reco_disp_sign",
        "az_tel",
        "alt_tel"
190 ],
    "allowed_tels": [1],
    "write_pe_image": false,
    "mc_image_scaling_factor": 1,
    "image_extractor": "LocalPeakWindowSum",
195     "image_extractor_for_muons": "GlobalPeakWindowSum",
    "CameraCalibrator": {
        "apply_waveform_time_shift": false
    },
    "time_sampling_correction_path": "default",
200     "LocalPeakWindowSum": {
        "window_shift": 4,
        "window_width": 8,
        "apply_integration_correction": true
    },
205     "GlobalPeakWindowSum": {
        "window_shift": 4,
        "window_width": 8,
        "apply_integration_correction": true
    },
210     "timestamps_pointing": "ucts",
    "train_gamma_src_r_deg": [0, Infinity],
    "source_dependent": false,
    "mc_nominal_source_x_deg": 0.4,
    "mc_nominal_source_y_deg": 0.0,
215     "volume_reducer": {
        "algorithm": null,
        "parameters": {}
    },
    },
    "calibration_product": "LSTCalibrationCalculator",
220     "LSTCalibrationCalculator": {
        "systematic_correction_path": null,
        "squared_excess_noise_factor": 1.222,
        "flatfield_product": "FlasherFlatFieldCalculator",
        "pedestal_product": "PedestalIntegrator",
```



```

225   "PedestalIntegrator": {
      "sample_size": 10000,
      "sample_duration": 100000,
      "tel_id": 1,
      "time_sampling_correction_path": null,
230   "charge_median_cut_outliers": [-10, 10],
      "charge_std_cut_outliers": [-10, 10],
      "charge_product": "FixedWindowSum",
      "FixedWindowSum": {
        "window_shift": 6,
235   "window_width": 12,
        "peak_index": 18,
        "apply_integration_correction": false
      }
    },
240   "FlasherFlatFieldCalculator": {
      "sample_size": 10000,
      "sample_duration": 100000,
      "tel_id": 1,
      "time_sampling_correction_path": null,
245   "charge_product": "LocalPeakWindowSum",
      "charge_median_cut_outliers": [-0.5, 0.5],
      "charge_std_cut_outliers": [-10, 10],
      "time_cut_outliers": [2, 38],
      "LocalPeakWindowSum": {
250   "window_shift": 5,
        "window_width": 12,
        "apply_integration_correction": false
      }
    }
255 },
    "waveform_nsb_tuning": {
      "nsb_tuning": false,
      "nsb_tuning_ratio": 0.52,
      "spe_location": "lstchain/data/SinglePhE_ResponseInPhE_expo2Gaus.dat"
260 }
  }
}

```

3 Unfolding

The Probability Density Function (PDF)

$$f(x) = x \exp(-0.2x) \quad (.1)$$

and the response matrix

$$\mathbf{A} = \begin{pmatrix} 1 - \epsilon & \epsilon & 0 & \dots \\ \epsilon & 1 - 2\epsilon & \epsilon & 0 & \dots \\ 0 & \epsilon & 1 - 2\epsilon & \epsilon & \dots \\ \vdots & \vdots & \vdots & \ddots & \ddots \end{pmatrix}, \quad (.2)$$

with $\epsilon = 0.22$ are used.

From the PDF, divided into 20 bins x , g is generated randomly by rejection sampling. Those g are taken as measured events. They are transformed by the inverse of \mathbf{A} :

$$\hat{f} = \mathbf{A}^{-1}g, \quad (.3)$$

giving the unregularized and oscillating result.

To understand the influence of the eigenvalues to the unfolding, \mathbf{A} is transformed to its eigenbasis.

$$\mathbf{A} = \mathbf{U}\mathbf{D}\mathbf{U}^{-1}, \quad (.4)$$

where \mathbf{U} is the transformation matrix with the eigenvectors of \mathbf{A} and \mathbf{D} is diagonal with the eigenvalues λ of \mathbf{A} on the diagonal. The folding equation becomes

$$g = \mathbf{A}f = \mathbf{U}\mathbf{D}\mathbf{U}^{-1}f \quad (.5)$$

$$\mathbf{U}^{-1}g = \mathbf{D}\mathbf{U}^{-1}f. \quad (.6)$$

Using

$$c := \mathbf{U}^{-1}g \quad \text{and} \quad b := \mathbf{U}^{-1}f, \quad (.7)$$

therefore

$$f = \mathbf{U}b \quad \text{and} \quad g = \mathbf{U}c, \quad (.8)$$

the folding equation becomes

$$c = \mathbf{D}b \quad (.9)$$

and since \mathbf{D} is diagonal, the entries of c and b are transformed independently. In the unfolding

$$b_i = \frac{c_i}{\lambda_i} \quad (.10)$$

small eigenvalues amplify statistical fluctuations, and the solution oscillates.

Setting the smallest ten eigenvalues to zero, and use that resulting matrix to unfold, the oscillations are reduced in exchange for higher bin-to-bin correlations.

4 Crab Nebula Crosscheck

For the crosscheck of the implementation, the spectrum of the Crab Nebula is unfolded in figure 6.5. In figure 1 the optimal regularization strength is found using the minimal mean global correlation. Figure 2 shows the correlation of the unfolded

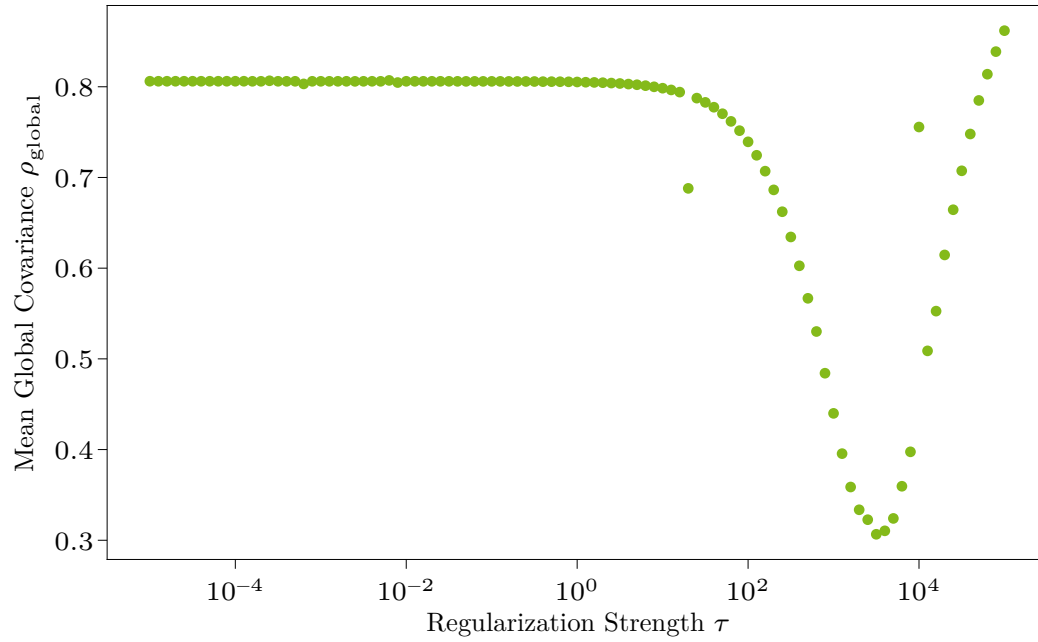


Figure 1: The optimal regularization strength τ is found as the point with minimal mean global correlation ρ_{global} (6.13).

flux points.

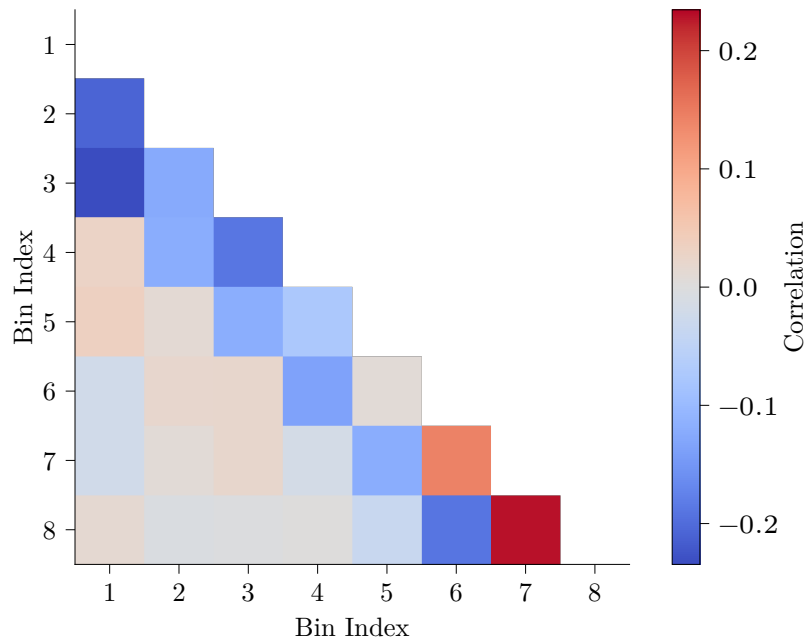


Figure 2: Correlation matrix of the unfolded flux points of the Crab Nebula spectrum. The underflow and overflow bins are not displayed. The self-correlation of each bin is also not displayed, to have a larger visual range in the color bar.

Glossary

AGN Active Galactic Nucleus. 2, 6–11, 21, 48, 51, 85

AUC Area Under Curve. 37, 38

CNN Convolutional Neural Network. 31

CORSIKA Cosmic Ray Simulations for Kascade. 25–29, 32, 33

CTA Cherenkov Telescope Array. v, 2, 17–20, 27, 29, 49, 60, 62, 65, 85

DAQ Data Acquisition. 22, 30

DL1a Data Level 1a. 30–33

DL1b Data Level 1b. 34

DL2 Data Level 2. 37, 63–65

DL3 Data Level 3. 43, 47, 65

DL4 Data Level 4. 68, 76

D-SEA Dortmund Spectrum Estimation Algorithm. 73

EAS Extensive Air Shower. 1, 2, 12–15, 17, 25, 27, 29, 30, 59

EBL Extragalactic Background Light. 8, 9, 19

FACT First G-APD Cherenkov Telescope. 10, 18, 19

Fermi-LAT Fermi Large Area Telescope. 8, 17

FoV Field of View. 20, 46, 59, 60, 66

GTC Gran Telescopio Canarias. 19

HAWC High-Altitude Water Cherenkov Gamma-Ray Observatory. 13

HEGRA High-Energy-Gamma-Ray Astronomy. 17, 18

- H. E. S. S.** High Energy Stereoscopic System. 18, 49
- IACR** Imaging Atmospheric Cherenkov Telescope. 2, 13, 15, 17, 18, 22, 25, 27, 41, 86
- IBU** Iterative Bayesian Unfolding. 73
- ICRS** International Celestial Reference System. 9
- IRF** Instrument Response Function. 2, 43–46, 55–59, 62, 65, 68, 76, 80, 86
- KASCADE** KARlsruhe Shower Core and Array DETector. 26
- KIT** Karlsruhe Institute of Technology. 27
- LC** Light Curve. 3, 48, 49
- LIGO** Laser Interferometer Gravitational-Wave Observatory. 12
- LST** Large-Sized Telescope. 2, 17, 19, 20, 55, 60, 62, 85, 86
- LST OSA** LST On-Site Analysis. 58
- MAGIC** Major Atmospheric Gamma Imaging Cherenkov. 10, 18, 19, 31, 49, 79, 86
- MC** Monte Carlo. 2, 25, 55, 57–59, 71, 79, 80, 86
- ML** Machine Learning. 2, 25, 29, 31, 37
- MSE** Mean Squared Error. 36, 38, 40
- MST** Medium-Sized Telescope. 19
- NSB** Night Sky Background. 21, 22, 52
- ORM** Observatorio del Roque de los Muchachos. 2, 18–20
- PA** Pierre Auger Observatory. 13
- PCA** Principal Component Analysis. 31, 34, 41, 43
- PDF** Probability Density Function. 105, 106
- PIG** Proposal for Implementation in **Gammapy**. 86, 87
- PMT** Photomultiplier Tube. 13, 17–19, 22, 25, 26, 28–30

PROPOSAL Propagator with optimal precision and optimized speed for all leptons. 27

PSF Point Spread Function. 45, 59, 65, 68

R0 Raw Data 0. 29

R1 Raw Data 1. 30

RF Random Forest. 25, 37, 39

ROC Receiver Operator Characteristic. 37, 38

RUN Regularized Unfolding. 74–76, 86

SCT Schwarzschild-Couder Telescope. 18

SED Spectral Energy Distribution. 3, 23, 48, 49

SiPM Silicon Photomultiplier. 18, 19, 22

SMBH Supermassive Black Hole. 5, 8

SSC Synchrotron Self-Compton. 6, 8, 11, 83

SST Small-Sized Telescope. 19

VERITAS Very Energetic Radiation Imaging Telescope Array System. 18, 49

VHE very-high-energy. 1, 2, 6–10, 13, 17, 20, 79, 85

VIRGO Virgo Interferometer. 12

VLT Very Large Telescope. 19

Acknowledgements

Danke Prof. Dr. Dr. Wolfgang Rhode, ohne dich wäre das alles hier nicht möglich gewesen. Danke für dein Vertrauen, deine Unterstützung, dein Wissen.

Danke Prof. Dr. Johannes Albrecht für die Begutachtung dieser Arbeit.

Danke Dr. habil Dominik Elsässer für die zahllosen Gespräche, die mich unendlich motivierten und begeisterten.

Danke Andrea Teichmann, dass du immer ein offenes Ohr hast.

Danke an die DFG, das BMBF, den SFB 876 und den SFB 1491 für die finanzielle Unterstützung.

Danke Dr. Maximilian Linhoff, dafür, dass du mich schon zur Bachelorarbeit an den Lehrstuhl geholt hast, für die vielen Diskussionen, und für alles, was ich von dir lernen konnte. Danke dir und Dr. Kai Brügge, dass die \TeX -Dateien eurer Dissertationen öffentlich sind.

Danke Lukas Nickel, für drei Jahre Tischnachbar. Danke dafür, dass du mein Code Sparringpartner warst, mit mir über Emacs, Lisp, Rust, TikZ, Vim, und wichtige Dinge diskutiert hast, dass du ein Freund geworden bist.

Danke Alicia Fattorini, die finale Zeit des Schreibens hätte ich ohne dich nicht geschafft.

Danke Ali, Elias, Lukas, Max, Michel, Simone, fürs Korrekturlesen.

Danke Felix, Kevin, Rune, für das tägliche Frühstück.

Danke an alle weiteren Kolleg:innen und Mitstreitenden der Arbeitsgruppe Astroteilchenphysik: Dominik, Jan Lukas, Jean-Marco, Johannes, Jonas, Karolin, Leonora, Lucas, Mirco, Pascal, Stefan, Tim, Tristan, es war mir eine große Freude euch kennenzulernen, und eine Ehre mit euch zusammenzuarbeiten.

Danke Lydia, dass du mir die Energie gibst, die ich brauche.

I love deadlines. I love the whooshing noise they make as they go by.
—Douglas Adams